

Investigating CMS Binary Chip Data Losses in the Phase II High
Luminosity Upgrade to the CMS

Mary-Ellen Phillips

2019 NSF/REU Program

Physics Department, University of Notre Dame

Advisors:

Kevin Lannon, Michael Hildreth

Abstract

The Large Hadron Collider (LHC) is set to reach a stage of high luminosity by 2026. In order to keep up with the resulting increase in pileup conditions, the Compact Muon Solenoid (CMS) will also be getting an upgrade. With this upgrade, it is important to understand the full capabilities and limitations of the tracker & trigger to read and store data about particles of interest. The following study details the losses of data due to limitations on the CMS Binary Chip (CBC). CMSSW 10.4.0 was used to simulate and analyze a sample of 500 events for stub losses in the barrel of the CMS due to CBC limitations. It was found that stubs from secondary reactions were consistently the highest volume of stubs that were lost due to a CBC failure in each of the layers and that layers 4, 5, & 6 had higher losses in comparison to losses in layers 1, 2, & 3.

1. Background

1.1 The Compact Muon Solenoid

The Compact Muon Solenoid (CMS) is one of seven experiments found at the LHC. The CMS is designed to detect and store data about the products of a high-energy collision. This is achieved using a solenoid with a magnetic field greater than 100,000 times than the earth's [2].

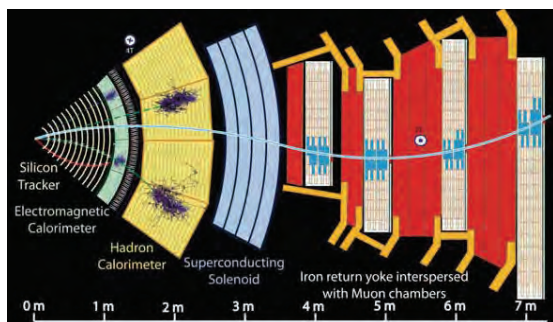


Figure 1: Layers of the CMS detector [1]

Figure 1 illustrates the many layers of the CMS

detector. Each layer takes precise measurements of different types of particles. The following study is concerned with the tracker of the detector, which tracks and stores data about the path of particles as they go through the layer.

The tracker is the innermost layer of the CMS which allows it to catch all of the particle spray that occurs from an event. The tracker can be divided into four subsections: Tracker Inner Barrel (TIB), Tracker Outer Barrel (TOB), Tracker Inner Disk (TID), and Tracker End Caps (TEC). Each subsection's location can be described by the radial distance from the center of the CMS detector (r), the linear distance down the center of the CMS detector (z), and pseudorapidity (η). The following study examines the TOB. Figure 2 shows a cross section of the tracker labeled with each of the subsections described. TOB is located where $r > 550$ and $z < 1200$

TOB has six layers of detector modules which are represented by lines in Figure 2. Each detector module is made up of two parallel silicon sensors. The first three layers use PS modules which use a strip sensor and a pixel sensor. The last three layers contain 2S modules which are simply made of two identical strip sensors. In comparison, PS modules have a higher granularity and provide higher precision hits which helps with the high levels of occupancy in the inner three layers [3].

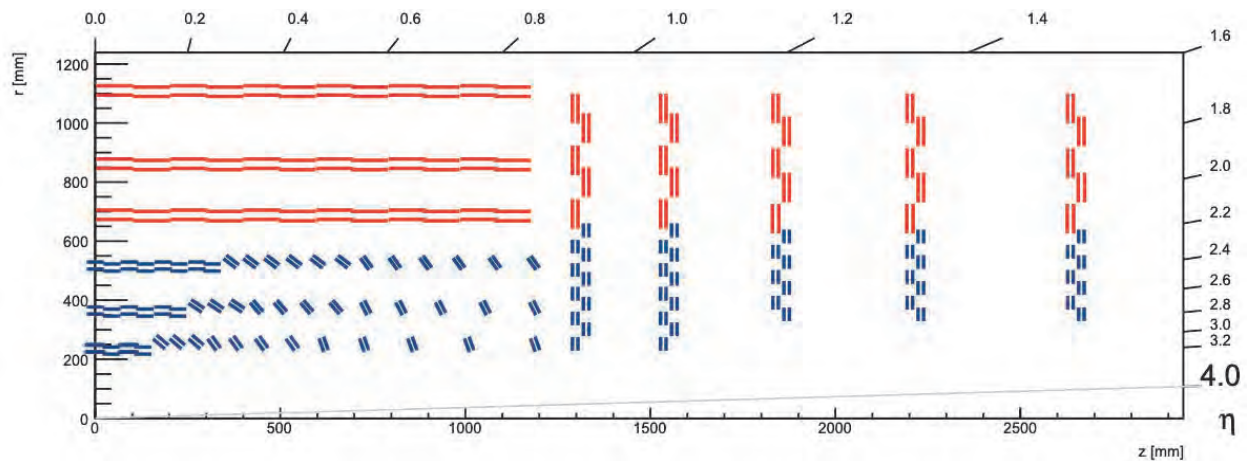


Figure 2: Schematic cross section through the CMS []

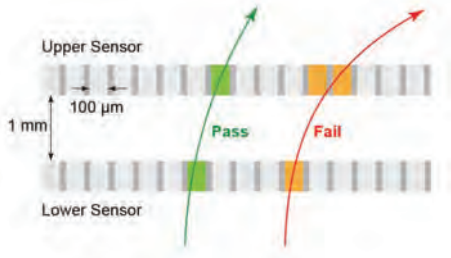


Figure 3: Stub schematic [3].

When a collision occurs, an electric signal is produced as a particle passes through pixels or strips creating a cluster. Correlated clusters in the parallel detectors within a module become reconstructed by CMS Binary chips (CBC) or Macro Pixel ASIC (MPA) chips to

create stubs; CBC are used with 2S modules while MPA chips are used for PS modules.

Figure 3 shows the concept of a stub and explains how stubs can be used to significantly reduce the enormous inflow of data. The transverse momentum (p_T) of a particle is directly related to the width of the stub that it creates. A cut-off p_T can easily be applied by examining the deviation of the second cluster and the implied momentum. As figure 3 suggests, a high p_T cut-off will cause certain particle paths to fail rejecting those stubs. Since CBC/MPA chips only readout stubs, this rejection of stubs helps reduce the flow of data coming in significantly.

Though stubs can reduce the amount of data coming in, there are still losses due to failures in the CBC readout chip. The CBC has a buffer that can be filled up when there is too much data which causes the data that does not make it into the buffer to be lost. Figure 4 shown below offers a diagram showing the full front-end data extraction and the rates at which data is produced in each step. The following study focuses on the truncation of data done by the CBC.



Figure 4: Front-end data extraction [4].

1.2 Past Studies

In a study performed in 2018, Christopher E. McGrady set out to understand how high data rates and limits on bandwidth readout affected losses of data in the tracker of the CMS. McGrady used CMSSW 9.3.7 to analyze data that were lost and understand what conditions caused the data to be lost. It was found that TOB encountered the highest percentage of losses ranging from 1.51% to 5.58% depending on pile-up conditions [1]. Table 1 demonstrates the high percentage of data lost in TOB (barrel layers 4, 5, & 6) due to CBC limitations. The full limit of data losses were based on a sample in which there was a pile-up of 300 collisions. With the conclusions found in McGrady’s study, it was suggested that more studies should be done in order to understand why such high losses were occurring due to CBC/MPA losses.

Table 1: Stub loss from different limitations [1]

Location Loss	Full Limits	CIC Losses	CBC/MPA Losses
Layer 1 Barrel	1.36%	0.72%	0.19%
Layer 2 Barrel	1.02%	0.90%	0.04%
Layer 3 Barrel	0.17%	0.05%	0.04%
Layer 4 Barrel	3.13%	0.30%	1.39%
Layer 5 Barrel	4.34%	0.24%	2.20%
Layer 6 Barrel	5.58%	0.15%	2.95%
Layer 1 End Cap	0.94%	0.66%	0.08%
Layer 2 End Cap	1.88%	1.57%	0.11%
Layer 3 End Cap	1.67%	1.56%	0.01%
Layer 4 End Cap	1.74%	1.70%	0.01%
Layer 5 End Cap	1.39%	1.31%	0.01%

2. Methods

CMS SoftWare (CMSSW) creates samples of events and shows how the CMS detects those events. In this study, CMSSW 10.4.0 was used. Events are simulated using the Monte Carlo technique, which estimates the value of an unknown quantity through inferential statistics [6]. A sample was created where the max events was set to 500 using the

L1TrackNtupleMaker_cfg.py file which can be found in the CMSSW_10_4_0/src/L1Trigger/TrackFindingTracklet/test directory. This sample was then used to make plots using stubRate.C located in the CMSSW_10_4_0/src/L1Trigger/TrackFindingTracklet/test/code2 directory. Losses due to CBC limitations were broken up into categories of stub types in order to understand what kind of stubs were being lost.

Three types of stubs were considered in this study: genuine, combinatoric, and unknown. A genuine stub contains two hits from the same Monte Carlo truth track, while a combinatoric stub contains one Monte Carlo hit and another hit with a different ID. An unknown stub contains hits that are not differentiable.

Four-dimensional arrays were created to account for stub volumes while also keeping track of the particular stubs' location. the parameters for the arrays created were barrel, layer, ladder, and module. Table 2 provides a comprehensive list of arrays created and descriptions.

Table 2: Arrays created

Array	Description
GenuineStubs	Count of all genuine stubs in each module
GenuineStubsCBCfail	Count of genuine stubs that failed CBC in each module
CombinatoricStubs	Count of all combinatoric stubs in each module
CombinatoricStubsCBCfail	Count of combinatoric stubs that failed CBC in each module
UnknownStubs	Count of all unknown stubs in each module
UnknownStubsCBCfail	Count of unknown stubs that failed CBC in each module

The arrays shown were then used to create one-dimensional plots so that they could be analyzed visually. The plots were made using ROOT. One-dimensional plots of each type of stub were made in each layer for a stub count. The plots were then superimposed into stacked histograms so that the full population of stubs could be seen while also knowing how many stubs belonged in each category.

3. Results

Figures 5, 7, & 9 show a count of stubs per module in each layer of TIB on a logarithmic scale. The different colors represent the stub type; Red represents unknown stubs, green shows combinatoric stubs, and blue is for genuine stubs. Similarly, Figures 6, 8, & 10 show the count of stubs that were lost due to a CBC failure broken up in colors again by stub types in layers of TIB. TOB is represented by Figures 11-16.

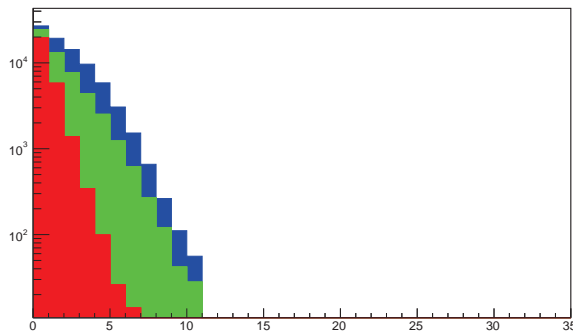


Figure 5: All stubs layer 1

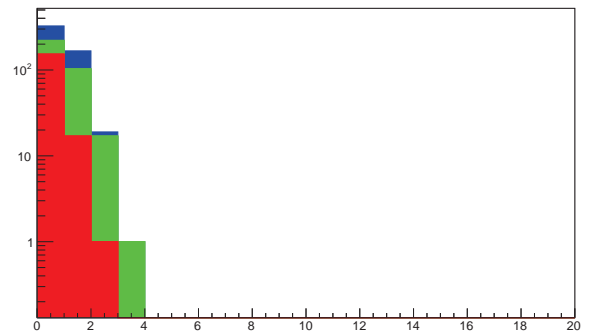


Figure 6: CBC failed stubs layer 1

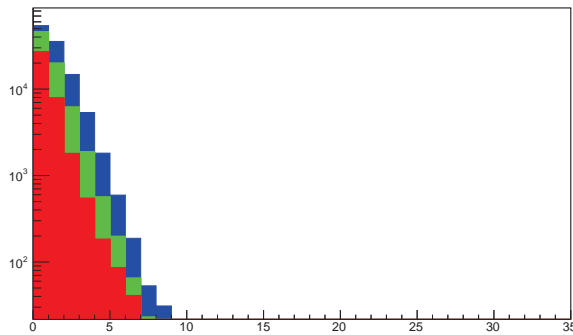


Figure 7: All stubs layer 2

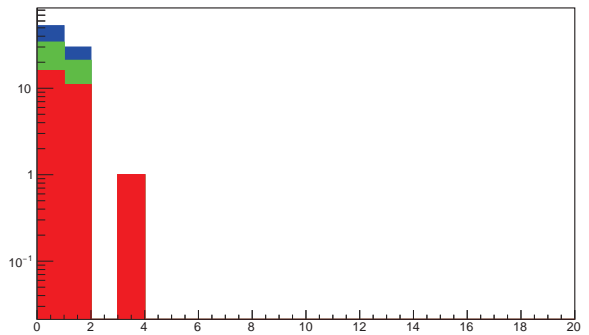


Figure 8: CBC failed stubs layer 2

Legend:

- Genuine
- Combinatoric
- Unknown

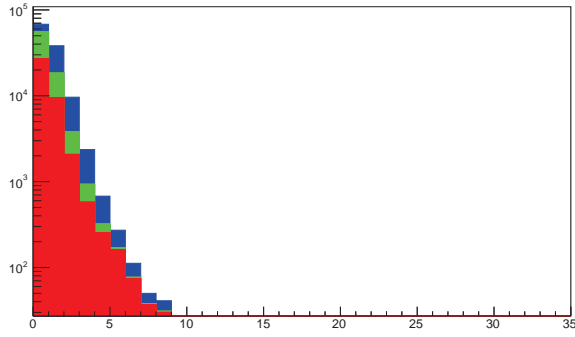


Figure 9: All stubs layer 3

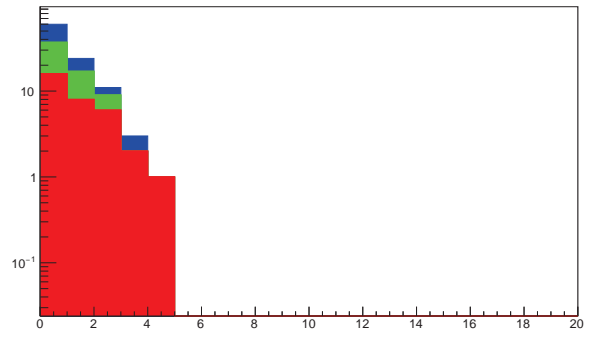


Figure 10: CBC failed stubs layer 3

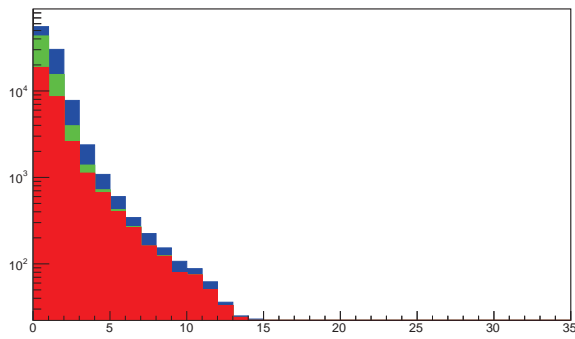


Figure 11: All stubs layer 4

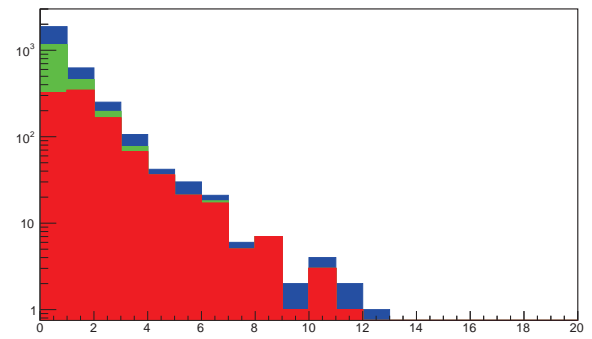


Figure 12: CBC failed stubs layer 4

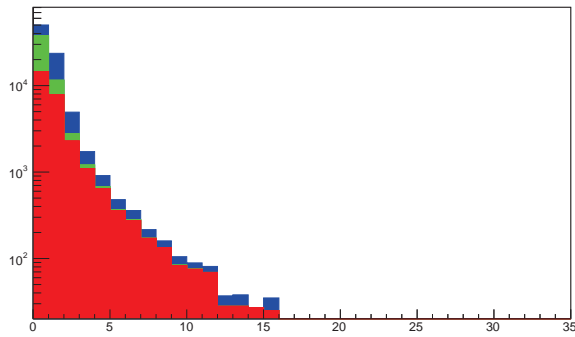


Figure 13: All stubs layer 5

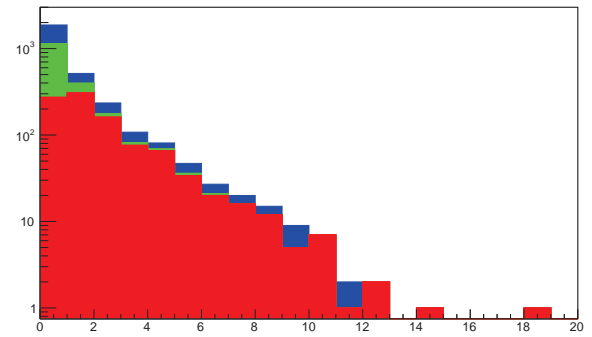


Figure 14: CBC failed stubs layer 5

Legend:

- Genuine
- Combinatoric
- Unknown

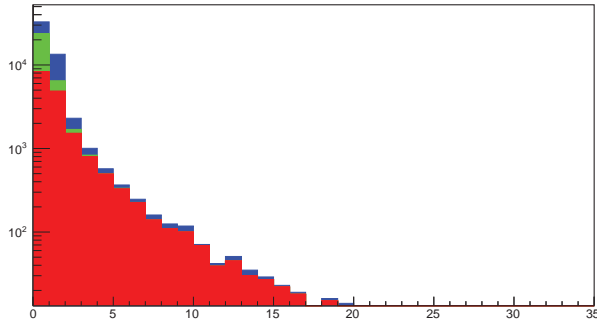


Figure 15: All stubs layer 6

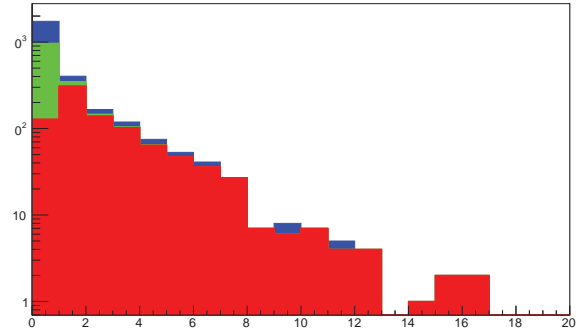


Figure 16: CBC failed stubs layer 6

Table 3 seen below shows the total amount of stubs and stub losses due to a CBC failure.

Table 3: Count of total stubs and stub layers

	Total Stubs	Losses due to CBC failure
Layer 1	27262	171
Layer 2	37536	28
Layer 3	39853	33
Layer 4	32888	991
Layer 5	27731	982
Layer 6	17158	887

4. Discussion

The population of unknown stubs grew to be the majority of all stubs when progressing through the layers. Unknown stubs were also the majority for stubs that were lost due to CBC failures in each of the layers. However, there is a distinct increase in the sheer amount of CBC losses when comparing TOB to TIB.

The amount of CBC failures in the first three layers decrease when moving outwards (from layer 1 to layer 3) from the collision point. Although the CBC failures decrease from layers 1 to 3, the amount of total stubs increases by nearly a factor of 1.46. This is shown in Figures 5-10 and in Table 3. Moving from layer 3 to 4, the amount of total stubs decreases a little

bit but the population of stubs that are lost from a CBC failure increases drastically. In layer 3, there are only 33 stubs lost to a CBC failure. In layer 4 there are 991 stubs lost from a CBC failure which is an increase of a factor of about 30. This is shown in Table 3 and in Figures 9-12.

The low amount of CBC failures in layers 1-3 can be attributed to the fact that these layers use an MPA chip to reconstruct stubs while layers 4-6 use CBC chips to reconstruct stubs. The CBC failures in each of these cases were mostly unknown stubs which can account for why the track efficiency in layers 4-6 are high despite the high loss of stubs.

In further studies, The performance of the MPA chip should be looked at and compared to the performance of the CBC chip. Ways to improve losses in TOB should also be researched by looking into other data compression methods.

References

- (1) McGrady, C. E. (2018). *Using particle interaction simulations to understand tracker efficiency for the phase II high luminosity upgrade on the cms experiment* (National Science Foundation). Indiana, United States: Notre Dame University, Physics.
- (2) Taylor, L. (2011, November 23). *What is cms?* Retrieved from <http://cms.web.cern.ch>
- (3) Viret, S. (2018). *Stubs*.
- (4) Viret, S. (2017). *Data transmission efficiency of the phase II tracker front-end system for the tilted geometry*.
- (5) The CMS Collaboration *et al* 2008 *JINST* **3** S08004
- (6) Guttag, J. [MIT OpenCourseWare]. (2017, May 19). *Monte Carlo Simulation*. Retrieved from <https://www.youtube.com/watch?v=OgO1gpXSUzU>

**Improving the Notre Dame MR-TOF and using Photodiode Detectors for
Beam Analysis**

Jason Prochaska

2019 NSF/REU Program

Physics Department, University of Notre Dame

Advisor: Maxime Brodeur

Abstract

This report first discusses the use of Multiple Reflection Time-of-Flight Mass Spectrometry in analyzing Radioactive Ion Beams. Particularly, the optimal beam pulse width to maximize the Mass Resolving power of said Mass Spectrometer. The successful use of Multiple Reflection Time-of-Flight Mass Spectrometry will aid in the study of many rare nuclei that have an extremely low natural abundance here on Earth. Additionally, we discuss the use of a particle detector called Ackbar in analyzing beam contents. The Ackbar detector utilizes a small gas chamber coupled to a silicon surface barrier to identify the beam contents. This paper presents a potential replacement for the silicon detector, by a photo-diode detector, as well as a mount for said photo-diode.

Introduction

There are two major processes that create elements heavier than iron. The discussion of this paper is focused on the r-process, or rapid neutron capture process, which generally synthesizes the most neutron-rich isotopes of the heavy elements. The r-process produces approximately half of all elements beyond iron in the universe [7]. To better understand the rapid neutron capture process it is necessary to study nuclei near neutron number $N=126$. This is because nuclei around the closed neutron shells of $N=82$ and $N=126$ have a large influence on the final abundances of nuclei that are produced by the r-process [7]. However, nuclei near $N=126$ are rare given their radioactivity, and production of these radioactive nuclei presents many challenges. Multi-nucleon transfer reactions are a viable method for reaching the $N=126$ region [8]. At Argonne National Laboratory, a facility is being created

to produce these rare nuclei allowing for their study [9]. However, production of these nuclei yields contaminant isobars. In order to filter out the contaminants, a Multiple Reflection Time-of-Flight Mass Spectrometer (MR-TOF-MS) [1, 2] will be utilized in the facility at Argonne National Laboratory.

The University of Notre Dame has developed an MR-TOF-MS that has been tested and commissioned off-line. One of the main goals of this endeavor was to optimize the resolving power of the mass spectrometer.

The off-line testing of MR-TOF-MS at Notre dame utilized a Bradbury-Nielsen Gate (BNG) to chop the beam into pulses, allowing only a specified width to go on to the Mass Spectrometer. The size of the pulse can have an influence on the resolving power of the beam. In order to determine the ideal size for the width of the beam, characteristics of the detected peak were analyzed.

Implications and Advantages of the MR-TOF-MS

Argonne National Laboratory is creating a facility in which radioactive beams of high purity are required. These beams will provide insight into the astrophysical processes under which r-process neutron capture can occur. However, many experiments like specifically a mass measurement requires isobarically pure beams. Hence, a MR-TOF-MS is required to filter out isobaric contaminants (isobars are isotopes having the same atomic mass) [3]. Even isobars have slight variations in their mass. Therefore, if the ions are produced at a constant energy, isobars will travel at a slightly different velocity. Thus, the time of flight will vary

between isobars.

One of the major advantages presented by TOF-MS is the extremely short time scale on which it can separate isobars. This is of particular importance in the Argonne National Laboratory setup, as the beams produced will be radioactive in nature. Another significant advantages of the Multi-Reflection TOF-MS is the length of the device [2]. An ordinary time of flight mass spectrometer would require a significant distance for the beam to travel to achieve a sufficient resolving power. Multiple-Reflection TOF-MS traps ions within a potential well, allowing them to oscillate along the length of the chamber. This allows for a far shorter beam line as mentioned, and has the added benefit of allowing for the Time-of-Flight to be modified and optimized. The MR-TOF-MS at the University of Notre Dame utilizes two sets of 5 electrodes forming mirrors and two Einzel lenses in order to create a modifiable reflecting potential.

MR-TOF-MS Optimization

When optimizing the MR-TOF-MS we seek to maximize the resolving power, which is given by the following equation:

$$R = \frac{t}{2\Delta t} \quad (1)$$

In equation (1), Δt is the width of the peak at half the height of the peak, and t is the total time of flight of the ions. At Argonne National Laboratory the Radioactive Ion Beam will be bunched by a component prior to the MR-TOF-MS. However, we decided to analyze the optimal pulse length for the MR-TOF-MS. On the offline setup, the BNG can be opened

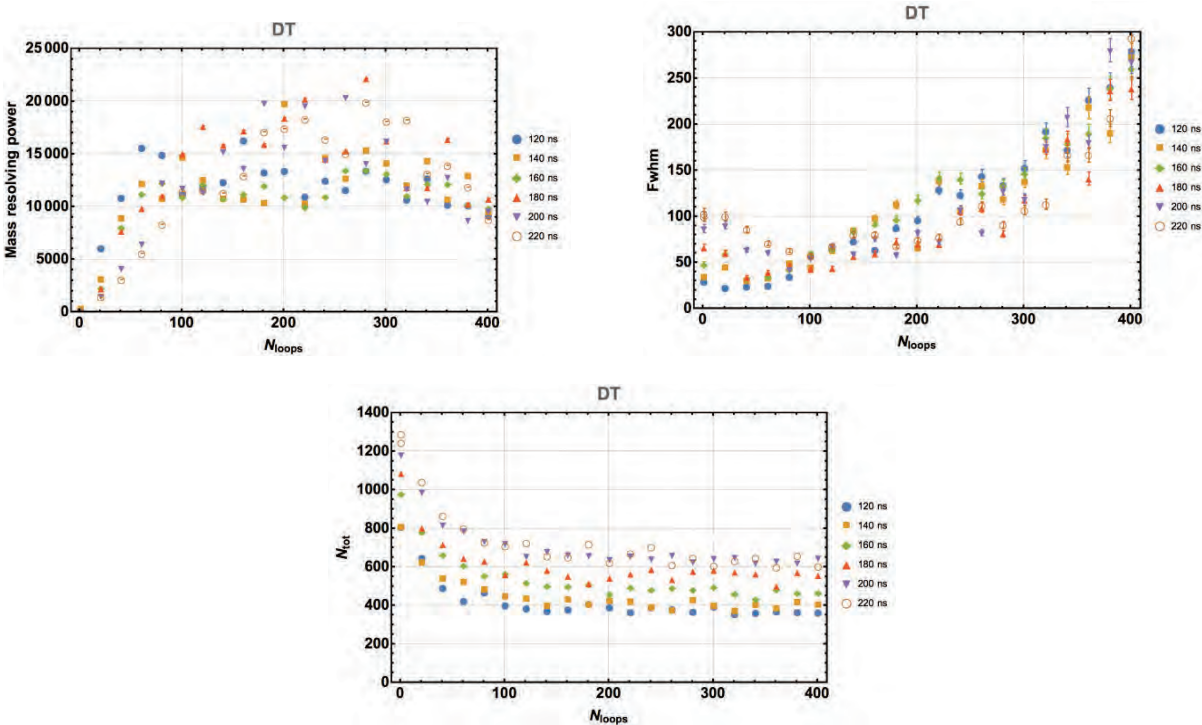


Figure 1: The above plots display the total counts, full width half maximum, and resolving power vs. the number of loops the ions are reflected. Each plot displays various pulse widths.

for a set amount of time [2]. However, it is a delicate balance between peak height and width. Too short of a pulse and less ions will get through. Also, a greater proportion of the beam will suffer from a transverse kick that will adversely affect the efficiency and resolving power. Too long of a pulse the width of the peak will be too large. The number of loops that the ions undergo determines the total distance they will travel. For all widths studied the mass resolving power and total number of ions gets affected the same way with the increased number of loops. Also the total number of ions increases with the pulse width as expected. The large drop in FWHM in the first 100 loops is due to ions entering the MR-TOF with large angles no longer being detected. The ideal resolving power is reached after 200 loops for 180 ns.

Issues Addressed and Potential Causes

Throughout measurement using the MR-TOF-MS a few issues were encountered. The first of which is that the influence of the steerer potential drifts. One possible cause for this is the varying temperature in the detector development lab. The facility at Argonne National Laboratory will be better temperature controlled, nullifying this issue. Another issue that was faced was the loss of vacuum in the system. The turbo-vacuums require a back pressure that was provided by a pure nitrogen supply. This supply ran out during the summer, and caused the system to lose vacuum briefly. Finally, the ion source seemed to die out, yielding progressively less counts and thus causing mass resolving power to plummet for high loop counts.

Testing TwinSol Contents with Ackbar

A particle identification detector, called Ackbar is used to analyze the contents of the TwinSol beams. Often these beams contain the primary beam from the FN that has scattered, the radioactive species of interest, as well as an array of isotopes that were not the intention of production. The Ackbar particle identification system allows operators to tune the beam to minimize contaminants. The Ackbar system is similar to a $\Delta E - E$ telescope detector that is built in two parts to classify the particles within the beam (see Figure 2). Particular isotopes can be identified according to their energy loss through the ionization chamber, and the final energy they deposit on the second detector. Usually for a telescope, the first of these detectors is ordinarily a thin silicone detector, which allows the incoming

particles to pass through. The first detector measures the energy loss of the particle. Within the Ackbar system the first detector is instead a gas detector, which provides three main advantages over the normal silicone detector. The first of which is it allows for detection of ions with a higher number of protons (Z). The second major advantage is the flexibility presented by varying the pressure and composition of the gas in the chamber. The most common gas utilized is P-10 gas which is comprised of 90% argon gas and 10% methane gas. The final advantage that gas detectors present is the ability to detect lower energy particles with higher accuracy. Gas detectors utilize a container with conducting walls, and is often filled with an inert gas [7]. When the ions enter the chamber they lose energy via excitation and ionization through the creation of a free electron and ion [7]. The cross-section for the latter to occur is one order of magnitude higher [7]. However, excitation reactions are generally more observed as they have a lower energy threshold than ionization processes [4]. The gaseous region of Ackbar is held under a constant applied voltage. These freed electrons then drift to the anode plate, and are detected as a current on the circuit. The second detector of the system will measure the remaining energy of the particle. The next section will discuss the two options for the final detector.

Photodiode Detector compared to Silicone Detector

Silicone detectors utilize a P-N junction diode that is put under reverse-bias [4]. This P-N junction has a depletion layer (which becomes larger in the presence of a reverse-bias) in which external particles that enter the region will deposit energy. This deposited energy

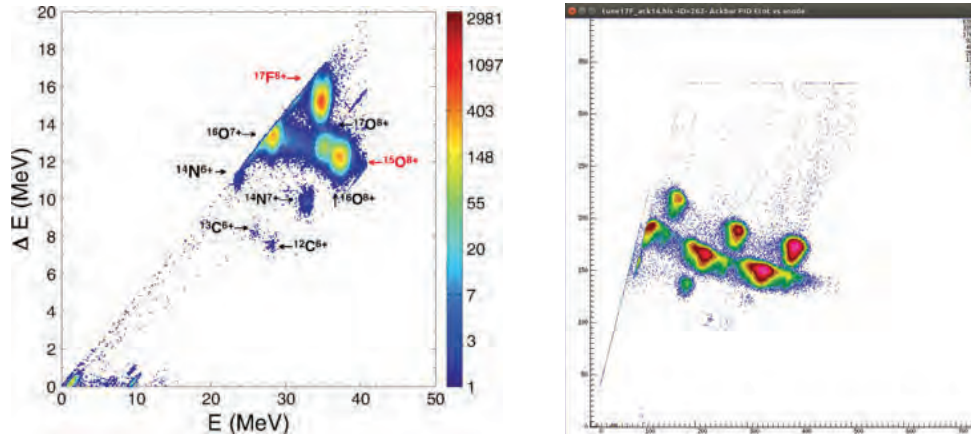


Figure 2: The lefthand particle identification plot that was created using Ackbar in it's previous telescopic form. The righthand utilizes a gaseous ionization detector to measure ΔE . The beam was produced by accelerating Oxygen-16 on a deuterium target with the goal of producing Flourine-17 for both plots. The righthand plot clearly displays a higher resolution than the previous arrangement.

creates electron-hole pairs. The N-type semiconductor collects the electrons, and visa versa for the P-type semiconductor [7]. Both of these enter the external circuit in which they can be detected. Silicone has a crystal lattice structure that vibrates when excited [8]. Photodiode detectors also utilize a p-n junction. Photodiodes utilize light as their external input. Photodiodes, however, utilize Gallium Arsenide instead of silicone, which has the benefit of bypassing the crystal lattice structure of silicone. Gallium Arsenide produces electron-hole pairs without the need for slow crystal lattice vibrations, making photodiodes more sensitive [8]. Photodiodes provide a better resolution of total energy. The main benefit of photodiode detectors is their reduced cost in comparison to silicone detectors. Photodiode detectors can be purchased for nearly a tenth of the cost of silicone detectors, and especially important given that the detectors will have a finite lifespan when exposed to accelerated beam. In the case of the Ackbar system, the ion beam will first strike a scintillation material which emits photons that will be detected in the photodiode.

Proposed Detector Mount

The following detector mount is designed such that the aluminum fixture can still support the previously used silicone detectors, but can also house the photodiode detector. The photodiode will be housed in the designed mount which will connect to the output wire (see Figure 3). The center of the photodiode will be exposed to the center of the beam. An aluminum mounting plate will be placed on top, and is designed to collimate the beam (reducing fringe effects). The righthand mount is to be fabricated out of plastic or ceramic.

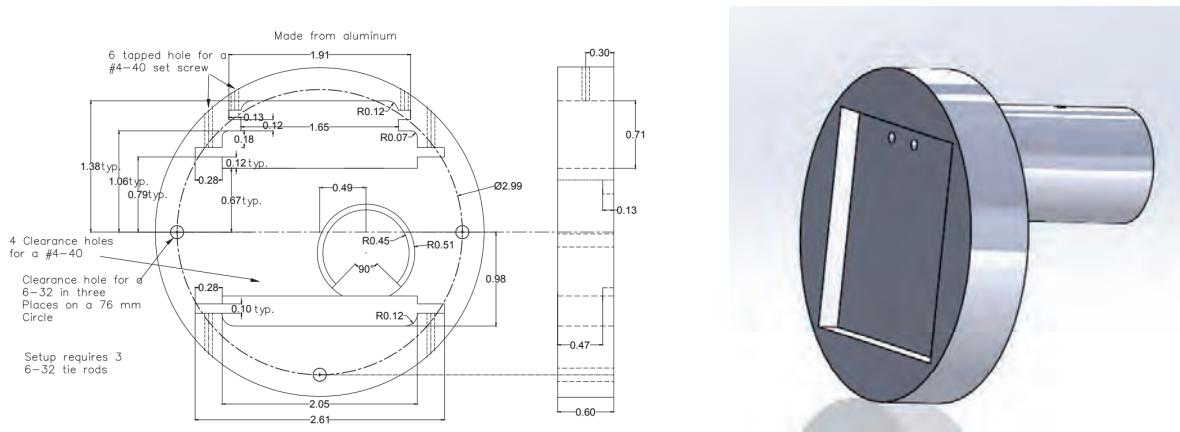


Figure 3: The lefthand plate has been designed to house a photodiode detector. The detector itself will be raised off the surface, with the back cylinder on the righthand side resting on the ridge inside the plate.

Conclusion

In this report the importance of optimizing the MR-TOF has been emphasized. The optimal pulse width was determined to be 180 ns, with a time of flight corresponding to 200 reflections. Further research into the effects of temperature on the steering potentials could

provide insight into the root cause of potential drift. However, this will likely be unnecessary for the setup at Argonne National Laboratory.

Photodiode detectors present clear advantages over silicone detectors. The cost advantage of the photodiode is significant. Further, the photodiode allows for faster data collection and will reduce detector dead-time. The manufacture of the above mounting system is still required, and then the mount must be tested with a well known beam like Oxygen-16 accelerated on a deuterium target.

References

- [1] J.M. Kelly, et al., First off-line tests and performance of the Notre Dame multi-reflection time-of flight mass spectrometer. Nuclear Inst. and Methods in Physics Research B
- [2] B.E. Schultz et al., Construction and simulation of a multi-reflection time of-flight mass spectrometer at University of Notre Dame, Nuclear Inst. and Methods in Physics Research B
- [3] Wolfgang R. Pla, Timo Dickel, and Christoph Scheidenberger. Multiple-reflection time-of-flight mass spectrometry. International Journal of Mass Spectrometry, 100 years of Mass Spectrometry.
- [4] Knoll, G.F., 2000, Radiation Detection and Measurement, Wiley.
- [5] Leo, W.R., 1987, Techniques for nuclear and particle physics experiments: a how-to approach, Springer-Verlag.
- [6] Braley, J., 2008, Photo Detectors. University of Rhode Island.
- [7] Mumpower M.R., Surman R., McLaughlin G.C., Aprahamian A. Prog. Part. Nucl. Phys., 86 (2016), pp. 86-126
- [8] Yutaka X, et al., 2015, Pathway for the Production of Neutron-Rich Isotopes around the N=126 Shell Closure., Physical Review Letters
- [9] G. Savard, M. Brodeur, J.A. Clark, R. Knaack, A.A. Valverde., 2019, Nucl. Instr. Meth. Phys. Res. B

Energy Reconstruction of Low Energy Supernova Neutrinos

Rachel Procter-Murphy
2019 REU Program
Physics Department, University of Notre Dame

Advisor: Dr. John LoSecco

Abstract

The Deep Underground Neutrino Experiment is an international experiment through the Fermi National Accelerator Laboratory that will study neutrinos. In this study, we examined at the detector effects on low energy supernova neutrinos in order to improve energy reconstruction at energies less than 40 MeV. In order to do this we looked at supernova neutrino events in a LarSoft detector simulator with and without background. We looked at the ratios between the true data and reconstructed data to identify the deficiencies of the detector, which we found to be low energies and high drift times. We also improved the ratio between the true and reconstructed data by applying the physical limits of the detector. The efficiency of the improved ratio of the clean data was 93.2% and the efficiency of the improved ratio with the data with background was 82.6%. We concluded that a second photon detector at the far wall of the detector would help improve the resolutions at high drift times and low energies.

Introduction

The Deep Underground Neutrino Experiment (DUNE) is an experiment that will study neutrinos and proton decays. Two detectors are currently being built and will be installed at the Fermi National Accelerator Laboratory and the Sanford Underground Research Laboratory. This experiment will aim to answer fundamental questions about matter, neutrinos, and the universe [4].

The DUNE detector will be installed almost 1,500 meters underground to reduce cosmic ray background. The detector consists of 17 kilotons of liquid argon each in a time projection chamber. The argon is viewed electronically with a cathode plane across from the wire collection

plane. The wire plane consists of three layers of wires in different orientations. The combination of ‘hits’ from each of these planes of wires allows researchers to reconstruct a three dimensional picture of what happens within the detector. The process of reconstruction ideally allows scientists to get an accurate representation of what happened in the detector from the digital information collected [5].

In this experiment we will study the detector effects on the data in order to improve the energy reconstruction, particularly at low energies. We specifically looked at the electron drift times which are important for energy correction and determining the coordinates of the neutrino interaction. The charge collected depends on the energy deposition so by learning about the charge and correcting for any lost charge helps us reconstruct the energy.

Neutrinos account for about 99% of the energy released from supernovae due to a process called neutrino cooling. The study of these neutrinos will allow a unique view into what is happening inside a star during its collapse.

There is a difference in the energy spectrum of actual supernova neutrinos as opposed to simulated neutrino energy spectrum is one of the main differences between the simulation [3] and what we expect from actual data.

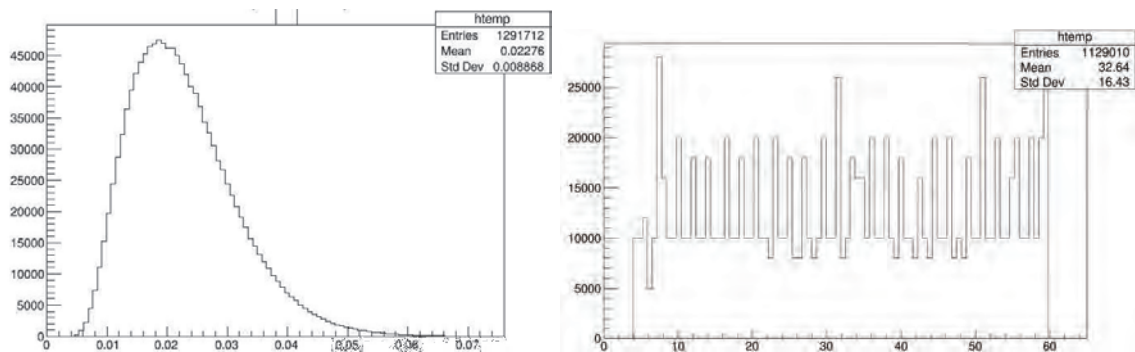


Figure 1: (Left to right) The spectrum created by the neutrino flux multiplied by the cross section in the detector in GeV; The simulation neutrino energy spectrum in (MeV).

The observed supernova neutrino energy spectrum peaks around 20 MeV, whereas in the simulation we are using, the neutrino energies are flat with the discrepancies due to binning effects.

Data

For this study we used a simulation created by Erin Conley [3] and the data without background [1] and data with background [2] that resulted from said simulation. One of the main focuses of this study was of the electron drift time (μs). The electron drift time was calculated by dividing the vertex position by the known drift velocity. The following plots show a comparison of the reconstructed drift times to the true drift times.

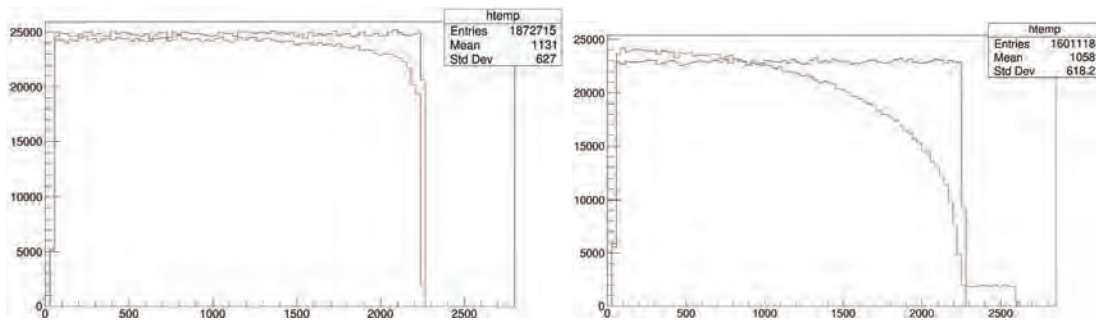


Figure 1:(Left to right) Comparing the reconstructed drift times (red) to the true drift times (blue) for clean data and data with background.

The detector seemed to have deficiencies at higher drift times that was worsened when background was added. Next, we created three dimensional histograms to compare the drift times to the true neutrino energies (MeV).

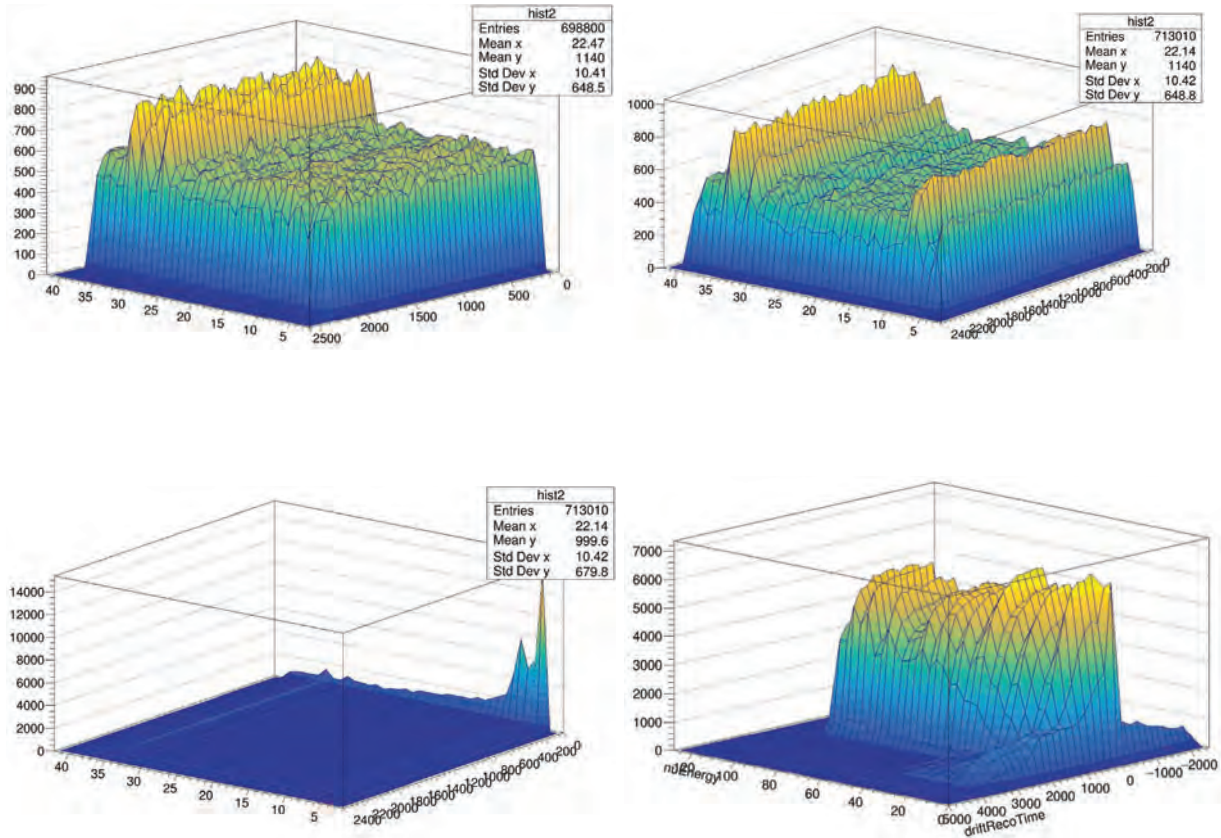


Figure 2: (Clockwise from top left) The true neutrino energies vs. the true drift time (clean); The true neutrino energies vs. the true drift time (with background); The true neutrino energies vs. the reconstructed drift times (with background); The true neutrino energies vs. the reconstructed drift times (clean).

Next we created ratios of the histograms of the true drift times divided by the reconstructed drift times. Different cuts were used to try to improve the ratio and to create histograms that are easier to read. The following plot shows the clean data with the true or reconstructed drift times (μs) compared to the true neutrino energies (MeV).

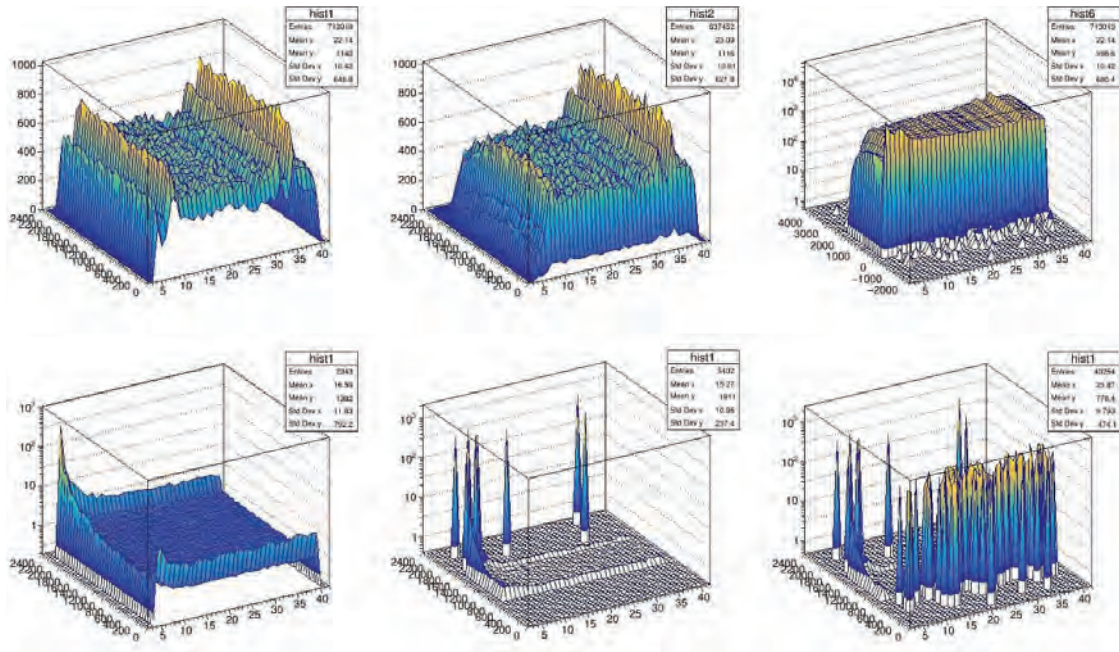


Figure 3: (Clockwise from upper left) The true neutrino energies vs. the true drift times; The true neutrino energies vs. the reconstructed drift times cut at physical bounds; The true neutrino energies vs. true drift times uncut; The ratio between the first histogram and the third histogram (uncut); The ratio between the first histogram and third histogram (cut at 0 μs to improve visibility); The ratio between the first and second histogram (cut at physical bounds).

The following shows similar plots but with background included.

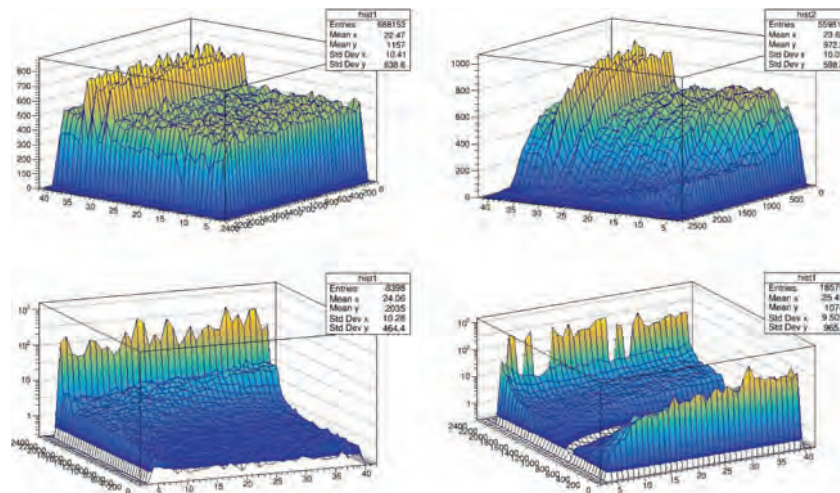


Figure 4: (Clockwise from top left) The true neutrino energies vs. the true drift times; The true neutrino energies vs. reconstructed drift times (with physical bounds); The first histogram

divided by the true neutrino energies vs. the reconstructed drift times (no bounds); The first histogram divided by the second histogram (physical bounds).

Methods

Many of the drift times for the reconstructed data (both with and without background) was outside of physical limits of the detector. To fix these inconsistencies, we added cuts to drift times that were too large to be found in the detector and cut drift times below $1 \mu\text{s}$. We also added cuts on the energy. We cut all of the data above 40 MeV and below 5 MeV. Finally we scaled the reconstructed data to account for the data that was lost in making these cuts.

Results

When these improvements were implemented some of the reconstructed data was lost. There was an efficiency of 93.2% with the clean data and an efficiency of 82.6% with the data with background. The following histograms show the improved ratios for the clean data.

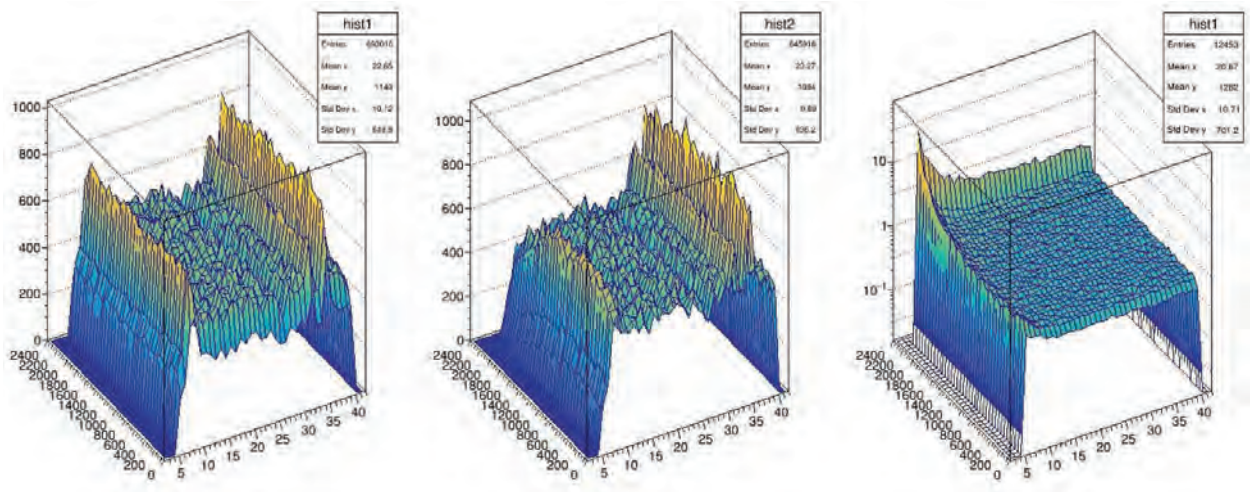


Figure 5: (Left to right) True neutrino energy vs. true drift time; Improved true neutrino energy vs. reconstructed drift time; Improved ratio between the first and second histograms.

These next set of plots show the improvements on data with background.

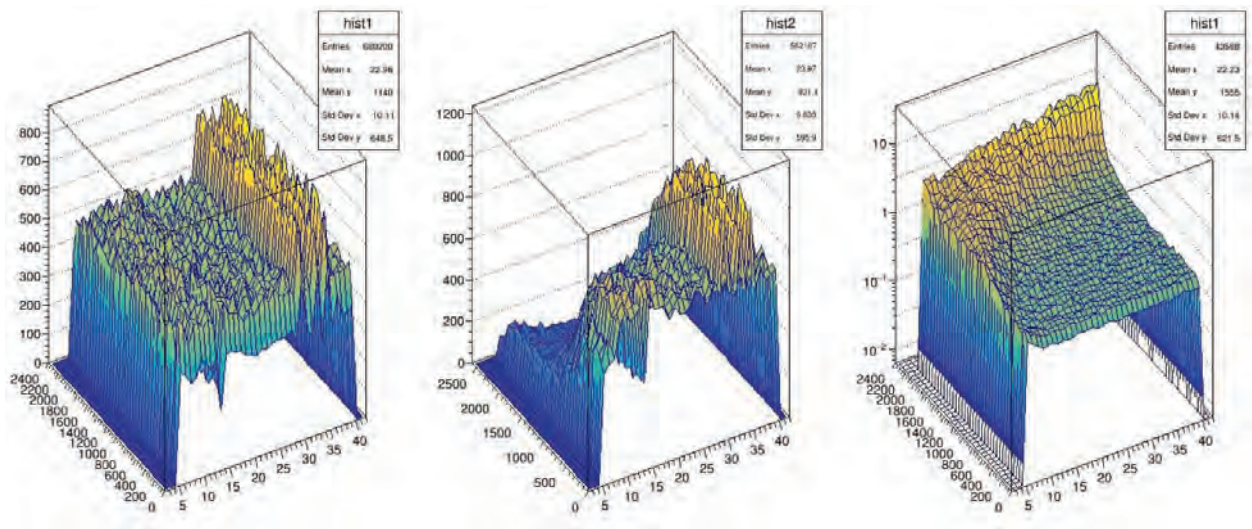


Figure 6: (Left to right) True neutrino energy vs. true drift time; Improved true neutrino energy vs. reconstructed drift time; Improved ratio between first and second histograms.

Discussion

When improving the ratio of the clean data set, the efficiency is quite good and we only lose a small fraction of the reconstructed data. However, almost 20% of the reconstructed data was lost when improving the ratio with background.

It is important to note when interpreting the previous histograms that the true drift time was divided by the reconstructed drift time so the peaks in the previous histograms highlight a deficiency in the detector as opposed to the detector over measuring a particular part of the dataset. In the clean data set, there are deficiencies at low energies and high drift times, with the greatest deficiency at the cross section of both. In the simulation with background, there is also a deficiency at low energies and high drift times. However, the deficiency at high drift times increases as the neutrino energy increases.

It would be possible to reduce the deficiencies of the detector at the high drift times if the

size of the detector was reduced to less than 2000 μs or if there was an added detector at the far wall of the detector. With a second detector the electron would never have a drift time greater than 2000 μs from either one of the detectors. Adding a second detector, while more expensive, would greatly improve the relationship between true and reconstructed drift times at high drift times without sacrificing the amount of data collected.

Conclusion

In this study, we looked at the relationship between the true and reconstructed drift times as a function of the true neutrino energy in order to further understand the detector effects on the energy resolution. The efficiency of these improvements for the reconstructed clean data was 93.2% and for the data with background was 82.6%. We created new histograms of the ratio between the true and reconstructed drift times against the true neutrino energy which reveal that there were deficiencies in the detector at low energies and high drift times. However, in the simulation with background, the deficiencies at high drift times increased at higher energies. Due to the large deficiencies in the detector at high drift distances for both the clean data and data with background, we believe that a second photon detector on the far wall would be best to improve the energy resolution.

Further Research

Unfortunately, there was more research that we did this summer than can be fit in ten pages. If you wish to read the full paper please check the dune science documents [6] or email me at rprocter@asu.edu.

References

- [1] Erin Conley. "ChargeDistEveryone_OpResim.root". June 12, 2019. [Dunevgpm10.fnal.gov.
/dune/data/users/econley.](https://dune.fnal.gov/dune/data/users/econley/)
- [2] Erin Conley. "ChargeDist_wbkg.root". June 12, 2019. [Dunevgpm10.fnal.gov.
/dune/data/user/econley.](https://dune.fnal.gov/dune/data/user/econley/)
- [3] Erin Conley. "ChargeDist_module.cc". June 12, 2019. [Dunevgpm10.fnal.gov.
/dune/app/users/econley/larsoftv082100/srcs/dunetpc/dune/ChargeDist/](https://dune.fnal.gov/dune/app/users/econley/larsoftv082100/srcs/dunetpc/dune/ChargeDist/)
- [4] Erica Snider. "Introduction to LArSoft". August, 2015. Retrieved from <https://indico.fnal.gov/event/9928/session/8/material/2/0>
- [5] An International Experiment for Neutrino Science. 2015. Retrieved from <https://www.dunescience.org/>
- [6] Rachel Procter-Murphy. *Energy Reconstruction of Low Energy Supernova Neutrinos*. <https://docs.dunescience.org>.

**Measurements on Magnetic Properties and Transport
Properties of Spintronic Materials**

BINGCHENG QING

Xi'an Jiaotong University

2019 NSF/REU Program

Physics Department,

University of Notre Dame

Advisor: Prof. Jacek K. Furdyna and Prof. Xinyu Liu

Abstract

This report explores the magnetic properties and transport properties of spintronic materials, including GaMnAsP and PbEuSe:PbSnSe:PbEuSe trilayer, using superconducting quantum interference device and Hall effect measurement. Moreover, the improvements to prevent the thermal noise in transport property measurements by using Delta mode, Pulse Delta mode and Conductance Differential mode are introduced and tested. As the result, the GaMnAsP samples show a strong ferromagnetic signal with the Curie temperature of 75K after annealing at 270°C, comparing the weak ferromagnetic signal with the Curie temperature of 38K before annealing; and the PbEuSe:PbSnSe:PbEuSe trilayer has the P-type carrier density of $2.486 \times 10^{18} \text{cm}^{-3}$ and the carrier mobility of $2319 \text{cm}^2 \text{V}^{-1} \text{s}^{-1}$.

Keywords: Spintronic, Magnetic semiconductor, Topological insulator, superconducting quantum interference device (SQUID), Hall effect, Curie temperature, Hall effect, Carrier mobility;

1 Introduction

The exploration of magnetic semiconductors and topological insulators (TI) has been continuing to gain great interest due to their potential in computer science, spintronic science and so on. The magnetic semiconductors, which are combined with the storage functional ferromagnetism and control functional semiconductivity in computer science together, can provide a new method of the computer system. As for the TI, the direction of electron flow on the surface is coupled with the spin, which can also be applied in spintronic science. There have been some experimental and theoretical researches reported,

including the spin control using GaMnAs based on spin injection [1] and the quantum anomalous Hall effects (QAHE) in magnetic doped TI. [2]. However, the application of magnetic semiconductors and TI is facing great challenges. For example, most magnetic semiconductors have a very low Curie temperature, and most QAHE is only observed at mK temperature range.

2 Method

2.1 Sample Growth through Molecular Beam Epitaxy (MBE)

Our samples are grown through MBE equipment which is a technique based on ultra-high vacuum to produce epitaxial structures with atomic monolayer control. The MBE method is firstly developed in the later 1960s at Bell Telephone Laboratories by J. R. Arthur and Alfred Y. Cho [3]. The structure of MBE is illustrated in Fig. 1. The substrate is located in a chamber with an ultra-high vacuum generated by the Turbo pump. When growing samples, the shutter of the target element cell is opened and the element is grown on the substrate. The substrate can rotate by the magnetic manipulator to ensure the uniformity of growth. A reflection high-energy electron diffraction (RHEED) system is applied to monitor the growth of samples. When a complete layer is grown successfully, the RHEED screen will perform the electron diffraction pattern, which is generally periodic bright lines. On the contrary, the RHEED screen will show a chaotic pattern when the layer is grown incompletely [4].

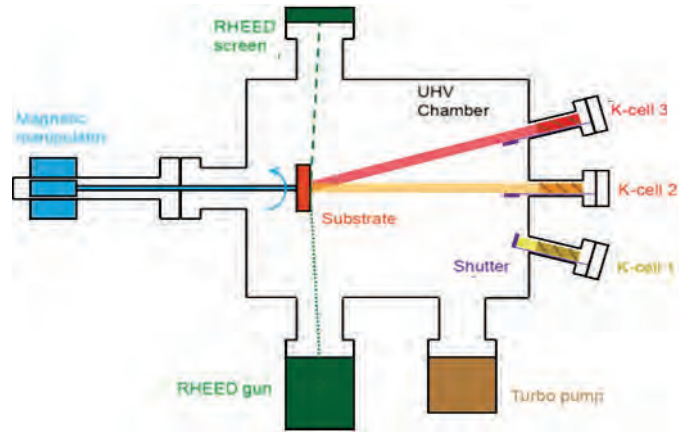


Fig. 1 MBE structure

By carefully controlling the flux of cells and the time of growth, the epitaxy structures of layers with specific thickness in nanoscale can be generated with high quality.

2.2 Magnetic Property Measurement through Superconducting Quantum Interference Device (SQUID)

Due to the tiny volume (thickness $\sim 10\text{nm}$, area $\sim 10\text{mm}^2$) of samples, the magnetic signals are very small. Thus, SQUID, a very sensitive magnetometer based on the Josephson effect, is used to measure the magnetization of samples. The SQUID structure is shown on the left of Fig. 2, and the core part of SQUID is a superconducting ring containing two Josephson junctions shown on the right of Fig. 2. Each Josephson junction consists of two superconductors separated by a very thin insulator.

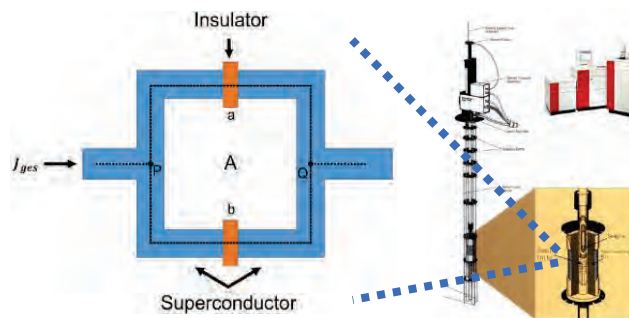


Fig. 2 SQUID structure and superconducting ring.

When applying current to the superconducting ring, the current flow through the ring is related to the magnetic flux Φ by equation 1, where q_e is the charge of an electron [5].

$$I_{ges} = I_{\max} \cos\left(\frac{2\pi q_e}{\hbar} \Phi\right) \quad (1)$$

Therefore, the magnetic flux has an interference-like relationship with current flow, which is very similar to double-slit interference in optics. When the magnetic flux changed continuously, the constructive and destructive interference of the current flow will happen in succession. Because of the large factor $\frac{2\pi q_e}{\hbar}$ in front of magnetic flux Φ , the change of current is so sensitive to the change of magnetic flux that even the change in $\frac{\hbar}{2\pi q_e}$ scale ($\sim 10^{-15} \text{Tm}^2$) can be detected.

The SQUID used in our measurement is a commercial system manufactured by Quantum Design, Inc., named Magnetic Property Measurement System (MPMS) Model XL, which is sensitive enough to measure magnetic moments of the sample as low as 10^{-9} emu [6].

2.3 Transport Measurement

The transport measurement is based on Hall bar geometry shown in Fig.3. Six contractors are applied to the sample. When the current flowing through the sample, the voltage U_{xy} and U_{xx} will be measured.

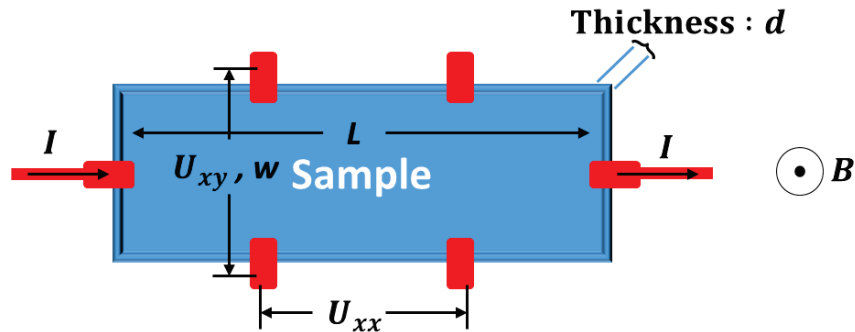


Fig. 3 Hall bar geometry

The voltage U_{xy} reveal the property of Hall resistance, which shows the carrier density.

With non-ferromagnetic materials, the normal Hall resistance is proportional to the out-of-plane magnetic field with equation 2, where n is the carrier density, B is the field applied, I is the current applied and e is the elementary charge.

$$U_{xy} = \frac{I}{ned} B \quad (2)$$

The voltage U_{xx} reveals the property of Longitudinal resistance, which is related to the carrier mobility μ with equation 3.

$$U_{xx} = \frac{IL}{wnde\mu} \quad (3)$$

3 Samples and Results

Our magnetic semiconductor GaMnAsP samples have the thickness of 62.5nm and are separated into two pieces, one is measured directly and the other is annealed at 270°C before the measurement.

By subtracting the magnetic signal of GaAs substrate, the out-of-plane and magnetizations of two GaMnAsP samples under 5K measured by SQUID are shown in Fig. 4. Before annealing, the sample shows a weak out-of-plane ferromagnetic signal, while after annealing, the sample shows a strong signal of out-of-plane ferromagnetism.

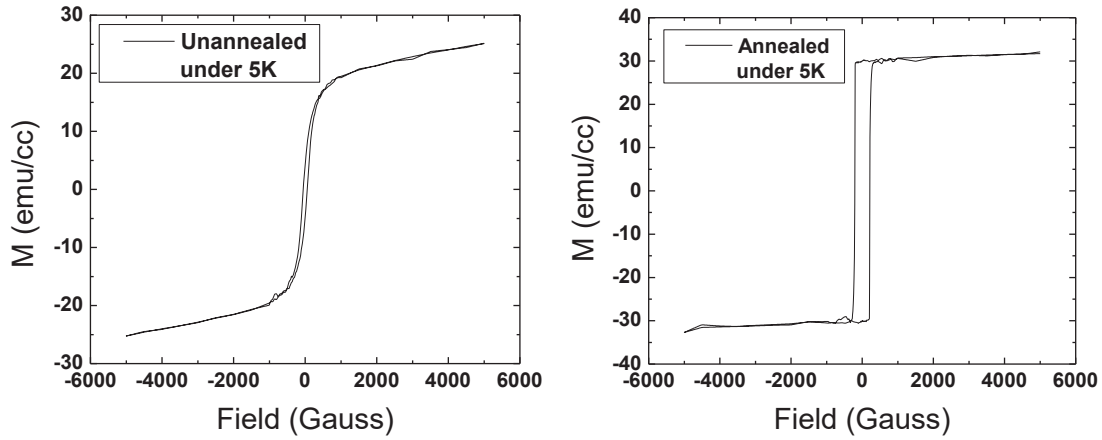


Fig. 4 Magnetizations of GaMnAsP samples

The magnetizations under the field of 25 Gauss with different temperature are measured as well and shown in Fig. 5. After annealing, the Curie temperature rises from 38K to 75K.

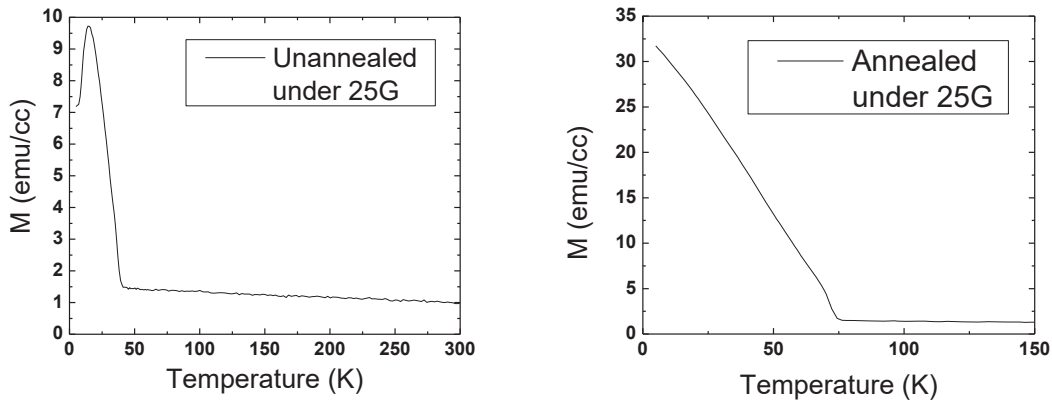


Fig. 5 Magnetization with different temperature

The transport properties of the topological insulator PbEuSe:PbSnSe:PbEuSe trilayer samples are measured. The relationship between field and Hall voltage of PbEuSe:PbSnSe:PbEuSe trilayer is shown on the left of Fig. 6. A linear relationship is observed because the ferromagnetism of the trilayer disappeared at 300K. By linear fitting, it is obtained that the carrier density is $n = 2.486 \times 10^{18} \text{cm}^{-3}$ and the trilayer is a p-type

semiconductor. The longitudinal voltage under 10K is shown on the right of Fig. 6, which shows that the longitudinal resistance increases when magnetic field goes beyond zero. The carrier mobility is $2319\text{cm}^2\text{V}^{-1}\text{s}^{-1}$.

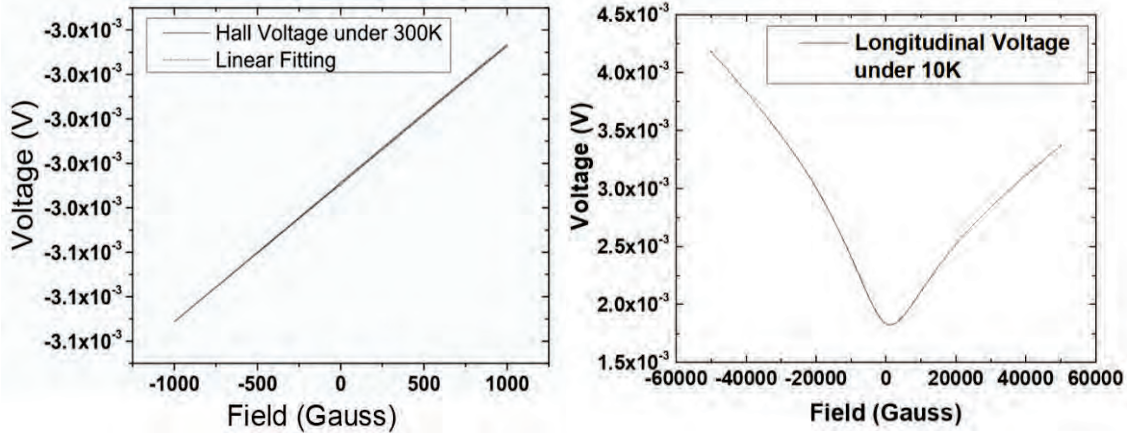


Fig. 6 Transport measurement

4 Discussion

It is observed that the ferromagnetism is enhanced by annealing for GaMnAsP. It can be explained by the dramatic change of carrier density after annealing. Such dramatic change strongly strengthens the out-of-plane anisotropy magnetic of GaMnAsP, thus the ferromagnetism and Curie temperature will be both enhanced by annealing.

When measuring the Hall voltage, the signal is on the scale of several millivolts. With such a small scale, the thermal noise is not neglectable. Considering the thermal noise in a short time, it is reasonable to approximately use a timely linear equation to describe the thermal noise. With such approximation, three methods are used to prevent the influence of thermal noise in transport measurement, including Delta mode, Pulse Delta mode and Conductance Differential mode [7].

After measuring the same sample under the same condition 100 time with each of the three

modes and traditional DC mode, the averages and standard deviations of the 100 measurements are shown in Fig. 7. It can be seen that the averages and standard deviations of those three modes is smaller than that of DC mode, which means the averagely positive thermal noise is subtracted in those three modes.

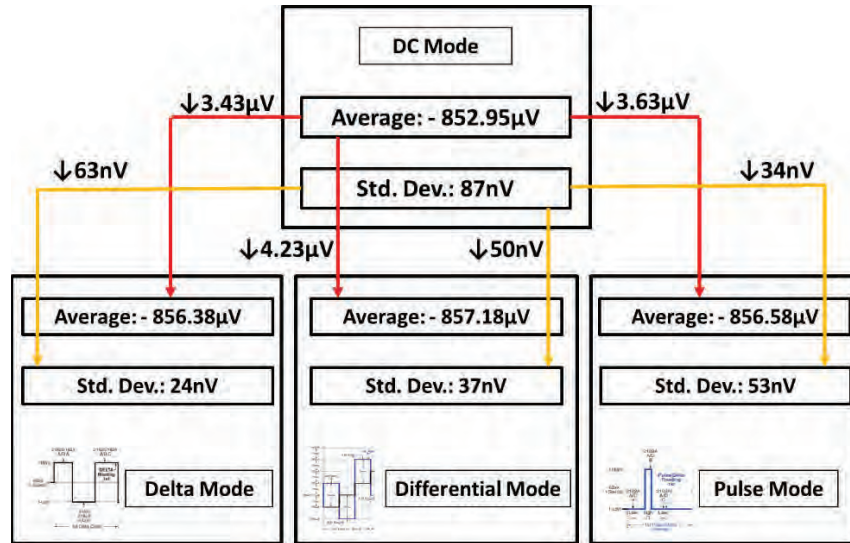


Fig. 7 Comparison between different modes

5 Conclusion

The study explored the magnetic property of magnetic semiconductor GaMnAsP and transport properties of the topological insulator PbEuSe:PbSnSe:PbEuSe trilayer sample. According to the data obtained by SQUID, the GaMnAsP sample shows weak ferromagnetic signal with Curie temperature of 38K before annealing but strong ferromagnetic signal with the Curie temperature of 75K after annealing. Moreover, with the data obtained by Hall effect measurement, PbEuSe:PbSnSe:PbEuSe trilayer is a P-type semiconductor with the carrier density of $2.486 \times 10^{18} \text{cm}^{-3}$, and has the carrier mobility of $2319 \text{cm}^2 \text{V}^{-1} \text{s}^{-1}$.

6 Acknowledgement

I would like to thank Prof. Jacek K. Furdyna for receiving me as his REU student and his generous help, and Prof. Xinyu Liu for his careful guidance on my REU project. Moreover, Prof. Seul-Ki Bac, Prof. Sanghoon Lee and Jiashu Wang are also strongly thanked for helping me. I should also thank Prof. Umesh Garg and Lori Fuson, as well as the University of Notre Dame and Xi'an Jiaotong University for providing me such a chance to experience research. Finally, I would thank my family, friends and girlfriend for their supporting.

Reference:

[1] Ohno, Y. et al. Electrical spin injection in a ferromagnetic semiconductor heterostructure. *Nature* 402, 790–792 (1999).

[2] Kou, X., Guo, S. T., Fan, Y., Pan, L., Lang, M., Jiang, Y., ... & Wang, Y. (2014). Scale-invariant quantum anomalous Hall effect in magnetic topological insulators beyond the two-dimensional limit. *Physical review letters*, 113(13), 137201.

[3] A. Cho, J. Arthur, *Prog. Solid-State Chem.*, 10, 157 (1975).

[4] Herman, M. A., & Sitter, H. (2012). *Molecular beam epitaxy: fundamentals and current status* (Vol. 7). Springer Science & Business Media.

[5] Leiner, J. et al. (2012). Exchange coupling in the ferromagnetic semiconductor GaMnAs. *Dissertations & Theses - Gradworks*, 8(2), 1120-1120.

[6] Quantum Design. (2011). *Magnetic Property Measurement System – MPMS®-XL* [Brochure].

[7] Model 6220 DC current source, model 6221 AC and DC current source user's manual (2005)

Low-energy electron interactions with triatomic molecules: CO₂ and H₂O

Melissa Quevedo Lopez

2019 REU Program

Department of Physics, University of Notre Dame

Advisor: Prof. Sylwia Ptasinska

Abstract

Low energy electron interactions with triatomic molecules: CO₂ and H₂O were studied using a crossed electron/neutral beams technique in combination with a quadrupole mass spectrometer (QMS). The QMS can be used for compound analysis by measuring mass spectra. In addition, energy and time dependencies can be measured for a specific ionic fragment and presented as ion yield curves as a function of electron energy or time. In this project mass spectra were determined for each molecule, for carbon dioxide an energy of 70 eV was used and for water 50 eV. The appearance energies (AE) were also obtained for positive ions and dissociative electron attachment resonances for negative ions formed due to electron impact on both molecules.

Introduction

When high-energy radiation (photons, ions, electrons) interacts with the matter, a high flux of secondary low energy electrons (LEE) is produced. These electrons can then efficiently trigger various dissociative processes and chemical reactions [1]. When an electron is incident on a generic molecule AB, it may lead to molecular dissociation in one of three reaction pathways: electron impact excitation (occurs at energies above ~ 3 eV), electron impact ionization (above 10 eV) and electron attachment (typically occurs at energies below 15 eV). In the last reaction pathway, i.e., electron attachment, a temporary negative ion (TNI) is formed. This reaction channel is perhaps the most important, as it is exclusive to electron induced fragmentation. Dissociative electron attachment (DEA) processes are applied to cross-disciplinary research areas: atmospheric and planetary atmosphere physics, astrochemistry (formation of molecules

in space) [3], semiconductor plasmas for manufacture of computer chips [4], radiation damage of DNA and cellular material [5], nanotechnology and surface engineering. Studies on near-threshold single and dissociative ionization of polyatomic molecules help to uncover the role of initial energy dissipation during electron–molecule interaction.

Experimental Set-up

For this project a high vacuum chamber was used (base pressure of $\sim 1 \times 10^{-7}$ mbar) with a quadrupole mass spectrometer (QMS) from Hiden Analytical. The QMS is the essential component of the whole setup which can be used for compound analysis by measuring a mass spectrum (up to 500 amu), as well as energy and time dependencies for a specific ionic fragment by measuring the ion yield curves as a function of electron energy or time. Correspondingly, the QMS can be operated in Secondary Ion Mass Spectrometer (SIMS) mode and Residual Gas Analysis (RGA) mode. In SIMS mode, a proper voltage is applied on the extractor equipped on the front end the QMS to attract ions generated outside the QMS. In RGA mode a current runs through the filament in the ion source part to emit electrons and the ions are generated through the electron molecule collision in this region. Mass spectrum measurements and the ion yield were recorded by means of MASsoft. The vapor of the liquid sample or gas-phase sample is introduced into the chamber through a gassing line connecting the sample container and a stainless steel leak valve affixed to the vacuum chamber wall. Inside the vacuum chamber, the gas sample is emitted from a thin metal tube attached to the outlet of the leak valve. The molecular beam is aimed at the small aperture in the front end of the mass spectrometer. There are two electron sources in this setup. An electron gun

affixed on the side wall of the chamber can generate a well collimated electron beam crossing the molecular beam right in front the QMS or built-in ion source part situated in the front end where two oxide iridium filaments are installed. [6]

Results and discussion

Electron impact to CO₂

Mass spectrum

Fig. 1 shows the mass spectrum of carbon dioxide (CO₂) measured at an electron energy of 70 eV. The peak 16 amu can be identified as O⁺, 32 amu as CO⁺, 44 amu is CO₂⁺ and the peak 45 amu is an isotope of CO₂⁺. There is good agreement between the measured spectrum showing a several fragment ions with that reported in the NIST database [8] and also in previous studies [9].

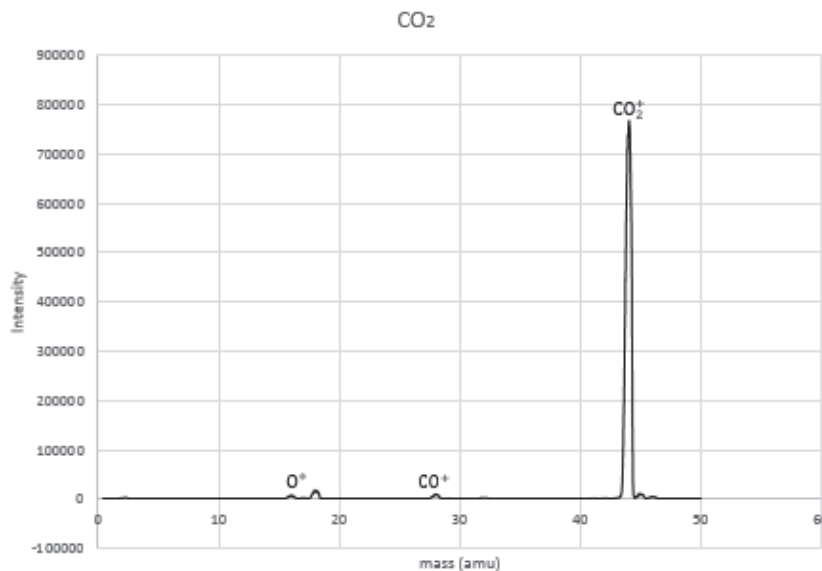


Fig.1 Mass spectrum of CO₂ obtained by 70 eV electron impact on neutral CO₂

Appearance Energies Resonances for Cations

The Fig. 2 shows the ionization efficiency curves for the parent ion, an isotope of the parent ion and two fragment ions of CO_2 . The parent ion CO_2^+ exhibits AE at 13.4 eV being the most abundant cation, the isotope of parent ion exhibits AE at 12.3 eV. The AE value of 15.5 eV corresponds to formation of CO^+ and finally the value of 18.5 eV corresponds to O^+ .

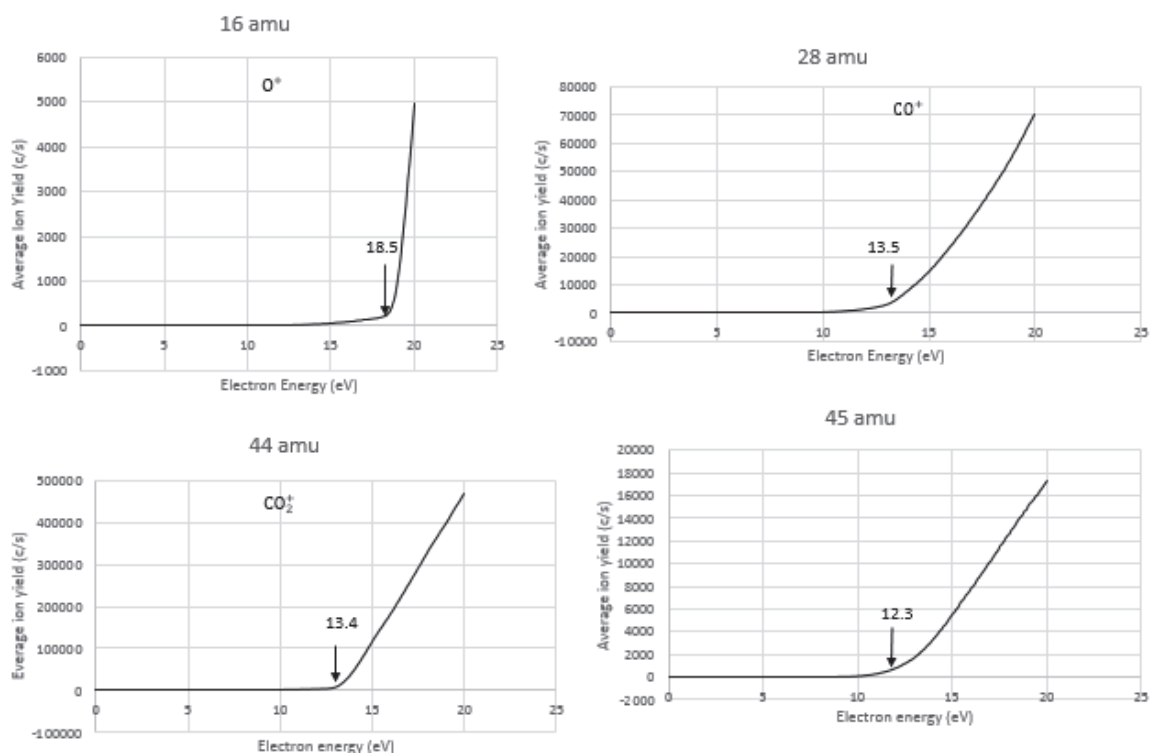


Fig.2 Fig. 2 Ionization efficiency curves for the formation of cations from neutral CO_2 by electron impact.

Table 1: Comparison of the present AEs of cations from CO₂ obtained experimentally with AEs reported previously in [11] and [7]

Cation	Mass (amu)	Present AE (eV)	Previous AE (eV)
O ⁺	16	18.5 ± 0.1	19.05 ± 0.05
CO ⁺	28	13.5 ± 0.1	14.014 ± 0.0003
CO ₂ ⁺	44	13.4 ± 0.1	13.79 ± 0.25
CO ₂ ⁺ isotope	45	12.3 ± 0.1	-

DEA Resonances for Anions

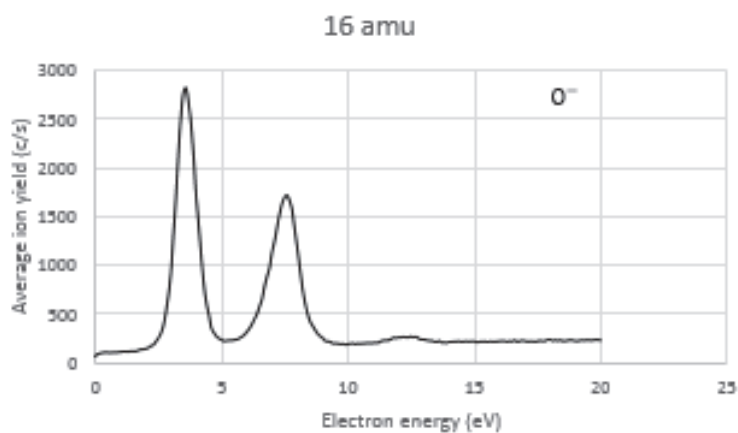


Fig. 3 Ion yield curve as a function of electron energy for the formation of O⁻ from DEA to CO₂

Fig. 3 shows the ion yield curve as a function of electron energy for the formation of O⁻ from DEA to a CO₂ molecule. The ion yield curve to O⁻ shows two significant resonances at 3.5 eV and 7.8 eV which are at similar energies and similar relative intensities as those reported previously [10].

Electron Impact to H₂O

Mass Spectrum

Fig. 4 shows the mass spectrum of water (H₂O) measured at an electron energy of 50 eV. The peak 16 amu can be identified as O⁺, the peak 17 amu correspondent to OH⁺, the peak 18 amu as H₂O⁺ and peak 19 amu corresponds to an isotope of H₂O⁺. There is agreement between the measured spectrum concerning the formation of fragment ions in this study with the mass spectrum reported in the NIST standard atomic and molecular constant database. [7]

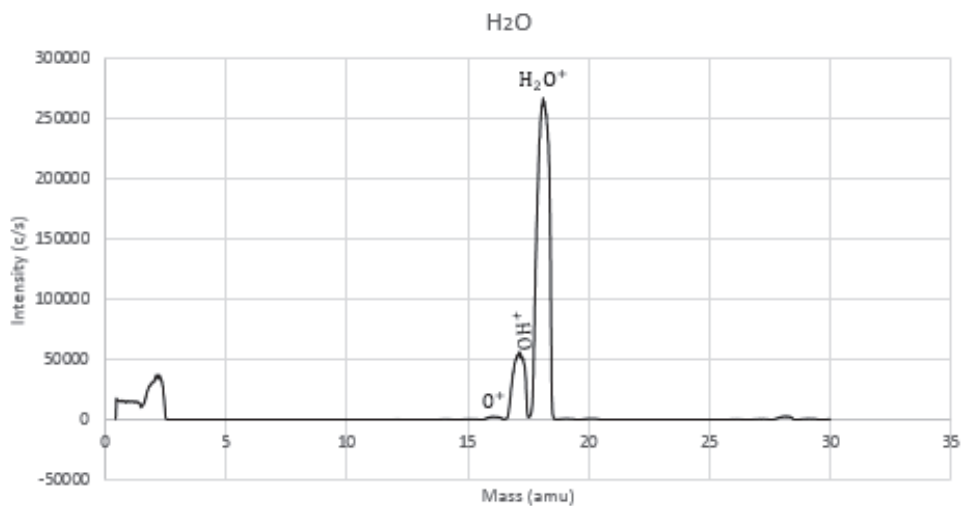


Fig.4 Mass spectrum of H₂O obtained by 50 eV electron impact on neutral H₂O

Appearance Energies Resonances for Cations

Fig.5 shows the ionization efficiency curves for the parent ion, an isotope of the parent ion and two fragment ions formed from H₂O. The parent ion H₂O⁺ exhibits AE at 12.2 eV, the lowest threshold of all

measured ionization efficiency curves, however the most abundant. The higher AE has the cation OH^+ formed at 17.9 eV. Whereas the AE 13.3 eV corresponds to O^+ formation.

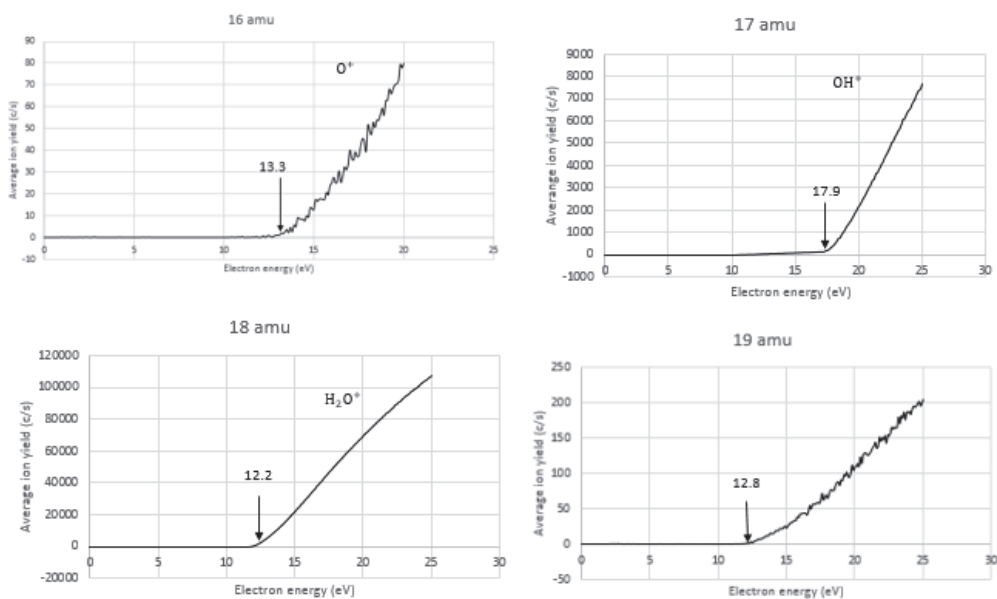


Fig.5 Ionization efficiency curves for the formation of cations from neutral H₂O by electron impact.

Table 2: Comparison of the present AEs of cations H₂O obtained experimentally with AEs reported previously [11]

<i>Cation</i>	<i>Mass (amu)</i>	<i>Present AE (eV)</i>	<i>Previous AE (eV)</i>
O^+	16	13.3 ± 0.1	13.618
OH^+	17	17.9 ± 0.1	18.115
H_2O^+	18	12.2 ± 0.1	12.58
H_2O^+ isotope	19	12.8 ± 0.1	-

Fig. 6 shows the ion yield curve as a function of electron energy for the formation of O^- from DEA to a H_2O molecule. The ion yield curve to O^- shows three resonances at 6.3 eV, 8.3 eV, and 10.3 eV, which are in good agreement with an earlier report [8].

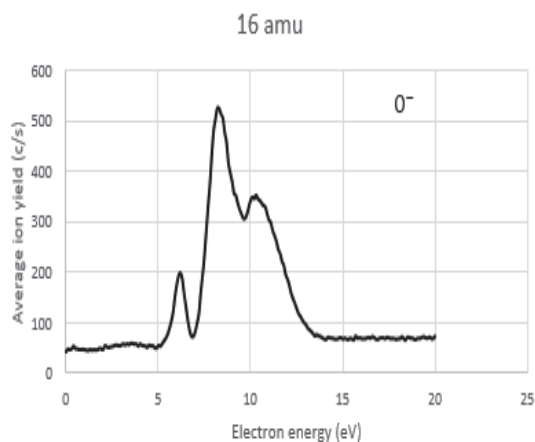


Fig. 6 ion yield curve as a function of electron energy for the formation of O^- from DEA to H_2O

Conclusions

The results obtained in this project show that for the mass spectra of both molecules, there is agreement between the measured spectrum concerning the formation of fragment ions with the NIST standard atomic and molecular constant database and different papers. The AEs and DEA resonances obtained for both molecules occur at very similar energies to those reported in the literature.

References

- [1] L. A. Sala, Low-Energy Electron Induced Chemistry in Supported Molecular Systems, Ph.D Thesis, University of Paris-Saclay, 1 (2018)

- [2] Zhu, Jane, The Dynamics of Electron-Induced Formation of N⁻² and N⁻³ Species from Condensed Ammonia, Honors Thesis Collection, 5-6 (2016).
- [3] M.C. Boyer et al. J. Phys. Chem. C, 2014, 118, 22592.
- [4] F.H. Ommarson et al. Angew. Chem. Int. Ed, 2014, 53, 12051.
- [5] E. Alizadeh & L. Sanche, Chem. Rev. 2012, 112, 5578
- [6] Zhou L Kasttner, Dissocitive electron Attachment to gas phase biomolecules, University of Notre Dame, 41, (2017).
- [7] NIST chemistry web book, available at: <http://webook.nist.gov>.
- [8] Prashant Rawat et al 2007 J. Phys. B: At. Mol. Opt. Phys. 40 4625.
- [9] Kaur, Parminder and Peter B. O'Connor. "Comparison of charge state determination methods for high resolution mass spectra." 2006 IEEE International Conference on Granular Computing (2006): 550-553.
- [10] S. K. Srivastava and O. J. Orient. "Double e-beam technique for collision studies from excited states: Application to vibrationally excited CO₂", (1983).
- [11] A. N. Zavilopulo, F. F. Chipev, and O. B. Shpenik. "Ionization of Nitrogen, Oxygen, Water, and Carbon Dioxide Molecules by Near-Threshold Electron Impact" (2004).

Characterization of Clover Detectors for use in fIREBall Detectors

Zarif Rahman

2019 NSF/REU Program

Physics Department, University of Notre Dame

Advisors:

Prof. Ani Aprahamian

Prof. Wanpeng Tan

Prof. Shelly Lesher

Abstract: Measurement of conversion electrons is an important aspect of nuclear structure studies. A new fIREBall (fInternal conveRision Electron Ball Array) array is being constructed by building on the existing “ICEBall” mini-orange array of SiLi detectors. fIREBall will come into existence from the replacement of the current array of six mini-orange Si(Li) detectors of ICEBall with twelve Si(Li) detectors to broaden the energy range of the detected electrons. fIREBall will be used in conjunction with two Compton suppressed Ge detectors. Compton suppression shields of Bizmuth Germanate (BGO) will be used on two clover detectors for coincidence measurements of gamma-rays and conversion electrons. I have studied the clover detectors in order to characterize their efficiencies and resolutions. They were calibrated using ^{60}Co and ^{252}Eu sources and a digital DAQ system. Each of the four crystals for each clover detector were evaluated separately and in summing of all four quadrants. This work is based on the full characterization of the energy resolution and the detection efficiency of the two clover detectors envisioned for use with fIREBall.

Introduction:

Measurement of conversion electrons is important in nuclear structure physics with importance in low-lying levels and various degrees of freedom in deformed nuclei and nuclear astrophysics. Knowing how to measure conversion electrons will be crucial in the understanding of the structure of 0^+ states in deformed nuclei, exploring the role of cluster states in light nuclei for stellar evolution, and testing the ab-initio theoretical model predictions. The Pittsburgh Internal Conversion Electron Spectrometer Array or “ICEBall” was constructed in 1993 with six mini-orange spectrometers and was a multiple element array for in-beam internal conversion electron spectroscopy. Since then, new designs have been made to increase the efficiency of mini-orange spectrometers and the acceptance window of electrons. fIREBall (Internal conversion Electron

Ball Array) will be constructed to upgrade the ICEBall system replacing the array of six mini-orange spectrometer with twelve Si(Li) detectors and two Bizmuth Germanate (BGO) anti-Compton suppression shields for use with two Germanium clover detectors at the University of Notre Dame. The new design will result in improved measurements of electrons in coincidence with gamma rays. The clover detectors will be essential in detecting the gamma rays.

A clover detector consists of 4 coaxial N-type high purity germanium crystals. A gamma ray may interact with one or more crystals in the clover detector. When it interacts with one crystal, it may deposit its full energy to the crystal. On the other hand, it can interact with multiple crystals through the process of Compton scattering and share its energy. This is why it is important to study the interaction of gamma rays with individual crystals and any possible combination of crystals.

The serial no., position, and the bias voltage of each of the crystal in the clovers are in the following tables.

Table 1. Serial No., Position, and Bias Voltage for Clover 1.

Crystal Position	Serial No.	Bias Voltage (in V)
1	40-N11538A	3500
2	40-N21518A	3000
3	40-N21456A	3000
4	40-N11539A	3200

Table 2. Serial No., Position, and Bias Voltage for Clover 2.

Crystal Position	Serial No.	Bias Voltage (in V)
1	41-N11542A	4000
2	41-N21573A	4000
3	41-N11534A	3000
4	41-N11672A	4000

Experiment:

Clover 1 was connected to a digital DAQ system following the bias voltage for each crystal from Table 1. A ^{60}Co source was used on the clover and ten minute runs were conducted using mesytec with different settings on the DAQ system. All the crystals were connected for the run. The process was repeated for clover 1 with a ^{152}Eu source and clover 2 with the same ^{60}Co source. The setting on the DAQ system that would give the best efficiency and resolution were determined. The raw data was in the zip.file format and the horizontal axis was in terms of channel numbers and not energy. The system was calibrated to convert the horizontal axis from channels to energy using linear fits.

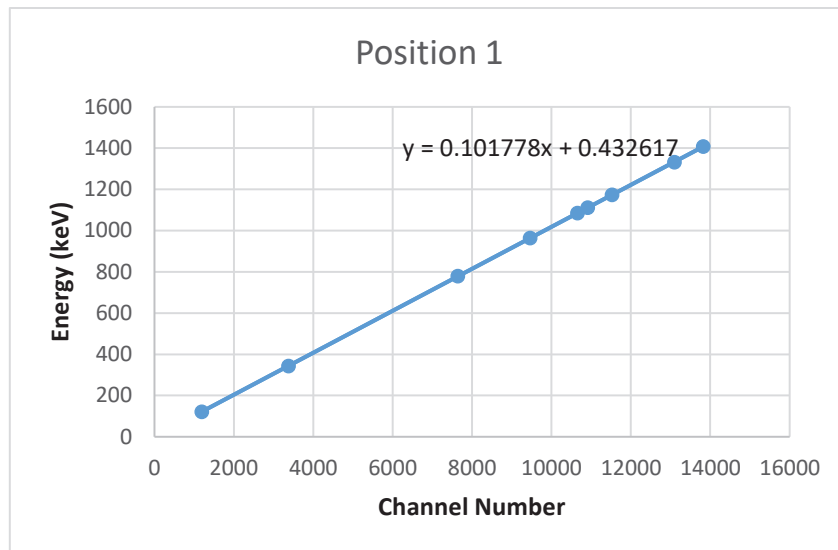


Figure 1. Linear Fit for calibration of Crystal 1 in Clover 1.

Table 3: Calibration parameters of all four crystals of clover 1 & clover 2 from linear fits where x is the corresponding channel number.

	Energies in Clover 1	Energies in Clover 2
Crystal 1	$0.101778x + 0.432617$	$0.108093x + 1.663683$
Crystal 2	$0.102023x + 0.032335$	$0.110993x + 0.907773$
Crystal 3	$0.102377x + 0.520720$	$0.109302x + 0.701314$
Crystal 4	$0.102331x + 0.191605$	$0.112284x + 0.800629$

Histograms were created for the peaks of each of the crystal and any possible combination between them. A threshold of each individual crystal is measured to be around 30 keV.

Normalized Gaussian was used to fit the peaks. Linear fit was also used to account for the background noise. The two parameters that we were interested on were area and standard deviation.

Results:

The following results were obtained from clover 1 and 2 with Normalized Gaussian:

Table 4: Characterization of Clover 1 crystals.

Combination of Summed Peaks	Peak 1			Peak 2		
	Gaussian Area	Sigma (keV)	FWHM (keV)	Gaussian Area	Sigma (keV)	FWHM (keV)
Crystal 1	2738.05	0.93	2.19	2511.9	0.96	2.25
Crystal 2	2878.51	1	2.34	2577.85	1.04	2.45
Crystal 3	3274.5	0.94	2.2	2968.25	0.98	2.32
Crystal 4	3135.31	0.94	2.21	2821.84	0.98	2.31
Crystal (1+2)	1005	1.22	2.86	945.283	1.26	2.96
Crystal (1+3)	309.397	1.23	2.89	288.288	1.26	2.97
Crystal (1+4)	1127.05	1.19	2.79	1030.75	1.25	2.95
Crystal (2+3)	1091.42	1.23	2.89	1055.09	1.28	3
Crystal (2+4)	310.01	1.24	2.92	292.26	1.3	3.07
Crystal (3+4)	1133.7	1.21	2.85	1050.77	1.22	2.88
Crystal (1+2+3)	89.3898	1.35	3.18	78.0488	1.36	3.2
Crystal (1+2+4)	85.0683	1.42	3.33	84.3758	1.33	3.13
Crystal (1+3+4)	92.1652	1.43	3.37	86.973	1.51	3.56
Crystal (2+3+4)	76.9839	1.27	2.98	77.0115	1.45	3.42
Sum (All combinations)	17352.6	1.11	2.62	15919.5	1.19	2.8
Sum (Individual Peaks)	12057.8	1.03	2.43	10907.4	1.11	2.62

Table 5: Characterization of Clover 2 crystals.

Combination of Summed Peaks	Peak 1			Peak 2		
	Gaussian Area	Sigma (keV)	FWHM (keV)	Gaussian Area	Sigma (keV)	FWHM (keV)
Crystal 1	2647.16	1.08	2.54	2282.06	1.11	2.6
Crystal 2	2492.39	0.86	2.03	2263.66	0.91	2.13
Crystal 3	2152.24	0.89	2.1	1953.84	0.92	2.18
Crystal 4	3159.72	1.43	3.37	2866.97	1.46	3.43
Crystal (1+2)	877.989	1.33	3.14	833.74	1.43	3.36
Crystal (1+3)	215.734	1.32	3.12	199.374	1.36	3.21
Crystal (1+4)	1053.54	1.79	4.22	960.956	1.82	4.28
Crystal (2+3)	791.415	1.12	2.64	767.456	1.18	2.78
Crystal (2+4)	279.308	1.59	3.74	249.727	1.58	3.72
Crystal (3+4)	906.165	1.61	3.78	855.549	1.6	3.77
Crystal (1+2+3)	65.4239	1.6	3.76	53.6534	1.51	3.56
Crystal (1+2+4)	71.1582	1.78	4.19	68.3341	1.85	4.35
Crystal (1+3+4)	56.8253	1.63	3.83	60.442	1.67	3.94
Crystal (2+3+4)	72.3703	1.48	3.5	70.2454	1.58	3.72
Sum (All combinations)	14543.1	1.2	2.82	13402.8	1.25	2.95
Sum (Individual Peaks)	10318.1	1.08	2.54	9232.45	1.11	2.61

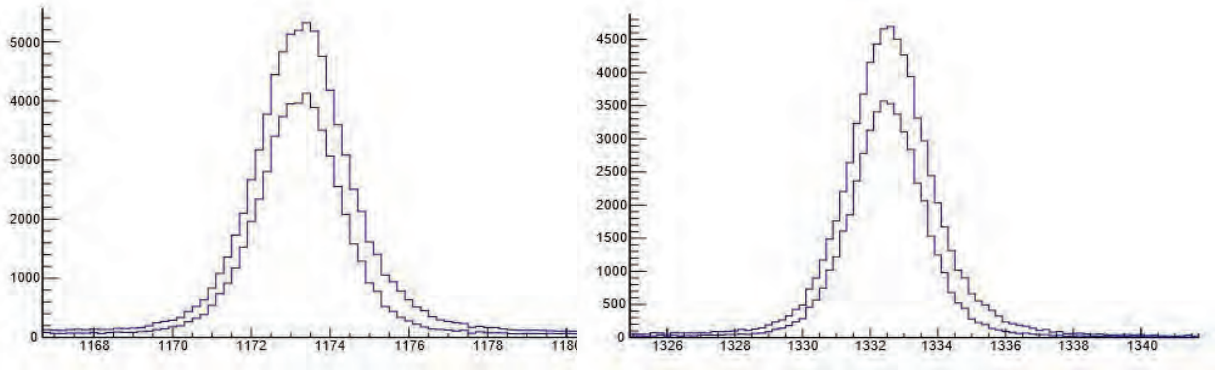


Figure 2. Normalized Gaussian fit of sum of all the combinations vs. the sum of all the individual crystals for Peak 1 & 2 of Clover 1.

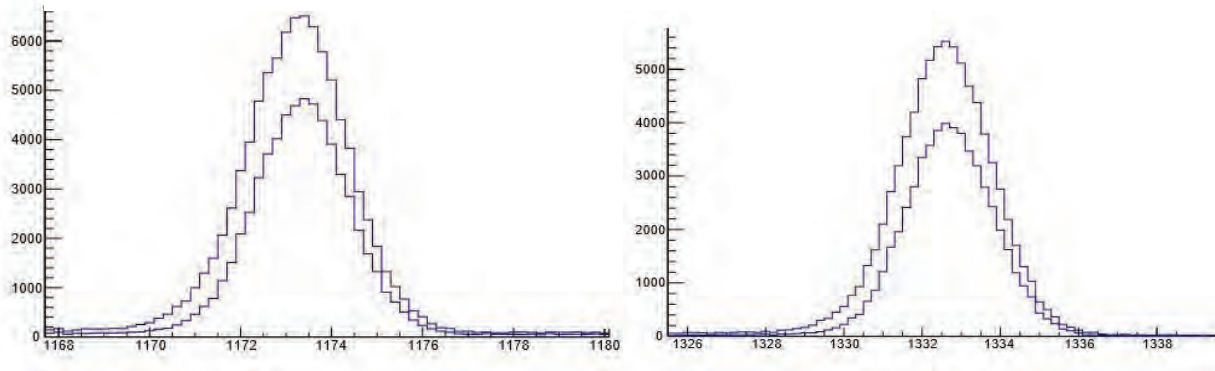


Figure 3. Normalized Gaussian fit of sum of all the combinations vs. the sum of all the individual crystals for Peak 1 & 2 of Clover 2.

When gamma rays were made to go through two crystals, less counts were attained than they were for one crystal. Similarly, when they were made to go through three or four crystals, there were even lower. At four crystals, the count was extremely small and so making a proper Normalized Gaussian fit was not practical. Thus it was not included in the table, but it was included in the sum of all the combinations. As seen from the calculation and the graphs, the sum of all the possible combinations gave a higher efficiency when compared to the sum of all the

individual crystals. However, the resolution was higher for the sum of the individual peaks than for the sum of all the possible combinations as expected.

Conclusion:

The two clover detectors at the University of Notre Dame were studied and characterized for fIREBA11 using a ^{60}Co and ^{152}Eu source. The first clover gave a Gaussian Area of 17352.6 and a resolution of 2.62 approximately for the first peak and a Gaussian Area of 15919.5 and a resolution of 2.8 approximately for the second peak for the sum of all the combination possible among the crystals. The second clover gave a Gaussian Area of 14543.1 and a resolution of 2.817 approximately for the first peak and a Gaussian Area of 13402.8 and a resolution of 2.954 approximately for the second peak for the sum of all the combination possible among the crystals. It was also observed that the sum individual modes had a better resolution, but the summing of all the possible combination had resulted in improved efficiency.

References:

- [1] M.P. Metlay, J.X. Saladin, I.Y. Lee, O. Dietzsch. 1993. The ICEBall: a multiple element array for in-beam internal conversion electron spectroscopy. 0168-9002
- [2] S.R. Leshner, A. Aprahamian, W. Tan. 2019. Proposal to purchase 12 Si(Li) detectors & 2 BGO anti-Compton shields to develop the FIREBALL spectrometer.
- [3] G. Duchene, F.A. Beck, P.J. Twin, G. de France, D. Curien, L. Hau, C.W. Beausang, M.A. Bentley, P.J. Nolan, J. Simpson. 1999. The Clover: a new generation of composite Ge detectors. *Elsevier Preprint*.

**EXTRACTION OF OPTICAL MODEL PARAMETERS FOR $^{90}\text{Zr}(^6\text{Li}, ^6\text{Li})$ AT
60 MEV/U USING A MARKOV CHAIN MONTE CARLO ALGORITHM**

AUSTIN SMITH

2019 NSF/REU Program

Physics Department, University of Notre Dame

DR. UMESH GARG

Abstract

The nuclear incompressibility is a fundamental property of nuclear matter which is critical for modeling astrophysical processes. Measurements of the isoscalar giant monopole resonance (ISGMR) is the most direct means to extract the incompressibility from finite nuclei. ${}^6\text{Li}$ can be used in studies of the ISGMR with radioactive ion beams. However, before measurements with radioactive ion beams may begin, the optical model parameters for ${}^6\text{Li}$ scattering need to be determined. To determine the optical model parameters, the elastic angular distributions of the ${}^{90}\text{Zr}({}^6\text{Li}, {}^6\text{Li})$ reaction were measured using the Grand Raiden spectrometer at the Research Center for Nuclear Physics at Osaka University. Experimental density distributions were used for the projectile and target nuclei to generate realistic volume potentials for the DWBA calculations. The optical model code, ECIS, and a Markov Chain Monte Carlo (MCMC) algorithm were employed to constrain the remaining optical model parameters for the reaction. The MCMC algorithm sampled from the 11-dimensional parameter space to visualize parameter probability distributions, from which the ideal optical model parameters were extracted.

Introduction

Nuclear Incompressibility

The nuclear incompressibility is a fundamental property of nuclear matter that can help provide insight into the dense internal environment of neutron stars [1]. It would provide information that could help determine the equation of state for these stars. K_∞ is the

most important incompressibility term for astrophysics, incompressibility of infinite nuclear matter, currently measured to be 240 ± 20 MeV [2].

$$K_A \approx K_\infty + K_{surf}A^{-1/3} + K_\tau \left(\frac{N-Z}{A} \right)^2 + K_{Coul}Z^2A^{-1/3} \quad (1)$$

Another important value is that of K_τ , the asymmetry term, and it was found to be -555 ± 75 MeV from analysis of Cd isotopes [3]. Both these values are in Eq. (1) that describes finite nuclear incompressibility K_A . As for the other terms in Eq. (1), K_{Coul} is the best known, but least important, with a value found to be 5.2 ± 0.7 MeV, and K_{surf} has no firm value [2].

$$E_{ISGMR} = \hbar \sqrt{\frac{K_A}{m \langle r_0^2 \rangle}} \quad (2)$$

The relationships in Eq. (2) and Eq. (1) allow us to measure the value of K_∞ by studying the energy of isoscalar giant monopole resonance (ISGMR) of nuclei. The strength of the ISGMR is determined experimentally with inelastic scattering; in the past, this has typically been done with ^{208}Pb and ^{90}Zr , due to their stature of doubly-magic nuclei. In measuring tin isotopes though, the strength of the ISGMR was significantly lower than predicted by theory. This tendency has been labeled as “fluffy” nuclei. In order to understand the fluffiness of nuclei, more nuclei need to be studied, including radioactive nuclei. Measuring ^{132}Sn , one of the prototypical radioactive nuclei for ISGMR studies, would be a particularly important experiment where ^6Li would be used, since it has a large proton-neutron imbalance as well as having a doubly-closed shell structure. Owing to their radioactive decay, it is difficult to prepare a target from radioactive isotopes to be used in a traditional scattering experiment. When used in inverse kinematics, the beam intensities available at modern-day radioactive isotope beam facilities are typically low, but sufficient to measure the ISGMR when the

radioisotopes are scattered off the stable targets. ${}^6\text{Li}$ is an isoscalar nucleus that can be made into a target for radioactive beams.

Optical Model

Before ${}^6\text{Li}$ can be used for radioactive beams, the optical model of ${}^6\text{Li}$ must be studied. The optical model offers a phenomenological way to model the angular distributions resulting from reactions, which then are used to extract the strength distributions of giant resonances using Distorted-Wave Born Approximation calculations and a multipole decomposition analysis [3]. The functional form of the optical model is,

$$V = V_{Coul} + V_{VOL} + V_{SURF} + i[W_{VOL} + W_{SURF}] + V_{LS} \quad (3)$$

where,

$$V_{VOL} = -V_{vol}f_v(r, R_v, a_v), \quad (4)$$

$$W_{VOL} = -W_{vol}f_{wv}(r, R_{wv}, a_{wv}), \quad (5)$$

$$W_{SURF} = 4a_{ws}W_{surf}\frac{d}{dr}f_{ws}(r, R_{ws}, a_{ws}), \quad (6)$$

$$V_{SURF} = 4a_sV_{surf}\frac{d}{dr}f_s(r, R_s, a_s), \quad (7)$$

$$V_{LS} = V_{ls}\left(\frac{\hbar}{m_\pi c}\right)^2\frac{1}{r}(\vec{L} \cdot \vec{S})\frac{d}{dr}f_{ls}(r, R_{ls}, a_{ls}), \quad (8)$$

ECIS is a optical model calculating code which is used to create a fit to angular distribution data. The code DFPD5 was used to calculate values for the real and imaginary volume potentials in ECIS at angles and the folded Coulomb part of the optical potential. The

functional form of “f”, Eq.(7) is of the Woods-Saxon form, where for ^{90}Zr $a = 0.523$ and $c = 4.911$ fm.

$$f(r, c, a) = \frac{1}{1 + e^{\frac{(r-c)}{a}}} \quad (9)$$

Markov Chain Monte Carlo Method

The principle of Markov Chain Monte Carlo (MCMC) methods is that the posterior distribution is estimated by taking simulated samples from the prior distribution. There are many types of MCMC algorithms, but the one used in this research is known as the Metropolis algorithm (see Algorithm 1). This algorithm draws samples from a probability distribution by using the full joint density function and independent proposal distributions for every parameter [4]. In Algorithm 1, $\pi(\cdot)$ represents the prior distributions, which in our case is the bounds of the parameters based on physical requirements and $q(\cdot)$ represents the likelihood based on the calculated weighted χ^2 value. The acceptance probability for a sample that increases the likelihood of matching the posterior distribution, which in our case reduces χ^2 , will be 1, so the sample will be accepted. Otherwise, a sample has a chance, based on the ratio α and a uniform distribution, to be accepted even if it increases the value of χ^2 . This allows the program, with a sufficient amount of samples, to escape local minima and find the absolute minimum within the bounded parameter space. An important part of the algorithm is the size of the steps for each parameter. These are tuned by hand to get an appropriate acceptance fraction, somewhere between 30% and 70%. This, along with a burn in phase, where the first portion of results the algorithm produces is ignored, allows the program to

reach a higher probability region of the sample distribution and provides a more reasonable posterior distribution from the accepted samples.

```
initialize  $x^{(0)} \sim q(x)$ ;  
for iteration  $i=1,2,\dots$  do  
    Propose:  $x^{prop} \sim q(x^{(i)}|x^{(i-1)})$ ;  
    Acceptance Probability::  
     $\alpha(x^{prop}|x^{(i-1)}) = \min\{1, \frac{q(x^{(i-1)}|x^{prop})\pi(x^{prop})}{q(x^{prop}|x^{(i-1)})\pi(x^{(i-1)})}\}$ ;  
     $u \sim \text{Uniform}(u; 0, 1)$ ;  
    if  $u < \alpha$  then  
        Accept the proposal:  $x^{(i)} \leftarrow x^{prop}$ ;  
    else  
        Reject the proposal:  $x^{(i)} \leftarrow x^{(i-1)}$ ;  
    end  
end
```

Algorithm 1: Metropolis Algorithm

Methods

Grand Raiden Spectrometer

The data collection for the $^{90}\text{Zr}(^6\text{Li}, ^6\text{Li})$ reaction, with the incident ^6Li at 340 MeV, took place at the Research Center for Nuclear Physics (RCNP), Osaka University, Japan. The Grand Raiden spectrometer is a high-resolution spectrometer that can measure forward angles up to 0° . This is especially useful since the cross section of the giant monopole

resonance is maximum at 0° . The data collected from the reaction is the cross section at a specific angles, ranging from 2.90° to 26.30° in 0.40° increments. For further specifications about the Grand Raiden spectrometer, see [3].

Parameter	Step Size Scale
Real Volume Normalization	0.0001
Imaginary Volume Normalization	0.0001
Real Surface Depth	0.005
Real Surface Radius	0.0001
Real Surface Diffuseness	0.0001
Imaginary Surface Depth	0.005
Imaginary Surface Radius	0.0002
Imaginary Surface Diffuseness	0.0002
Real Spin-Orbit Depth	0.005
Real Spin-Orbit Radius	0.0001
Real Spin-Orbit Diffuseness	0.0001

Table 1: The step size scale for the random walk steps for each parameter.

Metropolis Program

The Metropolis program that was developed in python can handle large ($> 10^9$) χ^2 values by rearranging the exponentials and logarithms preventing overflow errors. The program reads in an ECIS input file, inputs the parameters the program will search over, runs ECIS, then

recovers the χ^2 value from the ECIS output and that value is compared to the previous value. At the end, the program will generate a plot based on the best optical model parameters found. It also generates distribution plots of the tested parameters to provide a visual to determine if there are any correlations between parameters. The tuned step size scaled parameters are seen in Table 1, and the burn in size is set at 10% of the total number of samples. The parameters that were searched for were the normalizations for real and imaginary volume potentials, and the depth, radius, and diffuseness terms for the imaginary surface, real surface, and real spin-orbit potentials.

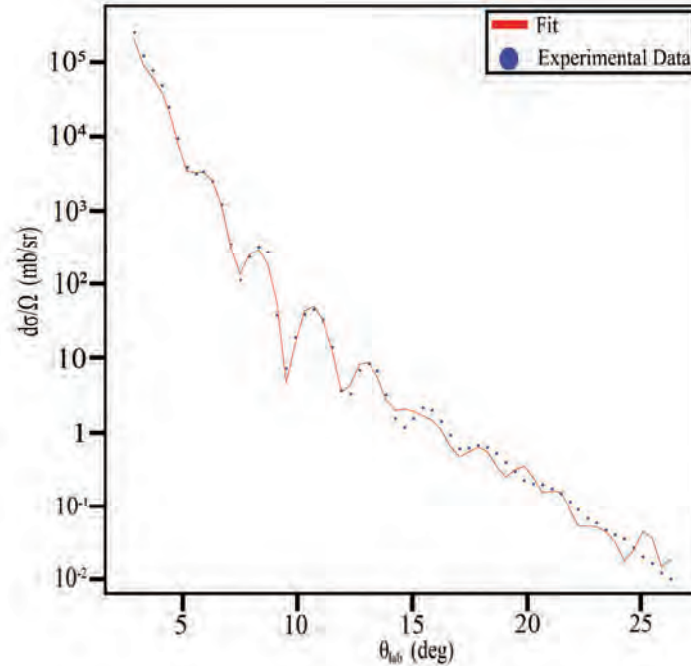


Figure 1: The fit of the data from the extracted optical model parameters.

Results

The values extracted by the Metropolis program that produced the best fit can be seen in Table 2. Figure 1 shows the fit based on these parameters with the experimental data. The χ^2 value of this fit is 27381.5, and the Metropolis program took about 7 hours to run for a hundred-thousand samples. The acceptance fraction was acceptable at 42.12%

Parameter	Extracted Value
Real Volume Normalization	-0.633
Imaginary Volume Normalization	-0.598
Real Surface Depth	-19.456
Real Surface Radius	0.785
Real Surface Diffuseness	1.566
Imaginary Surface Depth	31.098
Imaginary Surface Radius	1.072
Imaginary Surface Diffuseness	0.864
Real Spin-Orbit Depth	1.512
Real Spin-Orbit Radius	1.243
Real Spin-Orbit Diffuseness	0.744

Table 2: The final set of optical model parameters extracted by the program.

Discussion

A longer run time would also produce a better fit, since the Metropolis algorithm, given enough time, will find the best fit even if the parameters are correlated. The next step is to run this code for one or two million samples, since it is likely the program had not yet reached the stationary distribution. Additionally, the value of χ^2 seems disturbingly high, but this is due to the high precision of the measurements, which raises the χ^2 . The extracted parameters in this paper were just for the inelastic part of the $^{90}\text{Zr}(^6\text{Li},^6\text{Li})$ reaction. The next step of this research would be to expand this to also find the parameters for the inelastic optical model. Making this program more efficient would be important for the future, or exploring other algorithms to see if, in this correlated parameter space, a faster and better algorithm exists.

References

- [1] J. Piekarewicz, “Emergence of low-energy monopole strength in the neutron-rich calcium isotopes,” *Phys. Rev. C*, vol. 96, p. 044314, Oct 2017.
- [2] G. Umesh and G. Colò, “The compression-mode giant resonances and nuclear incompressibility,” *Progress in Particle and Nuclear Physics*, vol. 101, pp. 55–95, 2018.
- [3] D. Patel, “A study of the isoscalar giant monopole resonance: The role of symmetry energy in nuclear incompressibility in the open-shell nuclei,” *Springer Theses*, 2016.
- [4] I. Yildirim, “Bayesian inference: Metropolis-hastings sampling,” 2012.

**Adaptive Optics Instrumentation:
Building a Better Wave Front Sensor**

Nicholas Tusay

2019 NSF/REU Program

Physics Department, University of Notre Dame

Advisor: Justin Crepp

Abstract

Instrumentation development is a key component of observational astronomy. Since the mid-90's ground based telescopes have been using adaptive optics to improve their resolution capabilities. Adaptive optics uses real time computing to identify distortions in an incoming wave front, correct for them with a deformable mirror and then repeat the process. The industry standard is the Shack-Hartmann Wave Front Sensor (SHWFS). Technological advances in instrumentation have led to recent developments in more accurate ways of identifying the aberrations in incoming light. Combining expertise in computer science, theoretical modeling and optical systems assembly, our team is working on creating a new wave front sensor that can surpass the resolution power of the current industry standard. The non-linear Curvature Wave Front Sensor (nlCWFS) being developed will greatly enhance the capability of adaptive optics systems.

Introduction

The science of astronomy is conducted primarily by collecting light from distant sources in the universe and analyzing that data. Even close objects are very far in physical space and a high degree of precision is required to obtain usable data. Naturally, improving the resolution of the images provides better data. In some cases this can mean the difference between indiscernible noise and a verifiable signal.

Increasing resolution presents certain technological challenges. The obvious answer is to build bigger telescopes, with bigger mirrors to collect more light. The scientific community

has been doing just that, but at a certain point this becomes logistically and financially prohibitive. And because of financial and logistical issues only a limited number of the biggest telescopes can be built, which introduces supply and demand considerations for time usage.

Building bigger telescopes, however, is not the only way to increase resolution capability. Space based telescopes have the advantage of being able to resolve better images with smaller mirrors simply by collecting light before the Earth's atmosphere interferes with it. Turbulence in the atmosphere distorts and scatters incident rays of light. But space based telescopes are also prohibitively expensive and few and far between.

By being able to account for atmospheric distortions with relatively inexpensive hardware it is possible to significantly increase the resolving power of all ground based telescopes. Optical systems for this purpose have already been put into effect since the 1990s. The current industry standard employed at most major telescopes is the Shack-Hartmann Wave Front Sensor (SHWFS). It uses a lenslet array, a detector, a real time computer and a deformable mirror to analyze the atmospheric distortions, calculate how to counteract them and deform the mirror accordingly. Since it was first implemented, advances in optics, computing and the actuator hardware that deforms the mirror accordingly, have all improved the system to make this a robust method of increasing the resolution of ground based telescopes.

Since the advent of adaptive optics, advances in theory have led to a new kind of wave front sensor called a non-linear curvature wave front sensor. While the theory is more complicated and less intuitive than the Shack-Hartmann, this new sensor offers distinct advantages over its predecessor. The non-linear Curvature Wave Front Sensor (nlCWFS) uses four defocused

planes straddling the pupil to reconstruct an image at the pupil plane. This requires the use of Fourier transforms and iterative numerical analysis. Technological advances in computing power have made it possible to perform these calculations in real time, making a closed loop system feasible to construct. The nICWFS is theoretically capable of more than ten times the sensitivity of the SHWFS. [2]

Method

Adaptive Optics

The most effective adaptive optics systems work in a closed loop by splitting some of the incoming light to a wave front sensor to detect distortions in the light wave, calculate how to correct for that distortion, signal a deformable mirror to make the corrections and repeating the process as the distortions change with time. Figure 1 shows how this process flows through the system. The wave front sensor depicted is the SHWFS, though any wave front sensor can be applied in its place. The key feature is to have a closed loop system that can iterate and correct for the constantly changing aberrations in real time. This process needs to cycle on the order of microseconds in order to keep up with the rapidly changing perturbations caused by atmospheric interference. Current technology allows arrays of thousands of actuators to deform a mirror at $50\mu s$ with nanometer precision. [2] Naturally, the real time computer needs to work faster than this to calculate the wave front and communicate the correction to the actuators.

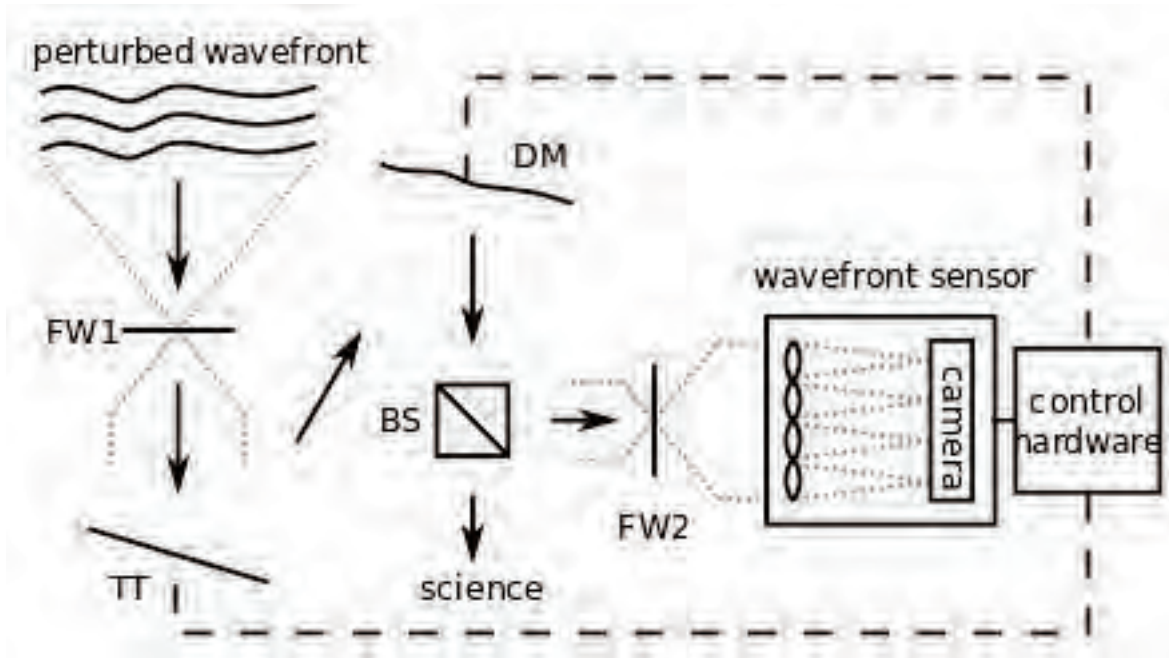


Figure 1: A typical closed loop adaptive optics system uses a beam splitter (BS) to send some of the incident light to a wave front sensor to be analyzed.

Industry Standard

The Shack-Hartmann wave front sensor is currently the industry standard in adaptive optics. It utilizes a simple lenslet array to identify how the wave front is distorted. Knowing that a plane wave front should create a perfectly focused image at the center of each lenslet array, it is easy to reconstruct how a wave has been distorted by analyzing how the image in each cell has been shifted. By increasing the number of lenslets in the array, higher order measurements can be made. However, that also decreases the amount of light per cell and the SHWFS cannot detect aberrations in the absence of light. [2] While adaptive optics using the SHWFS have proven incredibly successful, there is a technological limit to the device that is well below the theoretical diffraction limit that could be achieved with better instrumentation.

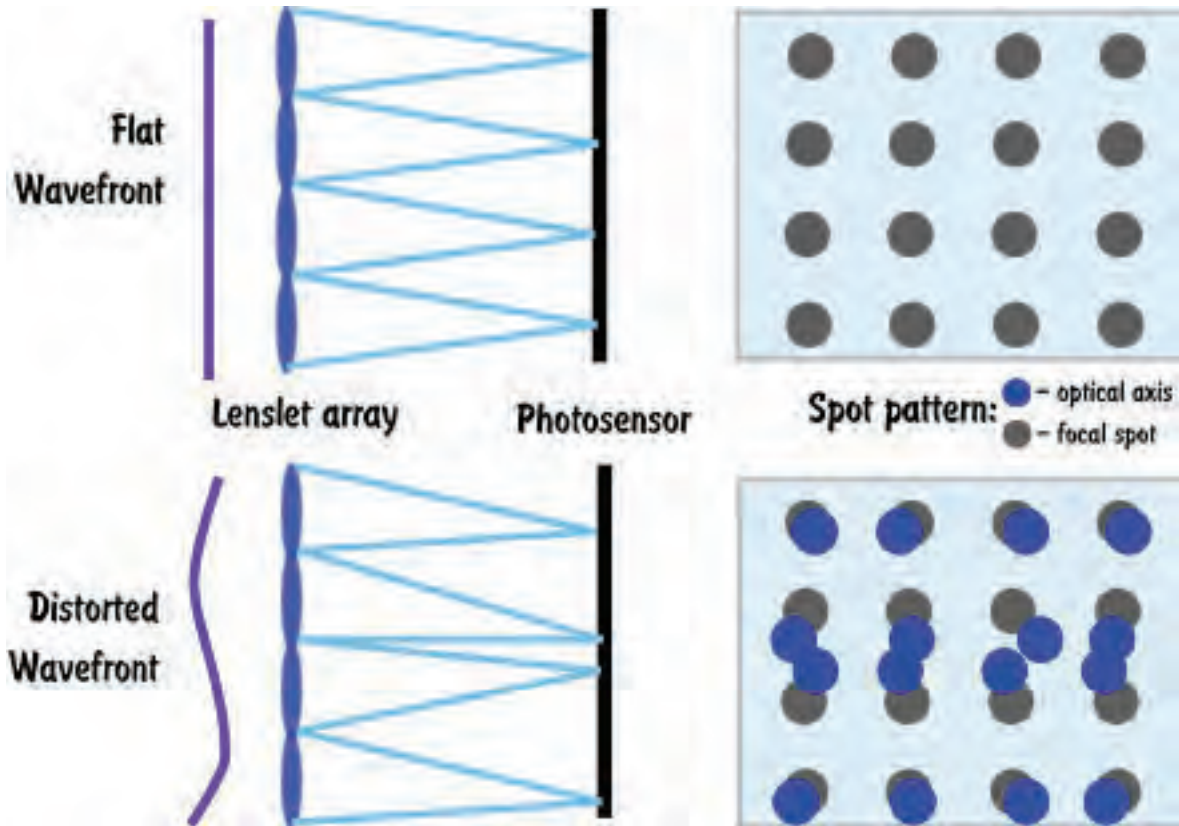


Figure 2: The Shack-Hartmann Wave Front Sensor uses a lenslet array to detect how a wavefront is distorted from what a flat wave front should look like.

The New Wave Front Sensor

The non-linear Curvature Wave Front Sensor (nlCWFS) or Fresnel WFS is capable of improved resolution over the SHWFS. It utilizes four defocused images on either side of the pupil to reconstruct an image at the pupil plane. Figure 3 shows the basic idea behind a conventional Curvature Wave Front Sensor, which utilizes the same physics but only two planes. By comparing phase information between defocused planes on either side of a pupil it is possible to reconstruct an image at the pupil plane. Utilizing four planes instead of two greatly enhances the sensitivity of the wave front sensor. [1] In order to reconstruct the

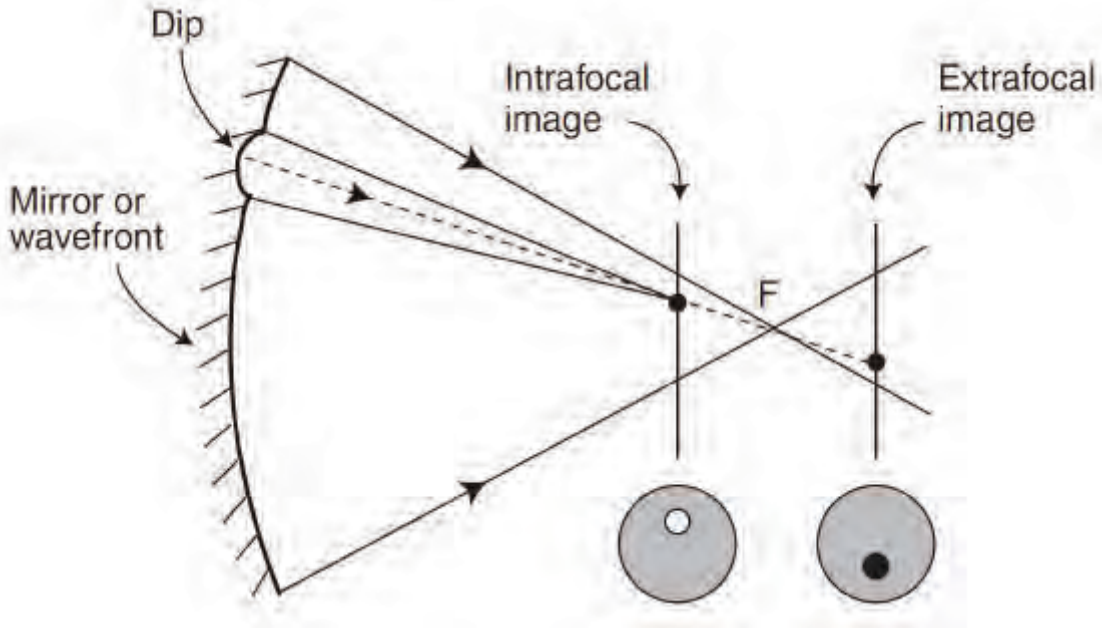


Figure 3: non-linear Curvature Sensors use defocused planes on either side of the pupil to compare the relative curvature in the wave front and reconstruct an image at the pupil plane between them. [2]

image at the pupil plane, the Fresnel diffraction integral must be used: [4]

$$U(x_2, y_2) = \frac{e^{ik\Delta z}}{i\lambda\Delta z} \int_{-\infty}^{\infty} \int_{-\infty}^{\infty} U(x_1, y_1) e^{i\frac{k}{2\Delta z} [(x_1-x_2)^2 + (y_1-y_2)^2]} dx_1 dy_1. \quad (1)$$

This integral must be solved numerically through an iterative process using Fourier Transforms. The solution method has been easily doable for some time, however only recently have advances in computing power made it possible to converge on a solution and reconstruct a wave front in real time.

Conclusion

This project is still ongoing and will culminate with the successful completion of a self-contained nCWFS optical system for use at a major telescope. It will replace the Shack-Hartmann wave front sensor as the industry standard and provide superior resolution by at least a factor of ten. This will allow ground based telescopes to obtain images much closer to the theoretical diffraction limit than is currently possible.

Current progress is proceeding apace with many milestones met and many more feasible on the horizon. Using Object Oriented Matlab Adaptive Optics (OOMAO) the team has demonstrated the theoretical capability for the new wave front sensor. A real time computer (RTC) has been built with a wave front error budget within acceptable processing time using simulated data. The instrumentation has been setup and aligned to provide real data using both the SHWFS and the nCWFS. Artificial aberrators have been constructed and put in place to demonstrate the resolving power of the system. More work needs to be done to the RTC system to improve its performance and ensure proper treatment of any wave front distortion. Once a reasonable comparison between the SHWFS and the nCWFS can be made using real data, proof of concept will help draw the necessary funds to upgrade the equipment to improve all aspects of the design and increase resolution and processing speed.

References

- [1] Guyon, O. (2009). High sensitivity wavefront sensing with a nonlinear curvature wavefront sensor. *Publications of the Astronomical Society of the Pacific*, 122(887), 49.
- [2] Crass, J. (2014). *The Adaptive Optics Lucky Imager: combining adaptive optics and lucky imaging* (Doctoral dissertation, University of Cambridge).
- [3] Mateen, M. (2015). *Development and verification of the non-linear curvature wavefront sensor*.
- [4] Schmidt, J. D. (2010, July). *Numerical simulation of optical wave propagation with examples in MATLAB*. Bellingham, Washington, USA: SPIE.

Study of Stub Momentum Resolution and Hardware Benchmarking for CMS Track Trigger

Author: Tianyi Wang

2019 NSF REU Program

Physics Department, University of Notre Dame

July 22, 2019

Advisors: Kevin Lannon, Michael Hildreth

Abstract

As the High-Luminosity Large Hadron Collider (HL-LHC) project upgrades the Large Hadron Collider (LHC) to greater collision density, a new technique applied to the L1 trigger called Track Trigger increases its ability to reject uninteresting collisions by providing more track information [1]. It quickly reconstructs tracks through a bend predicting algorithm, which includes many geometric corrections to compensate for deviations caused by simplified calculation. This research focuses on testing the resolution of bend predicting algorithm to give bend estimations based on given track information. Its resolution is key to determine whether the geometric corrections being applied are accurate enough for use. Benchmarking is also conducted on different options for system on chips (SOC), which are important for controlling the system during data collection.

Background

The project is concerned about the innermost section of sensors in the Compact Muon Solenoid (CMS) called the silicon tracker as shown in Figure 1. Each module in the tracker consists of strips or matrices of individual sensors. When particles emitted from collisions come through the tracker, they interact with the sensors to generate signals called hits. Figure 2 shows a r-z cross section of silicon trackers, where the whole section is divided into barrel, tilted barrel, and endcap region according to orientation of the modules. The inset shows the expanded detail of a module on the x-y plane. It consists of two parallel layers of sensors a few

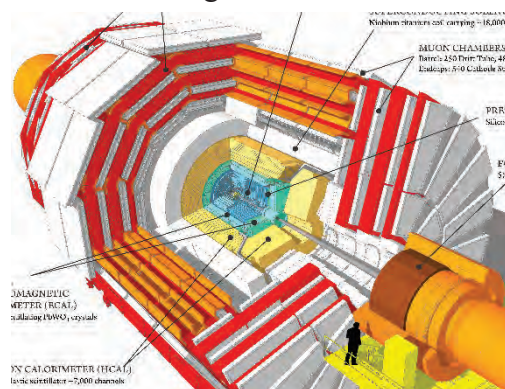


Figure 1: Structure of CMS, the blue section in the center is the silicon trackers

millimeters away from each other, where two hits from a particle constructs a stub. Another quantity named bend is introduced to describe the amount of horizontal shift in a stub [2].

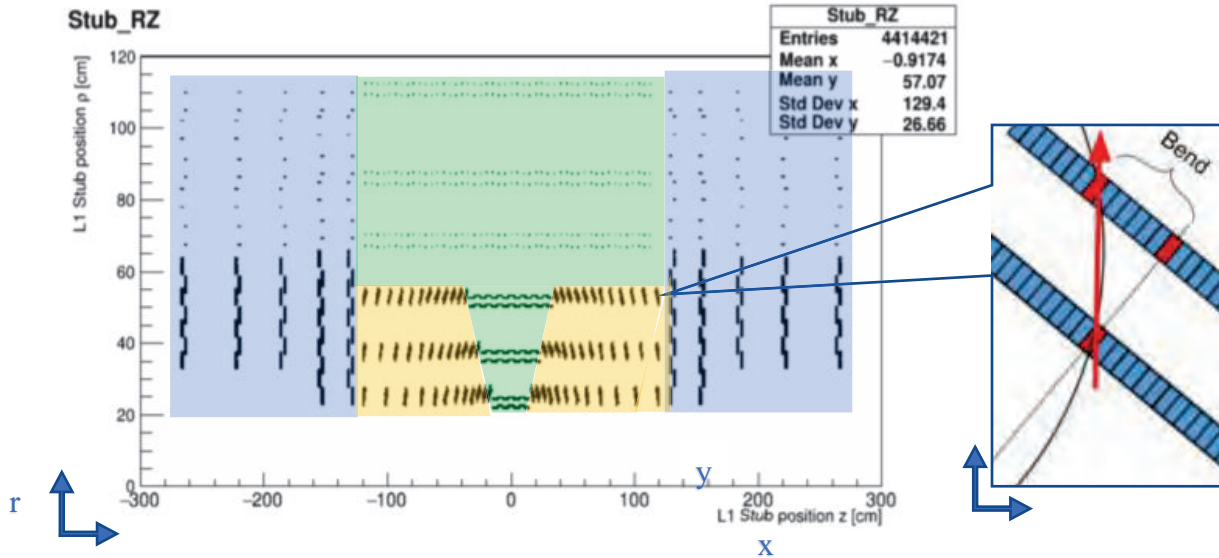


Figure 2: Cross section of silicon trackers, with barrel colored green, tilted barrel colored yellow, and endcap colored blue. On the right it shows the detail of a pair of stubs and an example of bend

With the assumption that the collision comes from the original point (0, 0) in the x-y coordinate, the bend can be calculated from the position of stub and the transverse momentum of particle creating the track. The analytic formula for bend prediction includes extensive trigonometric and angular components that the FPGA are inefficient to calculate and lead to large uncertainty in many situations involving small angles. Previous researchers have proposed a simplified formula with correction factor to calculate the bend:

$$bend = \frac{-r \cdot dr \cdot B \cdot c}{pitch \cdot p_T \cdot correction \cdot 2 \cdot 10^{11}} \quad [4]$$

- For the tilted barrel: correction = 0.886454*(|stub_zl/stub_r) + 0.504148
- For the ECs: correction = (|stub_zl/stub_r)
- For the barrel: correction = 1

Where *pitch* is the width of an individual strip of sensor, *dr* is the spacing between layers in a stub,

and p_T is the transverse momentum. The factor $2 \cdot 10^{11}$ at the denominator is to compensate for unit conversions. Inserting numerical values for the constants, the formula becomes:

$$bend = \frac{-0.5 \cdot dr \cdot r \cdot r_{inv}}{pitch \cdot correction}$$

Where r_{inv} is the inverse of the particle trajectory's radius. This value is inversely proportional to the momentum of the particle as it travels in a magnetic field. The correction factor [4] is applied to account for the error cause by direction difference of tilted barrel and endcap. It is an approximation to the full geometrical correction for the module tilts and has been shown to be totally adequate for the purposes of the algorithm.

The Track Trigger is developed to reconstruct trajectories of charged particles by linking together stubs. To reject fake combinations of stubs caused by different particles, it requires the momentum of the stub to comply with the momentum of the track that it's being used to reconstruct. The stub momentum is calculated from the measured bend of the stub, while track momentum is measured from the radius of curvature of the particle trajectory in the magnetic field created by CMS. Given momentum of the track and position of the stub, its stub bend can be calculated by bend predicting algorithm. Then the bend consistency cut algorithm checks whether the measured bend matches this predicted bend, and thus decide whether the stub belongs to the track. However, the measured bend of the stub would always deviate a little from the predicted one due to two major reasons. First, the accuracy of measured stub bends is about 0.4 to 0.5 strip width due to limited sensor precision [5]. Second, the algorithm that predicts stub bends from p_T relies on information that aren't known perfectly in real experiment. The primary goal of this research is to test the stub momentum resolution of the bend prediction algorithm, which determines if the

geometric corrections applied to the bend prediction algorithm are accurate enough for use.

The track reconstruction algorithm will be implemented into FPGA firmware, which are processors simpler than CPUs but specializing in performing certain command at very high frequency. There will also be processors configuring and controlling the FPGAs serving as part of the track trigger control system. In addition to studying bend resolution, I also worked on competent processor options to see whether they are suitable for the track trigger control system.

Method

The research utilizes a simulation of the upgraded CMS detector [6]. It is used to simulate two classes of collision: One in which a pair of muons with same momentum and opposite charge and direction is produced with randomly selected transverse momentum between 2 and 100 GeV. The other resembles real LHC collisions in which a top quark pair is produced, but with additional 200 additional overlapping collisions to represent the situation after the HL-LHC upgrade.

The bend prediction algorithm takes the value of stub coordinate (r, z) and the true value of the transverse momentum for the particle the produced the stub in the simulation . In this way, its prediction results are free of measurement errors and only contain deviations from the approximated geometric correction factors. Then the program reads in measured bends generated by simulator for the same stub, which have been processed to simulate data output from actual LHC runs. Measured bends are therefore disturbed by device uncertainty. They in a stored accuracy slightly less than 0.5 pitch, or half the width of an individual sensor due to limited sensor precision and storage assigned to each stub bend (4 bits for outer barrel and 3 bits for other regions).

The performance of bend prediction algorithm is measured by two ways. First is the range of deviation distribution. The second is sign of systematic biases, especially if deviation between predicted and measured bend is not random and evenly distributed, but instead suggesting an inclination to underestimate or overestimate the bend or performing much worse in certain regions.

The hardware benchmarking project consists of three different benchmarks: sbc bench, Zeromq performance tests, and CoreMark. The sbc bench [7] tests the processors' capability to compress and decompress files via 7-zip and conduct AES encryptions with different sizes of data being encrypted. The Zeromq performance test [8] transmits and receives data via local Ethernet to test the network and interthread latency of processors. CoreMark [9] tests their capability of solving simple functions, as well as assigning value for arrays of empty memory space.

Results

The most general and representative indicator of how well the bend prediction algorithm functions is statistics of deviation between predicted and measured bend. Because error assigned to measured bends are random, the deviation distribution should be a Gaussian curve. The smallest possible width of the Gaussian curve would be at around 0.4 based on the intrinsic bend measurement precision and would be larger if other sources of error exist.

Figure 3 contains distribution of deviation between predicted and measured bends for 100 top pair production events with 0.5 bend as single bin width. The bend prediction curve has a mean value at 0.0026 ± 0.0015 bend and sigma of 0.533 ± 0.001 . With average value very close to 0 and sigma close to theoretical limit of 0.4, it shows that there's no significant, systematic flaw in

the bend predicting algorithm and there's no visible error in detecting charge of particles. In distribution of bend deviation for 10000 muon pair events, the fitted Gaussian curve has a mean value at $5.316 \cdot 10^{-5}$ bend and sigma at 0.492 ± 0.001 . The Gaussian width in top pair production events is bigger than in muons because it includes stubs from many other types of particles, including electrons which lose a lot of energy moving through the detector and pions which have a similar mass to muons but also experience nuclear interactions. These particles experience significant impact when they pass through the detectors, and thus have a worse p_T resolution in prediction

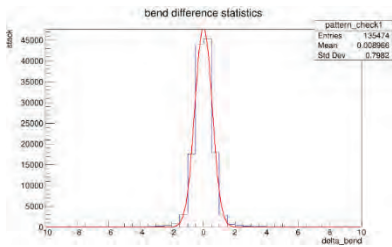


Figure 3: bend deviation statistic for top pair production events with Gaussian curve fitting

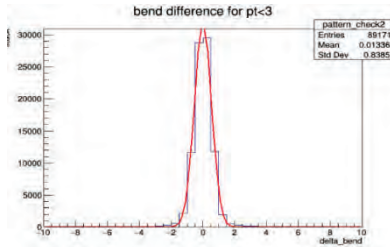


Figure 4: bend deviation for p_T smaller than 3 GeV in top pair production events (0.5 step)

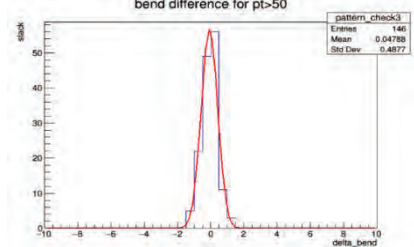


Figure 5: bend deviation for p_T larger than 50 GeV in top pair production events (0.5 step)

Pt (GeV)	2-3	3-10	10-20	20-30	30-40	40-50	50+	General
Muon	0.499	0.491	0.478	0.482	0.472	0.486	0.501	0.493
Top pair	0.538	0.526	0.490	0.460	0.491	0.496	0.499	0.533

Table 1: sigma value (width) of Gaussian curve for different p_T in muon and top pair production events

Table 1 shows that the width of Gaussian curve is largest when p_T is less than 3 GeV and larger than 50 GeV, while being smallest in between. The larger Gaussian curve width at smaller p_T is at least partially contributed by the excessively large number of entries that fall under this region, so the p_T resolution in general drops as its value rises at a minimal rate. No other tendency

or bias is observed relating to energy level, as shown in Figure 4 and 5.

Region	Inner barrel	Outer barrel	Tilted barrel	Endcaps
Muon	0.494	0.419	0.516	0.509
Top pair	0.527	0.507	0.539	0.544

Table 2: sigma value (width) of Gaussian curve for different region in muon and top pair production events

Table 2 shows that in both muon and top pair production events the bend prediction algorithm is most accurate in outer barrel region, while being less accurate in inner barrel region and deviate the most in tilted barrel and endcaps. In general, the Gaussian curve width is smaller than 0.55 in all cases. This implies that the geometric corrections compensate for most of the deviations caused by stub position difference and avoid major systematic errors. However, its resolution in the tilted modules and the endcap is worse than ideal. This is not completely unexpected especially for stubs in tilted barrel region because the geometric corrections don't take specific angle of individual stubs into account. However, these regions should be studied more carefully in the future to see if additional corrections can improve the resolution.

In hardware benchmark, comparisons were drawn between COM Express, a competent SoC for

local latency	raspi					raspi 3 b+							
latency/ms	100	1000	10000	100000	1000000	exe time/ite	100	1000	10000	100000	1000000		
100Byte	/	69.19	77.9	81.77	82.08		100byte	-0.3	-0.4		1.9	16.7	
1K	/	71.58	80.85	83.57	83.69		1K	-0.4	-0.4	-1.9		16.9	
10K	112.74	125.48	139.16	140.01	139.89		10K	-0.2	-0.2	-0.5		3	28.2
100K	330.79				/		100K	-0.3				/	
1M				/	/		1M				/	/	
local latency	COM Express					COM Express							
latency/ms	100	1000	10000	100000		exe time/ite	100	1000	10000	100000			
100Byte	536.58	932.02	762.17	625.63			100Byte	1.148	2.902	16.288	126.165		
1K	518.62	907.84	837.48	575.48			1K	1.144	2.856	16.574	116.136		
10K	795.17(unstable)	768.76	746.5	600.78			10K	1.199	2.576	15.969	121.193		
100K	597.32	857.48	642.24	569.53			100K	1.16	2.754	13.885	114.946		
1M	1755.77	1633.7	1522	1602.87			1M	1.391	4.308	31.479	321.615		

Table 3: Latency and execution time of Zeromq local latency test for COM Express and raspi3 b+

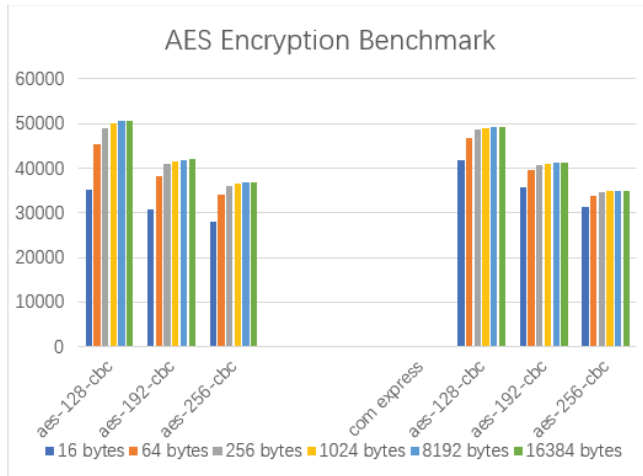


Figure 6: AES encryption test results of Raspi 3b+ and COM Express

Track Trigger equipped with a quad-core Intel Celeron J1900 processor and Raspi 3b+, a popular SoC model in the market with a quad-core Broadcom Cortex A53 processor. The encryption test from sbc bench shows that while they provide similar processing power

in dealing with larger data chunks, the efficiency of Raspi 3b+ drops significantly when processing small chunks of data, especially in the 16 bytes category as shown in Figure 6. This might be due to the lower clock speed of its processor, which is at 1.4GHz compared to 2.42GHz in COM Express. In average of 10 successive runs of Zeromq local latency test via bash script, COM Express shows a much larger and unstable latency compared to Raspi 3b+. This might be caused by its lack of hardware network control component or because it is booted on an older version kernel. Its detail awaits for further investigation in the future.

Further Studies

The next step for the simulation project is to figure out whether and how much influence to deviation is caused by resolution of p_T measurement, binning of results, or insufficiencies in the geometric correction respectively. This would be helpful in finding out whether the width of the bend deviation curve could be cut down further, and thus increase the resolution of the bend prediction algorithm. Special attention will be given in exploring the necessity and influence of additional geometric corrections applied on the tilted modules and the endcaps to improve the

algorithm's performance in these regions.

For benchmarking project, the Zynq will be built and configured with the same environment as COM Express. Comparisons will be then made according to their hardware parameters and performance in benchmarks. The goal is to measure their comparative strength in performing various types of tasks and help determine which one is a better choice for the Track Trigger.

Reference

- [1] The HL-LHC Project | High Luminosity Large Hadron Collider. CERN. <http://hilumilhc.web.cern.ch/>
- [2] Detector | CMS Experiment. CERN. <https://cms.cern/detector>
- [3] CERN, High-Luminosity Large Hadron Collider (HL-LHC) Technical Design Report V. 0.1., <http://dx.doi.org/10.23731/CYRM-2017-004>
- [4] Bend prediction formula and Correction Factors developed by Emyr Clement (Private communication)
- [5] Kevin Greif, "Bend Consistency Cut Performance in the CMS Detector L1-Trigger Upgrade", 2018
- [6] L1TrackNtupleMaker, program from CMSSW10_1_4 software environment
- [7] Thomas Kaiser, sbc-bench, <https://github.com/ThomasKaiser/sbc-bench>
- [8] Zeromq Performance Tests, 2011, <http://zeromq.org/area:results>
- [9] Embedded Microprocessor Benchmark Consortium (EEMBC), CoreMark®, <https://github.com/eembc/coremark>

The Effect of Finite Organism Size and Contact Forces in Population Dynamics

Hiroka Warren

2019 REU/NSF Program
Physics Department, University of Notre Dame

Adviser: Professor Dervis Can Vural

Abstract

We study the Lotka-Volterra model with intraspecific competition. The Lotka-Volterra equation describes the population dynamics of interactions between predators and preys. The intensity of the interactions depends on the size of species as well as area density. We show numerically and analytically that properties of this model changes depending on the size of species.

Introduction

The Lotka-Volterra equations (also known as predator-prey equations) give the population model of interactions between predators and preys. In the Lotka-Volterra model with two species, the predators feed on the preys [1], which in turn feed on some natural resource. There are several assumptions in this model. One of the assumptions is that the prey population always has an unlimited food supply. In other words, this model is applied only in some ideal conditions [2]. Multi-species Lotka-Volterra models have been studied by many researchers. However, not much known for the competitive model statistically. A research shows that the position of species can affect the intensity of competitive interactions. Typically, species can experience a stronger competition in areas of high density. As a result, a species can only survive if it can maintain some distance with the other species [3].

The aim of this research is to include finite size effects to the Lotka-Volterra model with intraspecific competition by using a simulation. We also show how to correct the mean-field model when size of the species is included.

Methods

Simulation Methods

We built a simulation which contains two species: namely, green balls (as prey) and red balls (as predator). Here is the scenario.

1. If a green ball hits another green ball, one of them disappears (because they compete for the same resources) with probability $P1$. With probability $1 - P1$, nothing happens.
2. If a green ball hits a red ball, the green ball turns a red ball (because the predator ate the prey and reproduced another predator) with probability $P2$. With probability $1 - P2$, nothing happens.
3. If no one collides or nothing happened in the scenario 1 and 2, a green ball reproduces another green ball with probability $P3$. With probability $1 - P3$, nothing happens.
4. A red ball dies with probability $P4$. With probability $1 - P4$, nothing happens.
5. The both green balls and red balls have finite size and perform a random walk in 2D.

Green balls have a step size of g , and red balls have a step size of r .

The simulation was compared with the theoretical model. The interaction matrix of the system in the simulation is

$$\begin{array}{cc} & \begin{array}{cc} G & R \end{array} \\ \begin{array}{c} G \\ R \end{array} & \begin{bmatrix} -P1 & -P2 \\ P2 & 0 \end{bmatrix} \end{array} \quad (1)$$

From this matrix, we obtain the Lotka-Volterra equations for the simulation.

$$\dot{G} \sim G [P3 - P1G - P2R] \quad (2 - a)$$

$$\dot{R} \sim R [-P4 + P2G] \quad (2 - b)$$

At steady state,

$$\dot{G} = 0 = P3 - P1G^* - P2R^* \quad (3 - a)$$

$$\dot{R} = 0 = -P4 + P2G^* \quad (3 - b)$$

From equation (3 – a) and (3 – b), we obtain population ratio of green balls and red balls.

$$\frac{G^*}{R^*} = \frac{P2P4}{P2P3 - P1P4} \quad (4)$$

We varied the radius $R = (0.1, 0.3, 0.5, 1.0, 1.5, 2.0)$, of each ball across multiple simulations making all balls the same radius. Since the results varied depending on the size of balls, we assumed that there must be other probabilities that we should include in the equation. In order to include “size” in the equation, we assume a modified set of equations

$$\dot{G} \sim G [P3 - P1\rho_{hit}^{GG}G - P2\rho_{hit}^{GR}R] \quad (5 - a)$$

$$\dot{R} \sim R[-P4 + P2\rho_{hit}^{GR}G] \quad (5 - b)$$

where ρ_{hit}^{GG} is the probability that a green ball hits another green ball, and ρ_{hit}^{GR} is the probability that a green ball hits a red ball. At steady state, we get population ratio of green balls and red balls from the equation (5 – a) and (5 – b).

$$\frac{G^*}{R^*} = \frac{P2P4\rho_{hit}^{GR}}{P2P3\rho_{hit}^{GR} - P1P4\rho_{hit}^{GG}} \quad (6)$$

In order to calculate ρ_{hit}^{GG} and ρ_{hit}^{GR} , we made simulations for each size of balls with each population ratio and area density by using the numerical steady-state results in the simulation. When a green ball hits a red ball and turns into a red ball, the probability of this event is $P(P2 \cap \rho_{hit}^{GR}) = P2\rho_{hit}^{GR}$. $P2\rho_{hit}^{GR}$ can be measured in the simulation by setting other probabilities $P1 = P3 = P4 = 0$ and counting how many green balls survived after one simulation time-step (tick).

$$P2\rho_{hit}^{GR} = 1 - \frac{\text{number of ball after one tick}}{\text{initial number of ball}} \quad (7)$$

We set $P2 = 1$ to simplify the calculation to obtain ρ_{hit}^{GR} . ρ_{hit}^{GG} can be obtained with the same procedure as ρ_{hit}^{GR} . However, since it was difficult to measure ρ_{hit}^{GG} unlike ρ_{hit}^{GR} (Figure 1), we calculated ρ_{hit}^{GG} by setting equation (6) equals to numerical number of population ratio.

$$\rho_{hit}^{GG} = \frac{(\text{numerical}_{\frac{G}{R}})P2P3\rho_{hit}^{GR} - P2P4\rho_{hit}^{GR}}{(\text{numerical}_{\frac{G}{R}})P1P4} \quad (8)$$

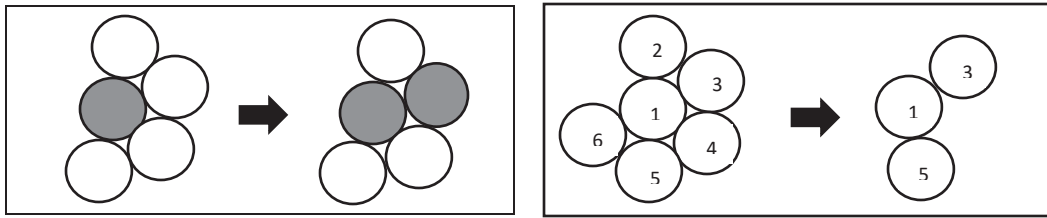


Figure 1: a) When a red ball hits multiple green balls at the same time, only one of them becomes a red ball. b) When a green ball hits multiple other green balls at the same time, multiple green balls can disappear at a time (Green 1 kills Green 2, Green 3 kills Green 4, and Green 5 kills Green 6.).

Calculation Methods

In order to get the same population ratio of green balls and red balls as the numerical result, we modify the population ratio as

$$f(\bar{\varepsilon}) = \frac{(P2 + \varepsilon_2)(P4 + \varepsilon_4)}{(P2 + \varepsilon_2)(P3 + \varepsilon_3) - (P1 + \varepsilon_1)(P4 + \varepsilon_4)} \quad (9)$$

We want to find $\bar{\varepsilon}$ such that $|\bar{\varepsilon}|$ is minimum. Therefore, we define Lagrangian,

$$L = (n - f(\varepsilon))^2 + \sum_i \varepsilon_i^2 \quad (10)$$

where n is the numerical number of population ratio. Minimizing the Lagrangian attempts to get a better prediction of the ratio while also regularizing the amount of change we introduce into the model. L can be minimized by taking derivative of equation (10) and set it to 0.

$$\frac{\partial L}{\partial \varepsilon_1} = 0 = 2(n - f(\varepsilon)) \frac{\partial f}{\partial \varepsilon_1} + 2\varepsilon_1 \quad (11 - a)$$

$$\frac{\partial L}{\partial \varepsilon_2} = 0 = 2(n - f(\varepsilon)) \frac{\partial f}{\partial \varepsilon_2} + 2\varepsilon_2 \quad (11 - b)$$

$$\frac{\partial L}{\partial \varepsilon_3} = 0 = 2(n - f(\varepsilon)) \frac{\partial f}{\partial \varepsilon_3} + 2\varepsilon_3 \quad (11 - c)$$

$$\frac{\partial L}{\partial \varepsilon_4} = 0 = 2(n - f(\varepsilon)) \frac{\partial f}{\partial \varepsilon_4} + 2\varepsilon_4 \quad (11 - d)$$

We assume the corrections are small in comparison to the initial probability values ($\frac{\varepsilon_1}{P_1} \ll 1, \frac{\varepsilon_2}{P_2} \ll 1, \frac{\varepsilon_3}{P_3} \ll 1, \frac{\varepsilon_4}{P_4} \ll 1$). The resulting system of the equation can be linearized around $0 \approx \bar{a} + B\bar{\varepsilon}$.

Therefore, we can approximate the optimal solution by solving the linear set of equations to get

$$\bar{\varepsilon} \approx -\bar{B}^{-1}\bar{a}. \quad (12)$$

Results

Simulation results

Figure 2 shows the difference between the theory and the numerical results in the simulation, where radius $R = 0.5$, $P_1 = 0.5$, $P_2 = 0.3$, $P_3 = 0.3$, $P_4 = 0.1$, step-size $g = r = 1$, and the initial

number of both balls = 20. While the

theory suggests that $\frac{G^*}{R^*} = 0.75$, the result

in the simulation is $\langle \frac{G}{R} \rangle = 0.749$, which

results in $error = \left| \frac{\langle \frac{G}{R} \rangle - \frac{G^*}{R^*}}{\frac{G^*}{R^*}} \right| = 0.011$.

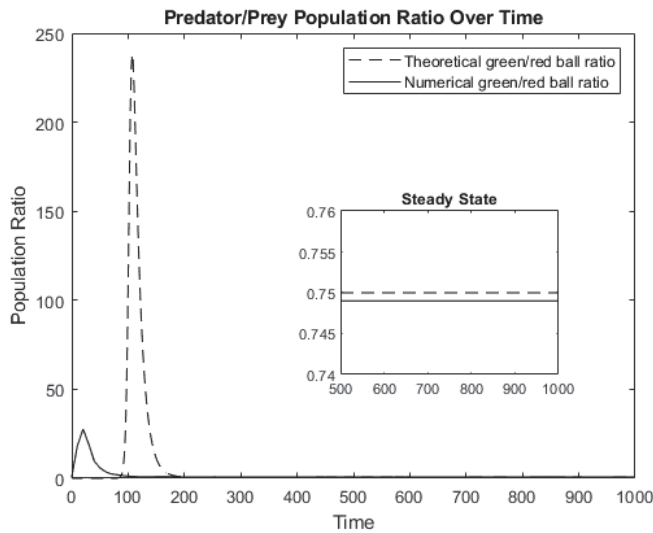


Figure 2: Theoretical and numerical population ratio of green balls and red balls.

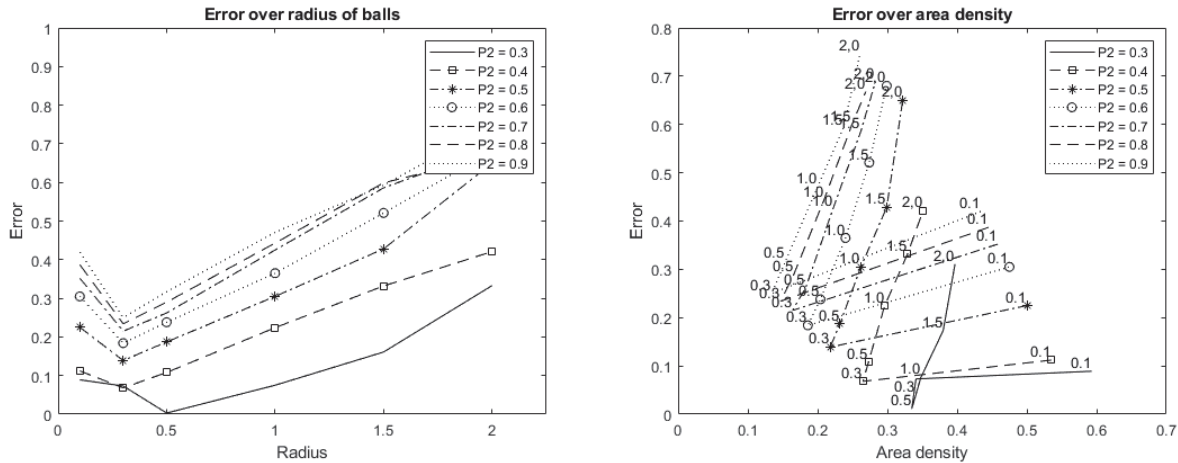


Figure 3: a) Error over radius of balls with different probability P2. b) Error over area density with different probability P2.

Figure 3 (a) shows a relation between error and the size of balls with the same step-size, initial number of balls, and probabilities with different P2. Figure 3 (b) shows a relation between error and $area\ density = \frac{total\ number\ of\ balls}{total\ area\ in\ the\ space}$. We expected that as we increase the radius of ball, error would be larger, and as we decrease the radius, error would be even smaller. However, the simulation for P2 = 0.3 shows larger error for smaller radius than R = 0.5 while error for larger radius becomes larger as we expected. Figure 3 (b) tells us the large error for the smaller size of balls is related to area density. Because there are more balls when the size of balls is very small, its area density becomes higher (Figure 4). The interesting fact in the graphs is that

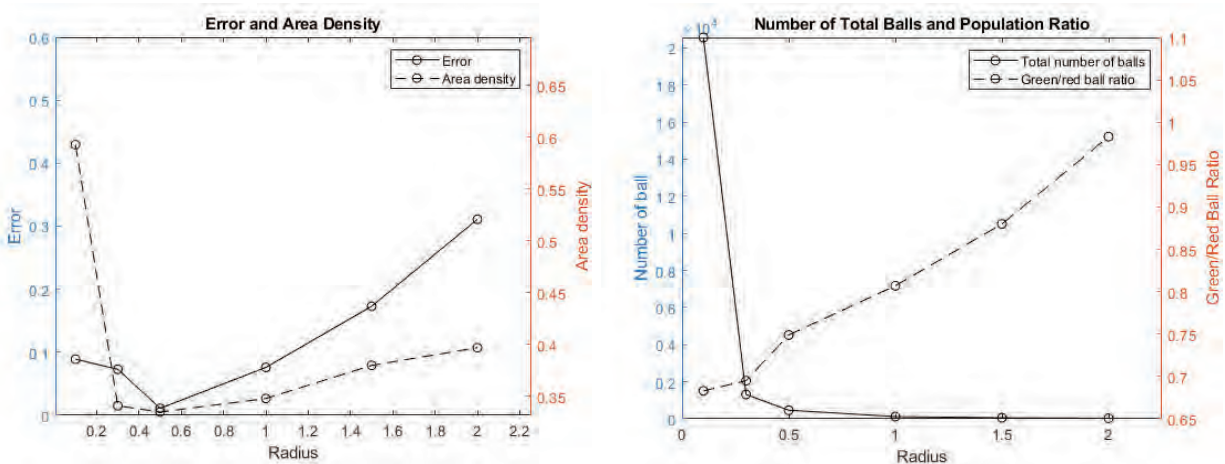


Figure 4: a) Error and area density. b) Number of total balls and population ratio of green balls and red balls.

the size is not the only factor that affects the results in error. The minimum error for $P_2 = 0.3$ is $R = 0.5$ while for other P_2 probabilities, $R = 0.3$ results in the smallest error. It implies that not only the size of balls but also probability combinations can affect total number of species in the space.

Figure 5 shows a relation between error and area density with the same step-size, initial number of balls, and probabilities with different P_1 (a), P_2 (b), P_3 (c), and P_4 (d). Not every probability is included in the graphs because with some probability combinations we got negative theoretical number, or in the simulation either green balls or red balls did not survive.

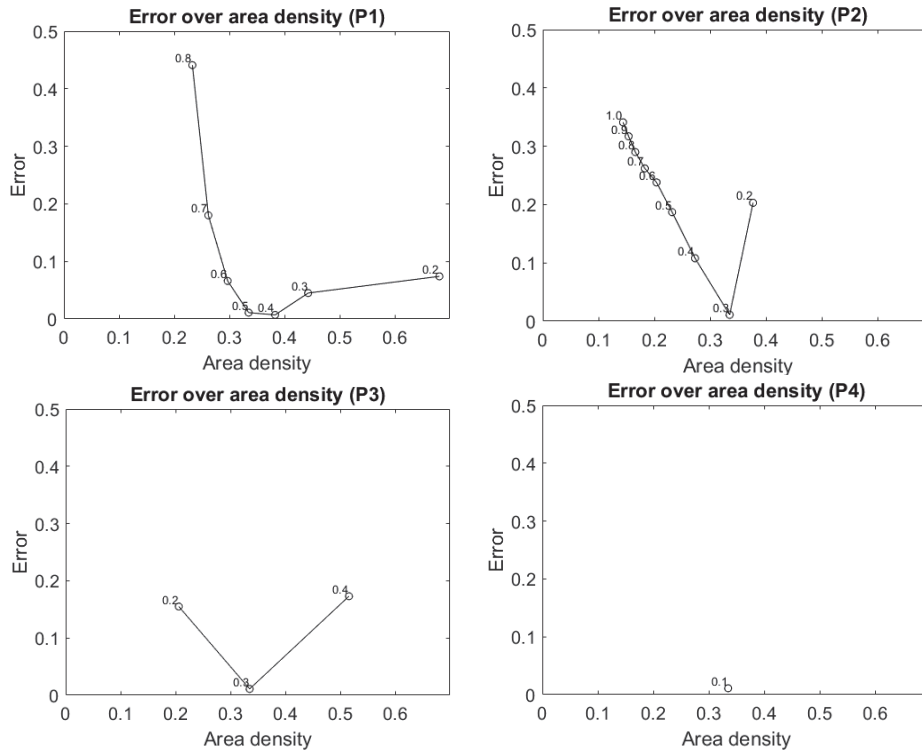


Figure 5: Error over area density for a) different P_1 with $P_2 = P_3 = 0.3$ and $P_4 = 0.1$, b) different P_2 with $P_1 = 0.5$, $P_3 = 0.3$, and $P_4 = 0.1$, c) different P_3 with $P_1 = 0.5$, $P_2 = 0.3$, $P_4 = 0.1$, and d) different P_4 with $P_1 = 0.5$, $P_2 = P_3 = 0.3$.

Figure 6 shows the result of ρ_{hit}^{GR} and ρ_{hit}^{GG} , where $P_1 = 0.5$, $P_2 = 0.3$, $P_3 = 0.3$, $P_4 = 0.1$, step-size $g = r = 1$, and the initial number of both balls = 20. Since the minimum error as well as area density in the situation is $R = 0.5$ as shown in Figure 3, we can expect at larger and smaller radius than $R = 0.5$, there would be more interactions among species because of high area density. This

explains the higher ρ_{hit}^{GR} and ρ_{hit}^{GG} for larger and smaller radius in Figure 6. The interesting result in the graph is that ρ_{hit}^{GR} is larger than ρ_{hit}^{GG} for $R = 0.3$ and 0.1 , and ρ_{hit}^{GR} is smaller than ρ_{hit}^{GG} for $R = 1.0, 1.5,$ and 2.0 . This can be explained by population ratio of green balls and red balls as shown in Figure 4 (b). With $R = 2.0$, population ratio is almost 1, which means the number of green and red balls are the same. If there are the same number of green and red balls, we may expect that there would be more interactions between green and red balls rather than interactions among only green balls. However, the simulation also shows that while a red ball kills one green ball at a time even when it hits multiple green balls at the same time, multiple green balls can disappear at a time when a green ball hits multiple other green balls at the same time (Figure 1). Therefore, it is possible that there are more interactions among green balls, but ρ_{hit}^{GR} and ρ_{hit}^{GG} relation varies

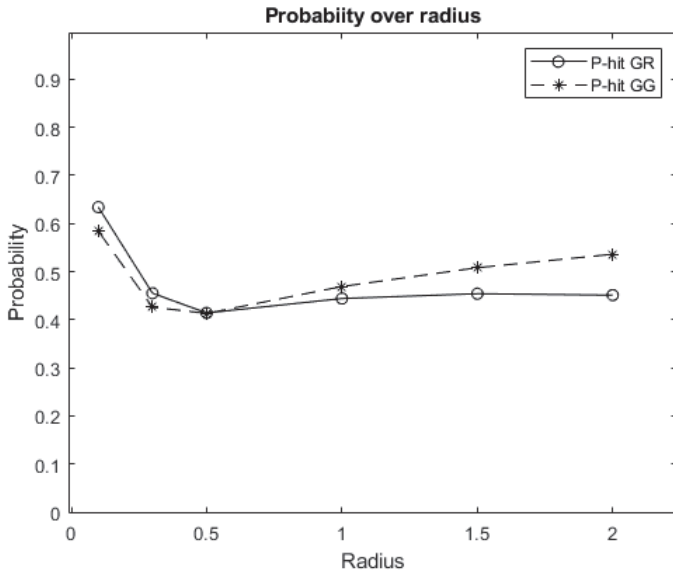


Figure 6: Probability ρ_{hit}^{GR} and ρ_{hit}^{GG} over radius of balls.

depending on the population ratio.

We must note that these probabilities can be applied only with the specific area density and population ratio of green and red balls for each radius of balls.

Calculation results

We solved the problem for a simulation, where radius $R = 0.5$, $P1 = 0.5$, $P2 = 0.9$, $P3 = 0.3$, $P4 = 0.1$ ($\frac{G^*}{R^*} = 0.4091$, $\langle \frac{G}{R} \rangle = n = 0.538605095$, and $error = \left| \frac{\langle \frac{G}{R} \rangle - \frac{G^*}{R^*}}{\frac{G^*}{R^*}} \right| = 0.317$). By solving the matrix, we got

$$\begin{bmatrix} \varepsilon_1 \\ \varepsilon_2 \\ \varepsilon_3 \\ \varepsilon_4 \end{bmatrix} = \begin{bmatrix} -0.015272093322937113 \\ 0.009692056367354583 \\ 0.04861521365238594 \\ 0.04200580067444445 \end{bmatrix}$$

Therefore,

$$f(\varepsilon) = 0.5202675187859286$$

$$error = \left| \frac{f(\varepsilon) - n}{n} \right| = 0.03404642173700825.$$

Conclusion

The simulation shows that the Lotka-Volterra model is no longer accurate when the size of species is considered. Area density and probability combinations also affect error for the equations. One of possible reasons is that when area density is high, the probability of interacting with other balls becomes higher than when the density is low. It leads more interactions among species than the Lotka-Volterra model expects.

References

- [1] J. Hofbauer and K. Sigmund, “The Theory of Evolution and Dynamical Systems,” second edition (Cambridge University Press, New York, 1988), pp.40-58.
- [2] M. C. Anisiu, “Lotka, Volterra and their Model,” *Didactica Mathematica* , Vol. 32, 2014, pp. 9–17.
- [3] S. Pigolotti, C. L’opez, and E. H. Garc’ia, “Species clustering in competitive Lotka-Volterra models,” DOI:10.1103/PhysRevLett.98.258101.

Implanted ^{14}N Target Preparation and Evaluation

Lexanne Weghorn

2019 NSF/REU Program

Physics Department, University of Notre Dame

Advisors: Dr. Ani Aprahamian and Dr. Wanpeng Tan

Abstract

The $^{14}\text{N}(p,\gamma)^{15}\text{O}$ reaction is one of the time-limiting reactions in stellar evolution and the burning of protons to heavier elements known as the CNO cycle. This rate is in turn dependent on the lifetime of the 6.79 MeV state in ^{15}O . Previous measurements have been made of the lifetime of this state, but with discrepant results. In preparation for a lifetime measurement of the 6.79 MeV state in ^{15}O , targets were produced by implanting different doses of ^{14}N into tantalum, tungsten, and molybdenum backings at beam energies of 350 keV. The characteristics of the targets were determined using the 1.06 MeV resonance in $^{14}\text{N}(p,\gamma)^{15}\text{O}$. Methods and measured target profiles will be reported, and plans for the lifetime measurement will be discussed.

Introduction

Although stellar processes cannot be examined in experimental conditions, it is possible to imitate the conditions inside stars through nuclear physics. The CNO cycle in stars, where hydrogen is converted to helium through a series of reactions, is one such process for which there is a high demand for clarity. The slowest reaction in this process is the $^{14}\text{N}(p,\gamma)^{15}\text{O}$, and the rate of this reaction is dependent on the lifetime of the 6.79 MeV state in ^{15}O . The current measurements of the lifetime of this state place the lifetime around 1 fs, but the measurements vary greatly^{[1][2]}. Using solid targets with implanted ^{14}N , a new lifetime measurement will be taken with the goal of setting a new upper bound for the lifetime of this state.

As the 6.79 MeV state in ^{15}O is weakly populated, targets with large amounts of ^{14}N are essential. Implantation of N into target backings is an appropriate method of preparing targets. For this upcoming lifetime experiment, backings of Ta, Mo, and W were chosen. Varying the material of the backing, as well as the dose of N implanted, will allow the identification of

systematic trends in the data of the lifetime measurement. The implanted targets can be profiled with a proton beam of varying energies around the 1.06 MeV resonance in $^{14}\text{N}(p,\gamma)^{15}\text{O}$ and gamma ray detectors. The counts of gamma rays decaying from this state at known proton energies can be used to determine the implanted doses of N. Proper implantation and accurate measurement of the implanted doses will contribute to an accurate lifetime measurement, which in turn will provide insight into the CNO cycle, and, accordingly, stellar evolution.

Experimental Methods

Implantation

The implantation setup was constructed in the vault of the 5 MV Sta. Ana accelerator. The setup included slits set to allow a beam spot of 1 cm², a liquid nitrogen cold trap with suppression voltage, and a target holder. Before implantation began, calculations were made to approximate the time each target would need to be in the beam to achieve the desired percentage N saturation, assuming a 1 cm² beam spot, and the implantation of 1/3 of the incident N ions^[3]. The beam current delivered to the target was also taken into account for these calculations. Targets were prepared for implantation by sonic cleaning in acetone, ethyl alcohol, then isopropyl alcohol baths followed by plasma cleaning. A wobbled 350 keV beam of ^{14}N was used for implantation, and the targets were water-cooled during implantation. The Ta targets were later redone due to small implanted region, ultimately leaving 9 useable targets of differing N levels for the upcoming experiment.

Profiling

The beamline setup for target profiling was constructed in the target room of the 5 MV Sta. Ana accelerator. The profiling setup included a liquid nitrogen cold trap with a suppression voltage, a Ge gamma ray detector, and two CeBr gamma ray detectors. The targets were water-cooled during runs. The detectors were calibrated using ^{60}Co and ^{152}Eu test sources. A proton beam of varying energies was used to profile the 1.06 MeV resonance in $^{14}\text{N}(p,\gamma)^{15}\text{O}$, and three strong gamma rays, at 3.04 MeV, 5.24 MeV, and 8.24 MeV, were observed in the decay at this resonance. Data were taken with a VME-based digital data acquisition system. The N yield at each energy was calculated by dividing the counts in the peak representing each of those three gamma rays by the charge accumulated over the run, and the amount of N implanted was calculated by comparing the area under the yield curves to that of a target with known N content.

Results

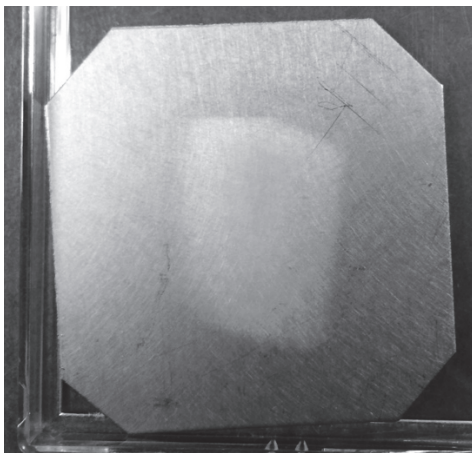


Figure 1: 30% Ta target after implantation. The light spot in the center of the target is the implanted region.

Implantation of nitrogen into the targets was successful, with implanted regions large enough to be used in the lifetime measurement. The implanted regions can be seen with the

unaided eye, appearing as lighter spots on the targets, as shown in figure 1. The water-cooling during implantation caused some corrosion on the backs of the W and Mo targets, but the implanted surfaces were unaffected. Figure 2 shows an on-resonance spectrum where the peaks at 3.04 MeV, 5.24 MeV, and 8.24 MeV are clearly distinguishable, as well as the single and double escape peaks from the 5.24 MeV and 8.24 MeV peak. These escape peaks are caused by pair production events resulting in the production of two 511 keV annihilation gamma rays. Figure 3 shows an off-resonance spectrum where those three peaks are less visible, and the largest peak is from a fluorine contaminant. However, a peak can also be seen at 6.79 MeV in figure 3, which demonstrates the feasibility of the lifetime measurement.

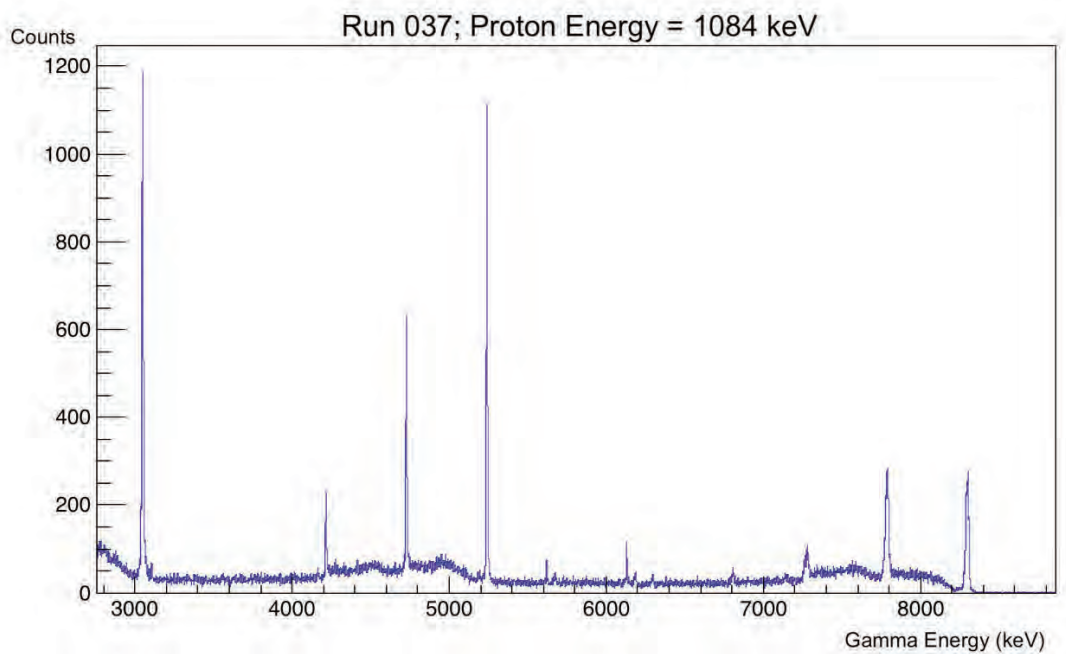


Figure 2: On-resonance spectrum for a Ta 30% target run.

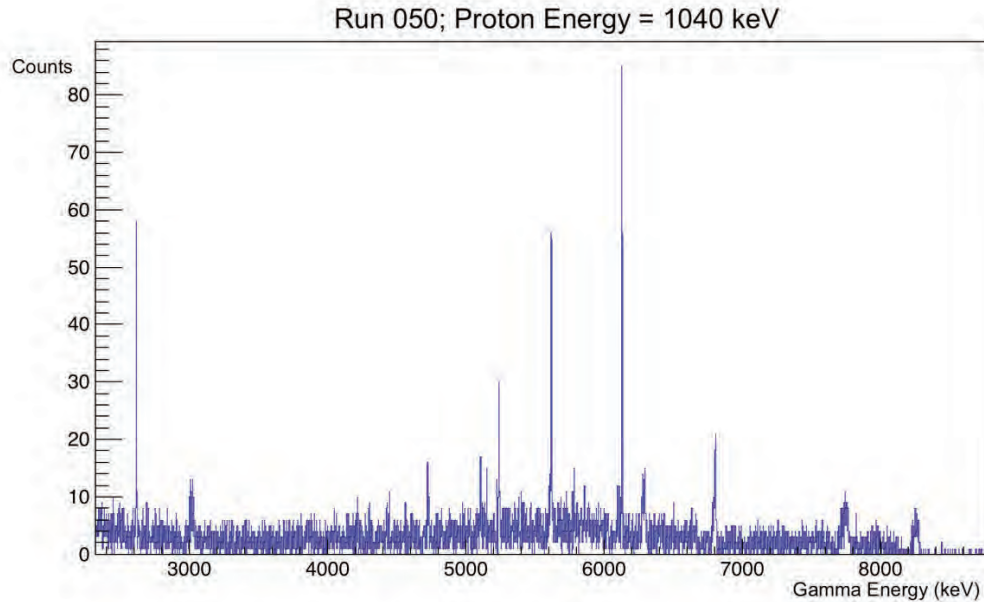


Figure 3: Off-resonance spectrum for a Ta 30% target run.

Figures 4, 5, and 6 compare the yields of the different targets of the same percent N saturation as calculated using the counts in the 5.24 MeV peaks. The different heights of the peaks is partially due to the different stopping powers of the backings, and partially due to uncertainty in the estimations made for implantation time. Figure 7 includes the profile of the TiN target with known N content. The peaks of the yield curves of the Ta, Mo, and W targets occur at higher proton beam energies due to the fact that the TiN target had the nitrogen deposited on its surface, while the other targets had the nitrogen implanted, and the protons required more energy to enter the target to interact with the nitrogen. Calculating the areas under these curves gave a method of comparing the content of the known N content target to the unknown N content targets, which further allowed for the actual percent N saturation of the targets to be calculated. These percent saturations are given in table 1.

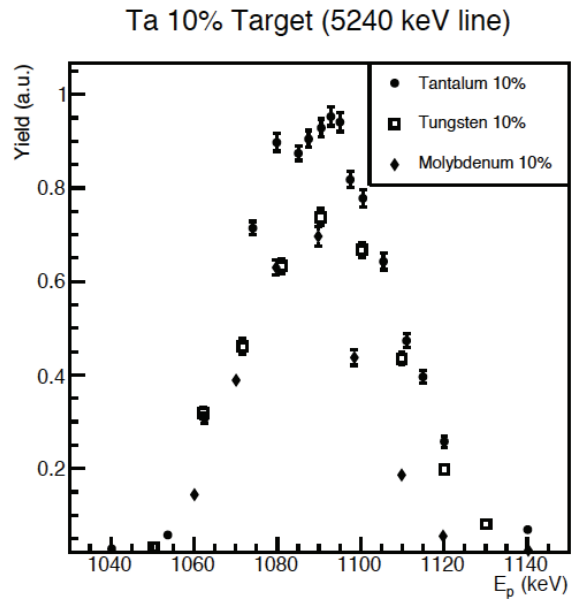


Figure 4: Comparison of yields of 10% N saturation targets of different backings at the 5.24 MeV gamma energy.

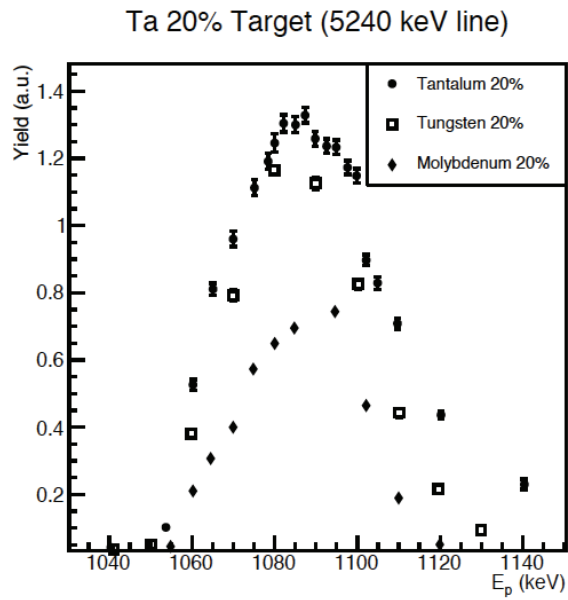


Figure 5: Comparison of yields of 20% N saturation targets of different backings at the 5.24 MeV gamma energy.

Ta 30% Target (5240 keV line)

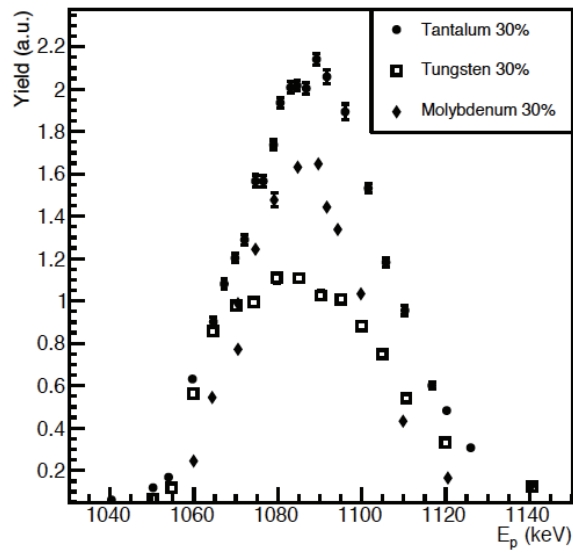


Figure 6: Comparison of yields of 30% N saturation targets of different backings at the 5.24 MeV gamma energy.

Ta 30% Target (5240 keV line)

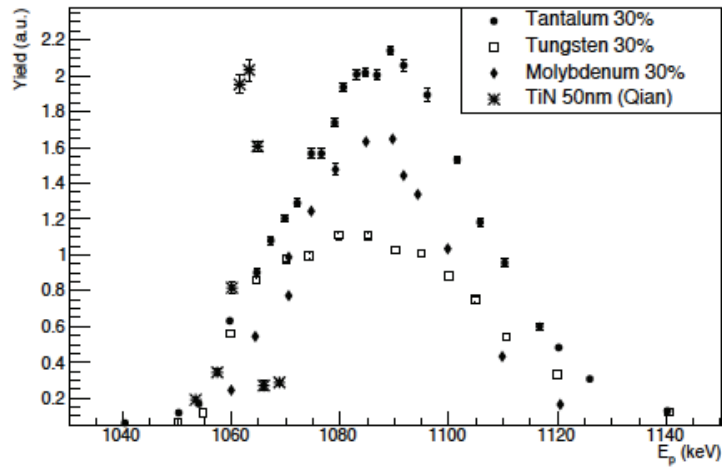


Figure 7: 30% N saturation target yield curves at the 5.24 MeV gamma energy compared to the yield curve of the TiN target of known N content.

Target	Actual percentage N saturation	Error
Mo 10%	18%	± 2%
Mo 20%	21%	± 2%
Mo 30%	44%	± 5%
Ta 10%	28%	± 3%
Ta 20%	43%	± 4%
Ta 30%	60%	± 6%
W 10%	21%	± 2%
W 20%	32%	± 3%
W 30%	37%	± 4%

Table 1: Actual percentage N saturation implanted per target.

Conclusion

Nitrogen was successfully implanted into the targets, but at a higher rate than expected. The percentage N saturation implanted exceeded the percentage expected in some cases by a factor of 1.5 to 2. However, this will not hinder the lifetime measurement. The 6.79 MeV state in ^{15}O is weakly populated, so more N will allow results to be seen much quicker. Although corrosion was noted on the backs of the W and Mo targets, the implanted regions were not affected, and this should not cause issues during the lifetime measurement. The off-resonance spectra from the profiling runs exhibit peaks at 6.79 MeV, indicating that the lifetime measurement will be feasible. There are concerns of F contamination, but the contamination should not be substantial enough to hinder results.

References

- [1]. Bertone, P.F. et al. (2001). "Lifetime of the 6793-keV State in ^{15}O ." *Physical Review Letters*, 87(15).
- [2]. Schürmann, D. et al. (2008). "Lifetime measurement of the 6792 keV state in ^{15}O , important for the astrophysical S factor extrapolation in $^{14}\text{N}(p,\gamma)^{15}\text{O}$." *Physical Review*, 77(5).
- [3]. Seuthe, S. et al. (1987). "Production and Properties of Implanted Targets." *Nuclear Instruments and Methods in Physics Research*, A260, 33-42.

A Method to Account for Hydroxide Contamination in Characterizing the
Giant Monopole Resonance to Determine an Accurate K_7

Sierra Weyhmiller

2019 NSF/REU Program

Physics Department, University of Notre Dame

Umesh Garg

Abstract

Measurements on the isoscalar giant monopole resonance (ISGMR) in finite nuclei over a range of isotopes permit the extraction of K_τ , the nuclear incompressibility asymmetry term. K_τ is critical to understanding systems with a large imbalance of protons and neutrons. A recent study has claimed that the energy of the ISGMR is higher in heavier calcium isotopes than lighter ones, indicating a positive K_τ . This is surprising when compared to most research on extracting finite nuclear incompressibilities from giant resonances. To independently verify the claim, a simultaneous study of the ISGMR of $^{40,42,44,48}\text{Ca}$ was conducted. However, contributions from hydroxide contamination were found in the ^{48}Ca foil used in the experiment. The contribution of the contaminant to the spectra had to be subtracted to ensure an accurate strength distribution extraction.

Introduction

K_τ , the nuclear incompressibility asymmetry term, is an essential parameter for the nuclear equation of state (EOS) for asymmetric matter. The nuclear EOS describes the binding energy per nucleon in terms of nuclear density. It is used to understand several interesting phenomena, including supernovae and neutron stars [1].

A K_τ value can be extracted from measurements on the ISGMR in finite nuclei over a range of isotopes. The ISGMR is a high-frequency, damped, nearly harmonic density vibration around the equilibrium density of the nuclear system, depicted in Figure 1. The ISGMR is directly related to K_A , the incompressibility of a particular nucleus, via

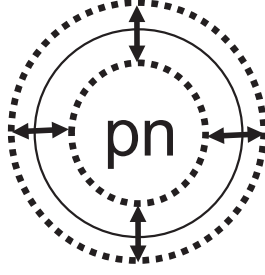


Figure 1: A depiction of the ISGMR resonance. Here, pn stands for protons and neutrons.

$$E_{\text{ISGMR}} = \hbar \sqrt{\frac{K_A}{m \langle r_0^2 \rangle}} \quad (1)$$

where E_{ISGMR} is the energy needed to induce the ISGMR state and $\langle r_0^2 \rangle$ is the ground-state mean-square radius of the nucleus [2]. Further, K_A is related to K_τ via

$$K_A \approx K_\infty (1 - A^{-\frac{1}{3}}) + K_\tau \eta^2 + K_{\text{Coul}} \frac{Z^2}{A^{\frac{4}{3}}} + \dots \quad (2)$$

where A is the mass number, Z is the atomic number, η is $\frac{N-Z}{A}$ (N is the number of neutrons), K_{Coul} is -5.2 ± 0.7 MeV, and K_∞ is 240 ± 20 MeV [2].

The goal of this experiment is to support or refute a controversial K_τ value proposed by a contemporary group at Texas A&M. This group claims that the heavier calcium isotopes are more incompressible than the lighter isotopes, as indicated by $K_\tau = +500$ MeV, rather than the negative value that has been previously measured [3].

Experiment

A simultaneous study of the ISGMR of the $^{40,42,44,48}\text{Ca}$ nuclei was conducted at the Research Center for Nuclear Physics, Osaka University in November 2018. The calcium

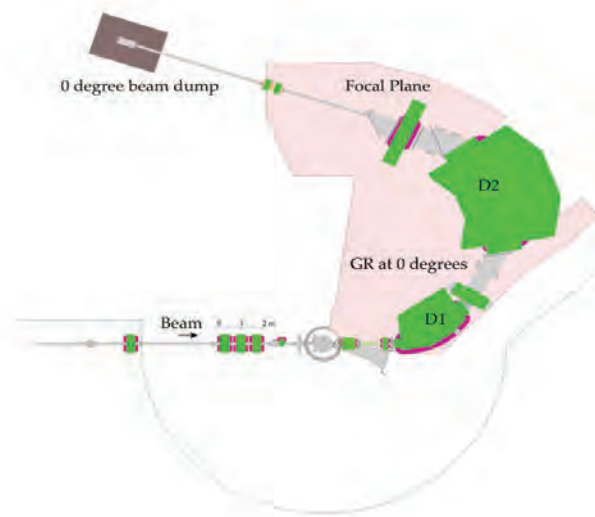


Figure 2: Schematic of Grand Raiden. Figure courtesy of Atsushi Tamii.

isotopes were excited with 386 MeV α particles. These α particles were scattered off the calcium targets and then into the spectrometer, Grand Raiden, which separated the α particles according to their momentum. Upon examining the spectra, it was discovered that the ^{48}Ca isotope was partially oxidized. At some angles, the contaminant line crossed the excited state of ^{48}Ca , meaning that the momentum of the ejected alpha elastic scattering off the contaminant nucleus was the same as its inelastic scattering off of the excited ^{48}Ca state (see Figure 3). Thus, the mass number that gave an elastic scattering momentum equal to the momentum of the ^{48}Ca inelastic scattering at the given laboratory-frame angle was calculated to be ^{16}O (see Figure 4). The contribution of the contaminant to the measured angular distributions must be accounted for to accurately determine the GMR strength distribution.

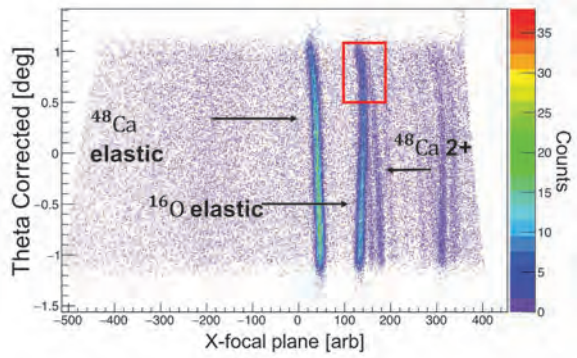


Figure 3: Theta Corrected vs. x-focal plane for the 12.8° elastic ^{48}Ca run. The box marks the intersection of the ^{16}O elastic state and the ^{48}Ca excited state.

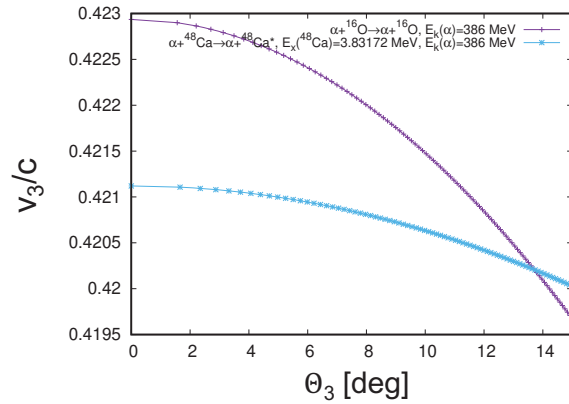


Figure 4: Velocity of ejectile vs. scattering angle. The purple line corresponds to $^{16}\text{O}(\alpha,\alpha)$ elastic scattering and the blue line corresponds to $^{48}\text{Ca} 2+$ inelastic scattering.

Data Reduction

To determine the amount of oxygen present in the target, one must find the counts arising solely from $^{16}\text{O}(\alpha,\alpha)$ elastic scattering. First, one must identify which events correspond to α particle scattering. The rate of energy loss of any charged particle as it travels through the target is dependent on that particle's velocity and charge [2]. Thus, one can measure the energy a particle deposits into the scintillator after it exits the target to identify which particle it is.

Next, one must remove any background events. Background events occur when α particles have the same momentum as if they truly scattered off the target, but actually originated from the α particle scattering off of other objects. Due to the optical properties

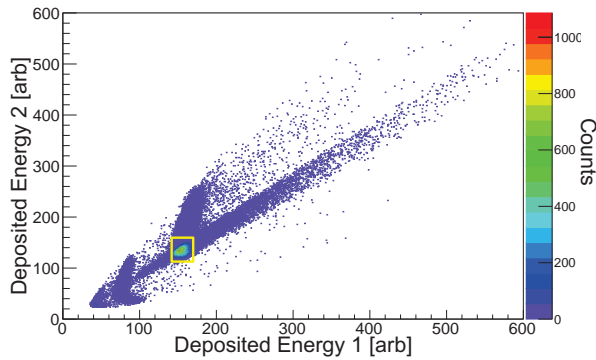


Figure 5: Particle Identification

histogram for the 8° elastic ^{48}Ca run.

The boxed region corresponds to the α particles of interest.

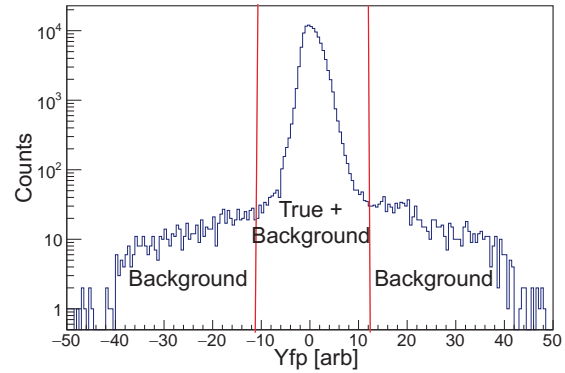


Figure 6: Background Subtraction

histogram for the 8° elastic ^{48}Ca run.

The lines mark the boundaries of the regions.

of the spectrograph, the true events congregate in a sharp peak along the y-focal plane, while the background events form a flat distribution. These regions were distinguished, the total background counts were determined, and a normalized amount of this background was subtracted from the true + background region.

Due to the optical properties of the spectrograph, the θ -scattered vs. x-focal plane spectrum becomes slanted. To remedy this, the spectrum was straightened with a 2nd-degree polynomial fit. With a straightened oxygen line, there is less overlap between the oxygen state and calcium states. After integrating in this region, one has obtained the counts arising solely from $^{16}\text{O}(\alpha,\alpha)$ elastic scattering, as desired (see Figure 8).

Data Analysis

The thickness of any target (contaminant or otherwise) can be determined from

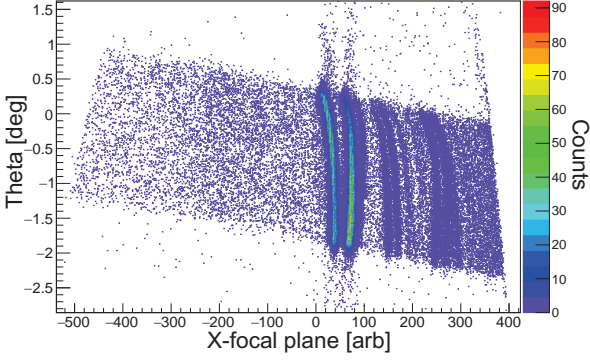


Figure 7:

Theta Scattered vs. x-focal plane for the 8° elastic ^{48}Ca run before shape correction.

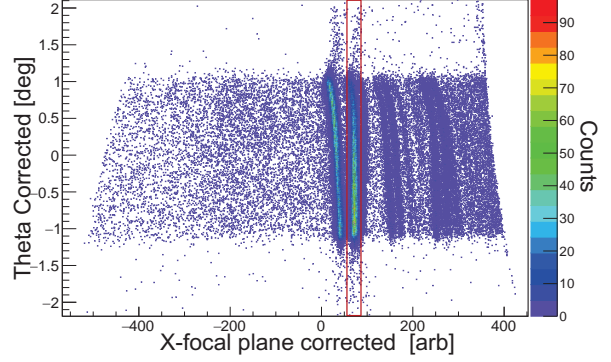


Figure 8: Theta Scattered vs. x-focal

plane for the 8° elastic ^{48}Ca run after shape correction. The box marks the ^{16}O elastic state.

$$\frac{d\sigma}{d\Omega} = \frac{YA}{kQ\Delta\Omega\Delta x\epsilon_{VDC}} \quad (3)$$

where $\frac{d\sigma}{d\Omega}$ is the cross section (mb/sr), Y is the true counts, A is the mass number (AMU), k is a conversion factor ($6.022\text{e-}7 \frac{\text{mg}/\text{cm}^2}{\text{AMU}}$), Q is the incoming beam charge (nC), $\Delta\Omega$ is the solid angle (msr), Δx is the thickness (mg/cm^2), and ϵ_{VDC} is the VDC efficiency. Y can be obtained after data reduction, and A , $\Delta\Omega$, Q , and ϵ_{VDC} are known experimental parameters. Thus, determining the cross sections for $^{16}\text{O}(\alpha,\alpha)$ elastic scattering in the lab frame at the run angles allows one to determine the thickness of the ^{16}O contaminant.

$^{16}\text{O}(\alpha,\alpha)$ elastic scattering cross sections have been published in the center of momentum (CM) frame and were converted to the lab frame for use in this analysis [4]. However, these cross sections correspond to different angles than those used in the present experiment. Thus, the published cross sections were interpolated using a cubic spline (see Figure 9).

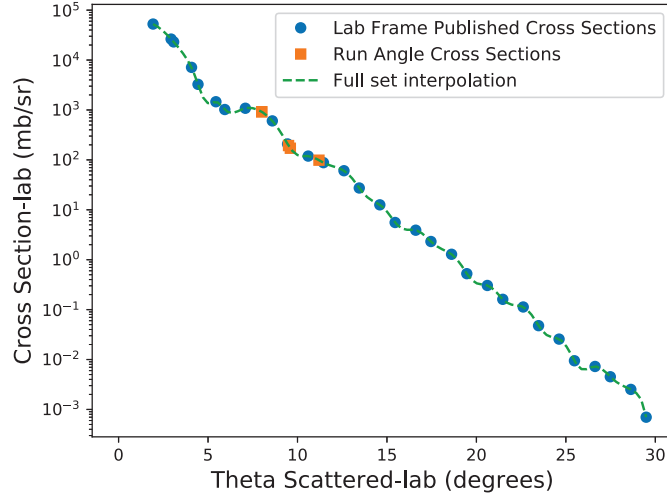


Figure 9: Cross Section interpolation. Data adapted from Ref. [4].

Error Analysis

The oxygen thickness uncertainty is given by

$$\delta x = \sqrt{\left(\frac{\sqrt{Y}}{Y}\right)^2 + \left(\frac{\delta \frac{d\sigma}{d\Omega}}{\frac{d\sigma}{d\Omega}}\right)^2} \Delta x \quad (4)$$

where δx is thickness uncertainty, Y is true counts, $\frac{d\sigma}{d\Omega}$ is cross section, $\delta \frac{d\sigma}{d\Omega}$ is cross section uncertainty, and Δx is thickness. At this point in the analysis, only the cross section uncertainty remains to be determined.

First, the inherent experimental uncertainty from the original published data was converted from the CM frame to lab frame. Then, this uncertainty was interpolated to the run angles by a cubic spline fit of the lab frame angle and uncertainty. Next, the uncertainty associated with interpolating the cross sections themselves had to be accounted for. To do this, half the experimental data was cubic spline fitted, from which the other half of the

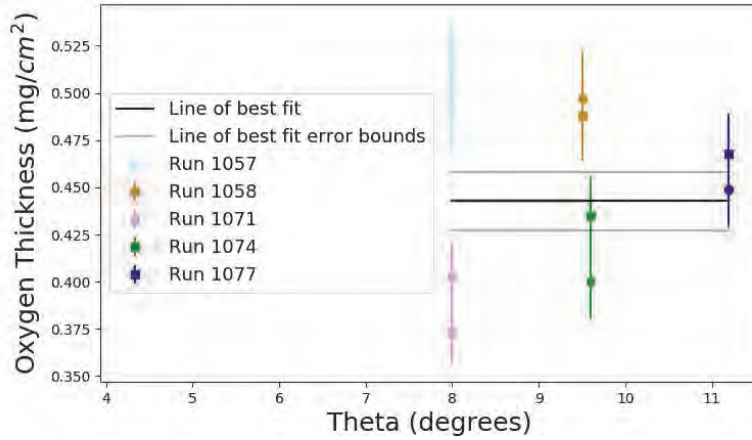


Figure 10: Oxygen Thickness Calculations. The line of best fit is 0.44 ± 0.02 mg/cm².

data was interpolated. The difference between the interpolated experimental data and the measured experimental data represented the error associated with this half-set interpolation.

The full-set interpolation error was then determined for each point using

$$E_{full} \leq E_{half} \left(\frac{h_{full}}{h_{half}} \right)^4 \quad (5)$$

where E_{full} is the full-set interpolation error, E_{half} is the half-set interpolation error, h_{full} is the full-set interpolation step size (0.919), and h_{half} is the half-set interpolation step size (1.753). To ensure that this uncertainty encompasses any point on the interpolation, the highest percent uncertainty (4.4%) was used for each lab angle. The total cross section uncertainty is the sum of the experimental uncertainty and the interpolation error.

Results and Discussion

Oxygen thicknesses were calculated from five elastic runs with $\Delta\Omega=12$ msr and a constant line of best fit was determined. The thickness of the ¹⁶O contaminant was found to

be 0.44 ± 0.02 mg/cm². Using this thickness, the appropriate number of counts arising from the oxygen contamination was subtracted from the excitation spectra of $^{48}\text{Ca} + ^{16}\text{O}$. The analysis of this spectra and the extraction of a K_τ value is ongoing.

References

- [1] J. Piekarewicz. *Unmasking the nuclear matter equation of state* Phys. Rev. C 69, 041301(R), 2004.
- [2] Darshana Patel. *A Study of the Isoscalar Giant Monopole Resonance: The Role of Symmetry Energy in Nuclear Incompressibility in the Open-shell Nuclei*. University of Notre Dame, Notre Dame, IN, 2015.
- [3] J. Button, Y.-W. Lui, D. H. Youngblood et al. *Isoscalar $E0$, $E1$, and $E2$ strength in ^{48}Ca* Physical Review C 96, 054330, 2017.
- [4] T. Wakasa, E. Ihara, K. Fujita et al. *New candidate for an alpha cluster condensed state in ^{16}O (α, α') at 400 MeV* Physics Letters B Volume 653 Issues 2-4 Pages 173-177, 2007.



**Mean Filter Method to Find and Identify Peaks for
PIGE and PIXE and Signal Sensitivity Analysis for
2.4-5.1 MeV Protons**

Jingxu Xie

2019 NSF/REU Program

Department of Physics, University of Notre Dame

Advisor: Prof. Graham Peaslee

Abstract

In this study, we analyze the PIGE and PIXE data for different proton beam energies: 2.4MeV, 3.4MeV, 4.2MeV, 5.1MeV of elements with $Z=9, 11-17, 19-23, 25-30, 35, 37, 40-42, 44-45, 47, 49-50, 53, 55-56$. We introduce a mean filter method to smooth raw data, to determine and subtract backgrounds, to find peaks, and to integrate and to normalize the peak areas. Then we obtain tables of γ -ray and X-ray signal sensitivities for each of the different proton beam energies. Lists of elements observed by γ -rays and X-rays were tabulated for each spectrum.

1 Introduction

Particle induced prompt γ -ray emission (PIGE) is a good way to analyze the light elements in samples according to the known γ -ray energies of each isotope. However, sometimes it is hard to identify peaks in a spectrum because there might be a lot of background noise and to find and identify every peak manually is a time-consuming task. Moreover, for some elements, they might not be enough proton energy to induce γ -ray emission, since the signal sensitivity is quite different for different proton energies. Measuring the sensitivity of elements as a function of proton energy can help us better identify materials when running samples and analyzing peaks. Thus, a good method is needed to subtract backgrounds as well as to find and identify peaks automatically. We also want to make a table of elements and isotopes observed by their unique energies for each spectra, and to identify their relative signal sensitivity.

In 1980s, Kiss^[1] (1984) and Räsänen^[2,3] (1982, 1987) measured many elements γ -ray emissions at low energy (2.4 MeV) and high energy (7 MeV) and made tables of target γ -ray yields. But there are no data published in the medium energy proton energies between 2.5 - 7 MeV.

Since PIXE can also be used to measure both light and heavy elements simultaneously with PIGE, we can often use PIXE to reconfirm our elemental identification using X-ray data. There is also limited X-ray data about X-ray emission on these elements as a function of proton energy. Therefore our experiment was designed to collect both the γ -ray and the X-ray data for each of the four energies for a wide variety of elements and to analyze their peak sensitivity.

2 Experimental Method

In our experiment, we used the Alpha toss ion source and the 9SDH 3MeV St. Andre accelerator at the University of Notre Dame (see Fig.1) to generate accelerated proton beams of 2.4 MeV, 3.4 MeV, 4.2 MeV and 5.1 MeV by adjusting the accelerating voltage. The whole accelerator system runs in high vacuum about 10^{-7} torr, to reduce the energy loss of proton beams before they hit the target. We also use magnetic quadrupoles to focus the proton beam and magnetic dipoles to bend the beam onto our targets.

Non metallic target samples are typically ground into powder and mounted into small bags, which are around



Figure 1: Alpha toss ion source and 9SDH St. Andre accelerator facility at the University of Notre Dame. The box on the left is the alpha toss which generates either H or He ions. The big blue tank holds a 3 MeV tandem accelerator.

10mm× 10mm in size, and about 2mm thick. Then tape is used to stick the bags to our stainless steel target frames, which are then attached to the target wheel (see Fig.2). Each target frame has a hole in center to let the beam go through target sample. We run samples *ex vacuo* for approximately three minutes of beam at approximately 50 nA current on target. In our experiment, we used samples of Ag₂S, BaOH, CaCO₃, Co₃P₂, CsCl, CuCl₂, Dy, NaF, FeCl₃, In, KBr, KI, MgCO₃, MgSO₄, Mn(OAc)₂, Mo, N₂NiO₄, NaHCO₃, Nd₂O₃, Pt, RbCl, Rh, RuO₂, SiO₂, Sm₂O₃, Ti, ZnS.



Figure 2: Target wheel and γ -ray detector. One wheel can mount and rotate each of sixty samples into the beam. The γ -ray detector is at the right of the target wheel and the X-ray detector is behind the wheel at top right in this figure.

3 Measurement and Data Analysis

The counts received by the high-purity germanium detector for each different γ -ray energy are recorded in each analysis. The raw data of Ag₂S sample for 3.4 MeV protons is shown in Fig.3. The γ -ray energy ranges from around 50 keV through 2500 keV. In the figure several dominant peaks can be seen and the energy of the peaks can be readily identified by eye and their identifications known by looking up online γ -ray charts of nuclides.

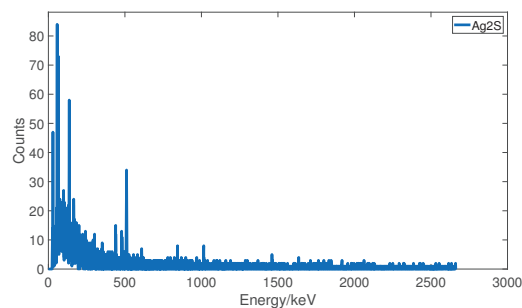


Figure 3: γ -ray raw spectrum of Ag₂S with 3.4 MeV protons. There are clear dominant peaks as well as a lot of background noise in this figure.

However, many peaks are generated from background reactions, for example, 511 keV is from positron annihilation. And if we zoom in on an area of the spectrum, as shown in Fig.4, we can see that there is a lot of background noise and even for the peaks, there are a lot of fluctuations. Also, the background noise intensity is different for different detection energies, for instance, the background noise is higher at low energy (less than 500 keV) than in high energy (more than 1000 keV). That is because our γ -ray detector sensitivity is different at dif-

ferent energies. It is much more sensitive at low energy than at high energy. So first we smoothed the spectrum to find the average background and then subtracted it off to identify the actual peaks.

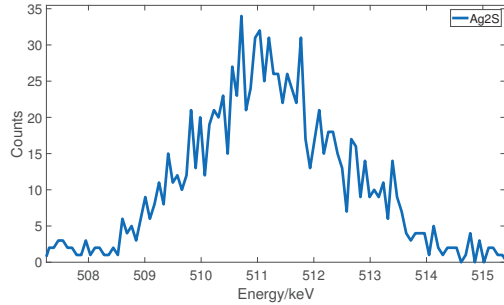


Figure 4: γ -ray raw spectrum of Ag_2S for 3.4 MeV protons, zoomed in around 511 keV (positron annihilation peak).

3.1 Spectrum Smoothing

We used a Mean Filter Method to smooth the spectrum. For each data point, we calculated the average of three points before and after and took this average value as the value of the selected point. This process was repeated for all points except for a few points at the beginning and the end of the spectrum because there is no before or after points with which to take an average for them. After doing this averaging, we obtain a new set of data. And we repeat the procedure for each spectrum 10 times. Then we get a satisfactorily smoothed curve of modified data that represents the spectrum accurately. As shown in Fig.5, the blue thin line is raw data and the red thick curve is the smoothed curve after using the Mean Filter Method. The smoothed curve lowers the peak height to some extent, but this does not affect our

calculated peak energy which is used for identification of the emitting nucleus. In general, the smoothed curve well represents the peaks shape and position, and it reduce the fluctuations of raw data which helps to identify

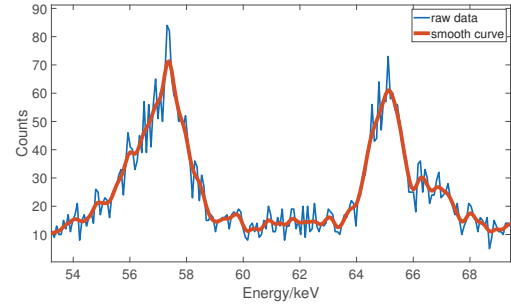


Figure 5: For the same spectrum shown before the mean filter smoothed curve (thick red line) and the raw data (thin blue line), zoomed in around 54-68 keV

the gamma peaks accurately. It also shows us a clear line of background, which is used to find the background subtraction.

3.2 Determining the Background

From Fig.5, we can see that most of the background noises fluctuations have been reduced. But there are still some fluctuations in the smooth curve. So we utilize these fluctuations to determine the background value at different γ -ray energies.

To determine the background, we first find all the local minima of the smooth curve. However, if two peaks overlap, there would be a minimum between two peaks but it is much higher than background. So we designed a filter to eliminate those minima points on the peaks. To do so, we compare all the local minima with their adjacent points. Specifically, for any point, we calculate the

average of two lower energy and two higher energy minima separately. Then we compare the point value with these averages. If it is larger than both of the averages, then the point is regarded as an invalid minimum and eliminated. After determining all the valid minima, we use the Mean Filter Method to smooth these minima and then use the smoothed curve as the background which will be subtracted later.

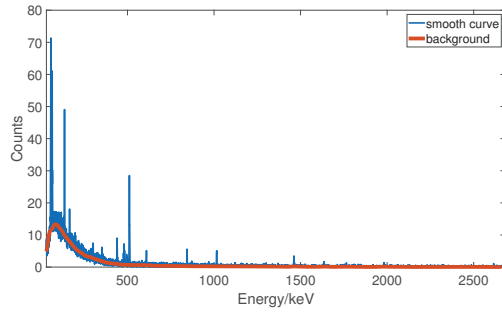


Figure 6: Smoothed spectrum (thin blue line) and background (thick red line) of Ag_2S for 3.4 MeV protons.

In Fig.6, the thick red line shows the background determined by these methods, and the thin blue line is the smoothed spectrum. This figure clearly shows the larger background at low energy and smaller background at high energy.

3.3 Finding Peaks and Integrating Peaks

Once the background is determined, it is subtracted from the smoothed spectrum to find the peaks of interest. After subtracting the background, although there are still some noise fluctuations, they are all centered around zero and the positive and negative numbers are roughly equal, which confirms a proper background subtraction.

To find the peaks, all the local maxima are identified, ²⁹³ one and retain the higher one. Then we compare the re-

and then thresholds are set to eliminate false peaks, including peaks that overlap too much, and small peaks. We find that the residual background noise fluctuations are related to the value of the background, i.e., higher background usually has higher noise fluctuations. So we set different thresholds according to different background values. Generally, we set the threshold as twice of the local background noise. If the maxima is lower

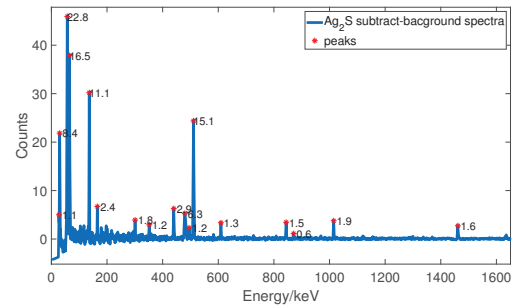


Figure 7: Subtracted background spectrum and peaks with normalized area. The blue line is the smoothed curve of raw spectrum for which the background has been subtracted. The red asterisks show the position of peaks found in the Ag_2S spectrum for 3.4 MeV protons. The numbers near asterisks show the normalized area of every peak.

than the threshold, then it is disregarded as a small peak and eliminated. As for overlapped peaks, we set a overlapped threshold as 0.75. This means for every adjacent peak, we first find the lowest point between the two peaks and then compare the minimum value with the lowest peak height. If the minimal value is higher than 0.75 of the lowest peak height, the two peaks are viewed as undistinguishable and we eliminate the lower

tained peak with next peak.

After locating the final significant peaks, we continue to locate the peak bases of every peak. For each peak, we first find two locations (before and after the peak) at half the height of the maximum. Then the distance between the half-height points is calculated and the summit of the peak identified. Then we multiply the half-height distances by a factor of 1.7 to locate the peak base. That is because the Full Width at Half Maximum (FWHM) is about 2.4σ and the peak width is about 4.2σ . So the peak width is about 1.7 times FWHM. Then we use a trapezoid method to integrate the peak area from one peak base to another channel by channel. We then normalize the areas observed by the total integrated charge of proton beam on target, i.e., divide the area by the beam current multiplied by the run time for each sample. The background-subtracted spectrum and the peaks found with normalized areas are shown in Fig.7.

3.4 X-ray Data Processing

X-ray data are easier to analyze because they typically do not have too much background noise in our system. Therefore, it is not necessary to determine and subtract background. The other procedures are the same as dealing with γ -ray data. The X-ray spectrum of Ag_2S for 3.4 MeV protons is shown in Fig.8.

4 Results

We ran the program described above for all of our samples recorded in 2017 and 2018, which is more than 294

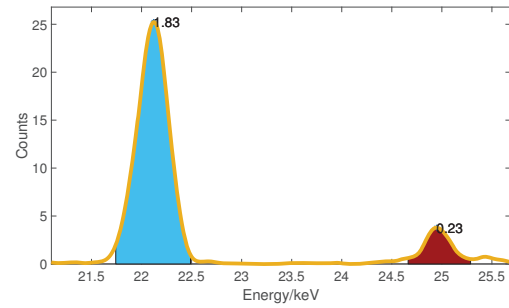


Figure 8: X-ray data after processing. The thick yellow line shows the smoothed spectrum. The colored areas are the peaks identified and the number near the peaks are normalized peak areas. The dominant two peaks are 22.1 keV and 24.9 keV, which are the K_α and K_β decay of silver in this case.

500 separate spectra. The table of γ -ray and X-ray lines identified for different elements and isotopes is shown below. We also calculate the signal sensitivity for different elements based the amount in sample and the natural abundance of isotopes in each target. This is helpful because for each peak in future analyses you can look up our tables to determine the what the element corresponds to which peak. Often identifications can be confirmed by using PIGE and PIXE data simultaneously. It is possible to select appropriate elements to identify in each spectrum according to our signal sensitivity table as a function of beam energy.

Table 1: Isotopes for γ -ray peaks

Energy(keV)	Isotope	Energy(keV)	Isotope
110	^{19}F	808	^{51}V

121.5	¹⁵² Sm	843	²⁷ Al	390	²⁵ Mg	1274	²⁹ Si
122	⁵⁷ Fe	847	⁵⁶ Fe	411	⁵⁵ Mn	1294	⁴¹ K
126	⁵⁵ Mn	858.5	⁵⁵ Mn	415	¹⁰⁹ Ag	1300	¹¹⁴ Sn
127	¹⁰¹ Ru	889	⁴⁵ Sc	423	¹⁰⁷ Ag	1312	⁴⁸ Ti
130	¹⁵⁰ Nd	889	⁴⁶ Ti	431.5	⁴⁵ Sc	1327	⁶³ Cu
159	⁴⁷ Ti	926.5	⁴⁵ Sc	440	²³ Na	1333	⁶⁰ Ni
170	²⁷ Al	928.5	⁵¹ V	454	¹⁴⁶ Nd	1368	²⁷ Al
172	¹²⁷ I	931	⁵⁵ Mn	475	¹⁰² Ru	1369	²⁴ Mg
182.5	⁷⁹ Br	962	⁴⁵ Sc	484.5	⁸⁷ Rb	1380	²⁵ Mg
190	⁸¹ Br	962	⁶³ Cu	520.5	⁴⁸ Ca	1408	⁵⁵ Mn
197	¹⁹ F	974.5	⁴⁵ Sc	523	⁷⁹ Br	1410	³⁷ Cl
203	¹²⁷ I	975	²⁵ Mg	530.5	⁴⁵ Sc	1438	⁴⁸ Ti
217	⁷⁹ Br	980.5	⁴¹ K	539.5	¹⁰⁰ Ru	1454	⁵⁸ Ni
231.5	⁸⁵ Rb	983.5	⁴⁸ Ti	543	⁴⁵ Sc	1480	⁵¹ V
255	¹¹³ In	1014	²⁷ Al	550	¹⁴⁸ Sm	1525	⁴² Ca
276	⁸¹ Br	1024	¹¹³ In	585	²⁵ Mg	1609	⁵¹ V
302	¹³³ Cs	1049	⁴⁵ Sc	617	⁷⁹ Br	1611	³⁷ Cl
302	¹⁴⁸ Nd	1093	⁴⁷ Ti	628.5	¹²⁷ I	1634	²³ Na
306	⁷⁹ Br	1120.5	⁴⁵ Sc	632	¹³³ Cs	1643	³⁷ Cl
311	¹⁰⁹ Ag	1131	¹¹³ In	638	¹¹³ In	1663	⁴⁵ Sc
320	⁵¹ V	1149	⁵¹ V	670	⁶³ Cu	1728	³⁷ Cl
324	¹⁰⁷ Ag	1157	⁴⁴ Ca	691	⁴⁵ Sc	1763	³⁵ Cl
334	¹⁵⁰ Sm	1165	⁵¹ V	696.5	¹⁴⁴ Nd	1779	²⁸ Si
338	⁵⁹ Co	1220	³⁵ Cl	700	¹¹⁹ Sn	1809	²⁶ Mg
358	¹⁰⁴ Ru	1228	⁸⁷ Rb	720.5	⁴⁵ Sc	1813	⁵¹ V
364	⁴⁵ Sc	1235	¹⁹ F	749	⁵¹ V	1943	⁴¹ K
370.5	⁴⁸ Ca	1237	⁴⁵ Sc	780	⁴⁸ Ca	2028	^{29,30} Si
383	¹³³ Cs	1263.5	⁵⁹ Co	804	⁵⁵ Mn	2128	³⁷ Cl

Table 2: PIGE relative signal sensitivity of isotopes

Element	Signal Sensitivity (MeV)			
	$E_p=2.4$	3.4	4.2	5.1
^{107}Ag	0	0	0	223
^{109}Ag	0	0	14	274
^{27}Al	0	193	9494	47600
^{79}Br	0	65	858	5663
^{81}Br	0	41	599	4754
^{42}Ca	0	0	0	5748
^{44}Ca	0	0	1339	7699
^{48}Ca	0	1688	25650	112388
^{35}Cl	0	0	293	2298
^{37}Cl	0	0	0	2686
^{133}Cs	0	4	21	58
^{63}Cu	0	0	61	941
^{19}F	135	37626	265322	684468
^{56}Fe	0	0	291	3210
^{57}Fe	0	0	0	4958
^{127}I	0	0	0	69
^{113}In	0	0	0	3316
^{41}K	0	0	695	10043
^{24}Mg	0	140	2223	13178
^{25}Mg	0	3388	20827	60306
^{26}Mg	0	0	5042	14064
^{55}Mn	0	794	9852	60556
^{58}Ni	0	0	0	249

^{60}Ni	0	0	0	237
^{23}Na	0	184	3012	50070
^{144}Nd	0	0	0	48
^{146}Nd	0	7	79	225
^{148}Nd	0	88	473	1118
^{150}Nd	0	284	1063	2051
^{85}Rb	0	0	115	746
^{87}Rb	0	0	87	357
^{100}Ru	0	0	0	282
^{101}Ru	0	0	0	294
^{102}Ru	0	8	103	484
^{104}Ru	0	33	323	1250
^{45}Sc	0	238	2606	12396
^{28}Si	0	0	2066	7914
^{29}Si	0	49	4735	19182
^{30}Si	0	0	0	4467
^{150}Sm	0	30	279	1035
^{152}Sm	0	205	838	2386
^{154}Sm	0	45	144	515
^{114}Sn	0	0	11286	0
^{119}Sn	0	0	0	137
^{46}Ti	0	8	1637	8813
^{47}Ti	0	724	13589	47351
^{48}Ti	0	7	1339	7964
^{51}V	0	13	1322	9326

Table 3: X-ray peaks and signal sensitivity

Element	Energy (keV)	Signal Sensitivity(MeV)			
		2.4	3.4	4.2	5.1

Ag	22.1	0	2	53	258	I	28.5	0	0	10	56
	24.9	0	0	8	41		32.3	0	0	1	8
Ba	4.5	0	2	4	6	Mn	5.9	14	1099	3754	0
	4.8	0	5	11	18		6.5	6	392	1374	47
	32.2	0	1	4	12						
	36.3	0	0	1	2	Mo	17.5	33	678	1882	3810
							19.6	5	124	356	721
Br	11.9	7	728	2764	5966						
	13.3	1	155	609	1353	Ni	7.5	0	344	1723	3310
							8.3	0	88	448	875
Co	6.9	1	116	655	1319						
	7.6	0	26	159	344	Nd	5.2	1	10	24	29
							5.7	1	24	59	75
Cs	4.3	0	0	1	1						
	4.6	0	1	3	5	Pt	7.4	269	2599	1184	2266
	30.9	0	5	30	68		8.2	64	639	321	617
	34.9	0	1	5	10						
						Rb	13.4	0	64	237	1516
Cu	8	2	450	2304	3840		15	0	11	42	285
	8.9	1	110	597	1024		13.4	2	349	1219	2171
							15	0	68	249	461
Dy	6.5	0	4	53	243						
	7.2	0	3	46	297	Rh	20.2	18	292	1142	2035
							22.7	3	46	184	334
Fe	6.4	8	240	863	1603						
	7	3	77	293	569	Ru	19.2	0	57	382	0
							21.7	0	10	69	0

Table 3: (continued)

Element	Energy (keV)	Signal Sensitivity(MeV)			
		2.4	3.4	4.2	5.1
Sc	4.1	0	2	8	11
	4.4	0	3	9	14
Sm	5.6	2	39	90	160
	6.2	2	69	181	335
Sn	25.2	0	13	81	201
	28.5	0	2	13	34
Ta	8.1	3	78	186	609
	9.3	2	75	197	761
Ti	4.5	0	7	18	22
	4.9	0	6	15	19
V	5	0	19	96	134
	5.4	0	9	53	75
W	8.4	0	53	421	427
	9.7	0	39	421	651
Zr	15.7	1	59	295	644
	17.7	0	11	55	122
Zn	8.6	0	27	447	6
	9.6	0	6	100	0

5 Discussion

In our data analysis, the background-subtracted mean smoothed curve was used to integrate the peak areas. As discussed above, our curve smoothing will lower the peak height, which causes some uncertainty. We can do uncertainty analysis by using FWHM. We plan to combine Föurier Transformation Filter Method in the future to smooth the spectrum to overcome the shortcomings of the Mean Filter Method.

Acknowledgement

During this summer, I have received much useful guidance and advice and I thank all those students and the professor who took the time to help me. I greatly thank professor Graham Peaslee for giving me this project and for his patient guidance. I am grateful to John Wilkinson and Sean McGuinness who taught me a lot of nuclear physics. And I thank Emily McGill, Matt Roddy, Alec Gonzales and Nick Caterisano for their warm help.

References

- [1] Á. Z. Kiss, et al. Measurements of Relative Thick Target Yields for PIGE Analysis on Light Elements in the Proton Energy Interval 2.4-4.2 MeV, Journal of Radioanalytical and Nuclear Chemistry, Physical Methods Section, 1984.
- [2] J.Räisänen et al. Heavy Element ($Z>30$) Thick-Target Gamma-Ray Yields Induced By 1.7 and 2.4 MeV Protons, Nuclear Instruments and Methods, 1982.
- [3] J. Räisänen et al. Absolute Thick-Target γ - Ray Yields for Elemental Analysis by 7 and 9MeV Protons, Nuclear Instruments and Methods in Physics Research, 1987.



St. George Group

CALCULATION FOR HIPPO

Simulation of the elastic scattering in the HIPPO gas-jet target of the St. George recoil separator

Haobo Yan ¹

2019 NSF/REU Program

Physics Department, University of Notre Dame

Advisor: Manoël Couder ²

¹School of Science, Xi'an Jiaotong University, Xi'an 710049, People's Republic of China

²Department of Physics, Joint Institute for Nuclear Astrophysics, University of Notre Dame, Notre Dame, IN 46556, USA

Abstract

Nuclear-reaction cross sections play a pivotal role in understanding the evolution of the elements, energy production, and nucleosynthesis during stellar formation. In this work, the cross section of an (α, γ) reaction is studied in inverse kinematics. The St. George recoil separator at the University of Notre Dame's Nuclear Science Laboratory is used to separate the beam that did not interact in the HIPPO helium gas jet target from the products of a reaction. The number of reaction products detected is proportional to the cross section, the transmission efficiency of St. George, the beam intensity, and the target thickness. The intensity of the incident ion beam is deduced from the number of elastically-scattered helium in a detector placed at 65° . A calculation was implemented to deduce intensity from the experimental energy spectra. The calculation is based on the finite element method (FEM) and includes the energy loss and straggling of the beam through the target. The calculation results agree well with the experimental data. Our approach provides an accurate and efficient method to compute the intensity of the incident beam and provides one of the key ingredients for the measurement of the (α, γ) reaction cross section.

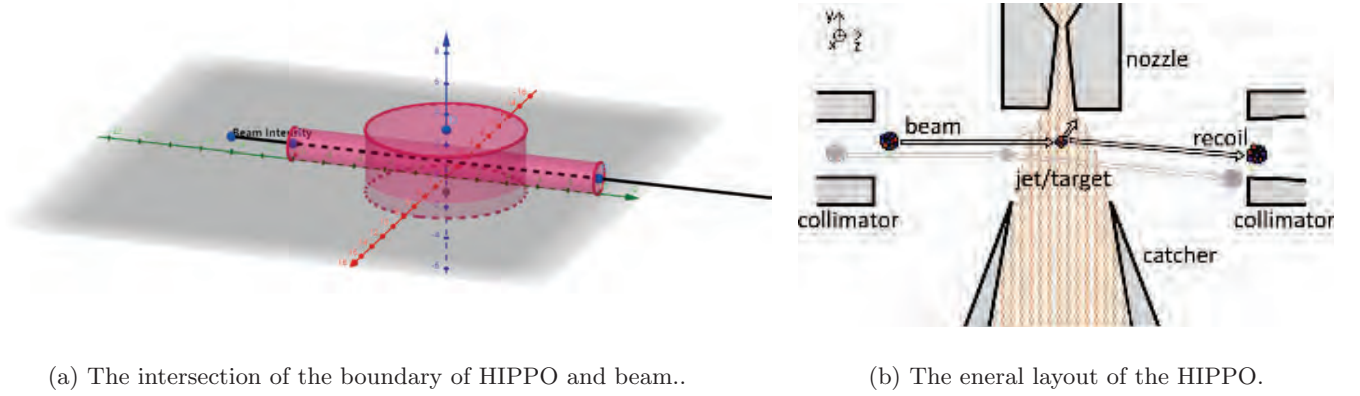
1 Introduction

The object we are analyzing is HIPPO (High Pressure POint like gas target), the target of the St. George recoil separator [1]. The supersonic and windowless design makes HIPPO produce a confined region of gaseous helium, which is the requirement of recoil nuclei capture [2]. A heavy incident beam gains energy from 5U accelerator impinges on HIPPO. Precise (α, γ) reaction cross sections are crucial to accurately model a variety of astrophysical phenomena. Direct kinematic to detect the gamma rays has been done for decades. To measure smaller and smaller cross sections, high efficiency and signal that is larger than the background are hence needed. Besides, the elastic

measurement is critical to provide normalization of the measurement of the recoil nuclei.

The jet is produced by flowing pure compressed gas through an axisymmetric convergent-divergent nozzle into an almost-vacuum chamber. When a reaction happens, the central chamber is generally surrounded by a close-packed γ -detection array to detect γ -rays emitted by the reaction, while a collimated silicon detector fixed at a forward angle is used to monitor the incoming ion-beam current.

The beam and HIPPO are schematically shown in Fig. 1a. One can easily see the effective zone is the intersection of two cylinders. Gas is injected through a nozzle into the central chamber and the



(a) The intersection of the boundary of HIPPO and beam..

(b) The eneral layout of the HIPPO.

Figure 1: Schematic of the HIPPO gas-jet target, the left one is used for simulation, the right one is viewed perpendicular to the ion beam and gas-jet axes.

main fraction of the gas flow is captured by a catcher, as seen in Fig. 1b [3].

2 Numerical Simulation

2.1 Finite Element Analysis (FEA)

The basic formula we use to calculate elastic scattering is the Rutherford scattering formula. The differential cross section can be derived from the Binet equation, given by

$$\sigma_C(\theta_C) = \left(\frac{1}{4\pi\epsilon_0} \frac{Z_1 Z_2 e^2}{4E_C} \right)^2 \csc^4 \frac{\theta_C}{2}, \quad (1)$$

which is derived for the center of mass frame. We numerically solved the discretized version of the scattering and subdivide the HIPPO gas target into tiny parts. After solving the parts directly we can assemble every element into the complete HIPPO, that describes the entire problem.

The cross section is

$$\sigma_{total} = \iiint_{(V)} \frac{d\sigma_L}{d\Omega} d\Omega, \quad (2)$$

The probability be be calculated by

$$P = \int_{-\infty}^{\infty} \iiint_{(V)} f(E) \sigma_C(\phi') nt dE dV, \quad (3)$$

We take the discretized form to calculate numerically,

$$P = \sum_{i=1}^p \sum_{j=1}^q f(E_q) \sigma_{C_p}(\phi'_p) n_p \Delta t_p. \quad (4)$$

where $f(E_q)$ is the probability density function (PDF) of the beam, n is the number density of HIPPO, and t the thickness.

2.2 Space Analytic Geometry to Calculate Effective Solid Angle

There are two collimators before the detector to restrict the angle of Helium recoil, thus it is necessary to consider solid angles carefully. The effective area in the detector is the intersection of

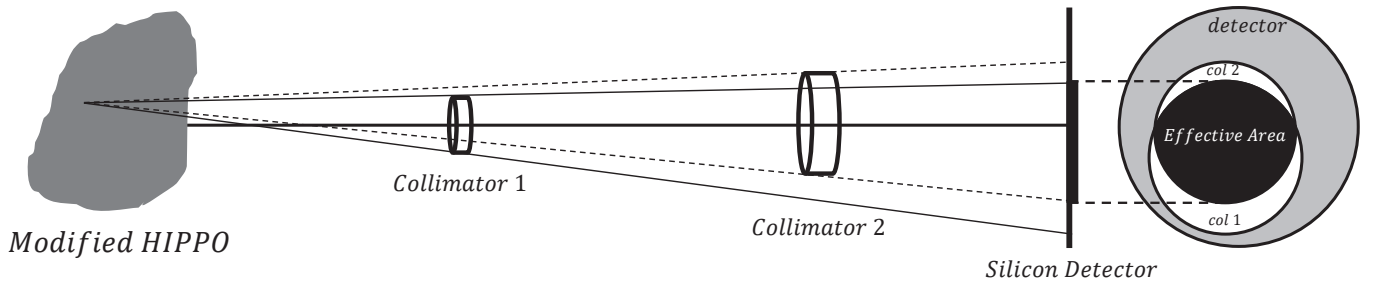


Figure 2: Take the center of the gas target as the vertex, take the sight as the bus, and make two cones, the intersection of the detector with which is defined as an effective area.

two ellipses, resembling your visible range of a plane when looking through two apertures, as shown

schematically in Fig. 2. Here we apply space analytic geometry to calculate. Note that the axis here needs to be transformed from the original one.

The silicon detector is so big that every particle being able to pass the two collimators are bound to hit on the detector.

2.3 Energy Loss and Straggling

Charged particles like our ion beam suffer energy loss when traveling material. The relativistic version of energy loss is described by Bethe formula, found by Hans Bethe in 1932,

$$-\left\langle \frac{dE}{dx} \right\rangle = \frac{4\pi}{m_e c^2} \cdot \frac{nz^2}{\beta^2} \cdot \left(\frac{e^2}{4\pi\epsilon_0} \right)^2 \cdot \left[\ln \left(\frac{2m_e c^2 \beta^2}{I \cdot (1 - \beta^2)} \right) - \beta^2 \right], \quad (5)$$

where c is the speed of light and ϵ_0 the vacuum permittivity, $\beta = \frac{v}{c}$, e and m_e the electron charge and rest mass respectively.

Besides, there are statistical fluctuations when particles colliding and transferring energy in each collision, known as energy straggling, described by the Gaussian form, assuming there are sufficient collisions.

$$f(x, \Delta) \propto \exp \left(\frac{-(\Delta - \bar{\Delta})^2}{2\sigma^2} \right), \quad (6)$$

The first approximation is derived by Bohr to be [4]

$$\sigma_0^2 = 4\pi N_A r_e^2 (m_e c^2)^2 \rho \frac{Z}{A} x. \quad (7)$$

We calculate the energy loss and energy straggling layer by layer when the ion beam traveling through the target, ensuring the accurate energy distribution of the beam at every element.

2.4 Kinematic Relationships and Probability

It is obvious that we can not apply directly the Rutherford differential scattering cross section formula. The recoil separator relies on gaseous helium target HIPPO, which uses inverse kinematics,

i.e. a heavier incident beam collide with an almost-standing lighter gas target. That is why we will discuss the kinematics of recoil and scattered here. Using the transformation of the reference frame from the center of mass (C.M.) to the lab, as shown schematically in Fig. 3, we derive the cross section for Helium, the recoil. The energy of the incident in the C.M. frame is

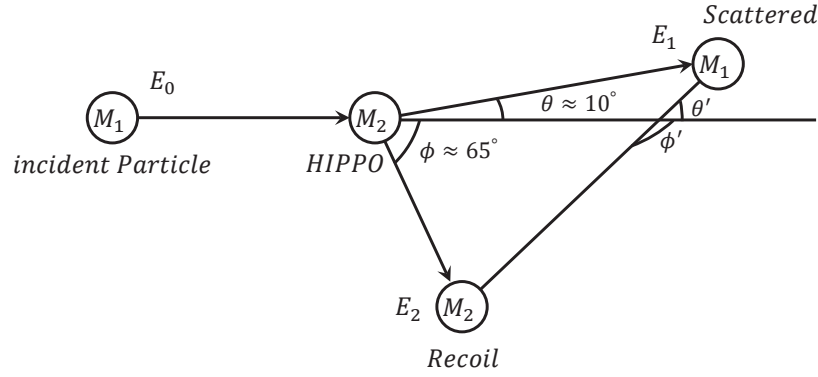


Figure 3: Trajectories of an incident particle and gas target particle before and after a scattering event as seen from the C.M. frame and laboratory frame. The primed quantities are in C.M. system.

$$E_C = \frac{m_2}{m_1 + m_2} E_L.$$

Another transition is the solid angle. The solid angle we calculated is for Helium in the lab frame and need to be turned into the version in the C.M. frame. The intensity ratio for recoil nucleus is

$$\frac{\sigma(\phi')}{\sigma(\phi)} = \frac{I(\phi')}{I(\phi)} = \frac{\sin \phi d\phi}{\sin \phi' d\phi} = \frac{1}{4 \cos \phi}. \quad (8)$$

Substitute (8) into what has been calculated about solid angle before, we can immediately know the total cross section, sum up all of which will give the probability.

3 Results and Discussion

3.1 The Result

The exact calculation result and the experimental data are carried out as mentioned before. We carried out a $2 - D$ matrix plane to describe the energy distribution when the beam going through

the target. One of the intermediate states is shown in Fig. 4.

The comparison between the calculation and the data are shown in Fig. 5a. However, there is an imprecise calibration of the silicon detector. Thus we manually shift the data to the position of the calculation to compare the shape.

The density of the outer section of the gas target is much lesser the inner section, which is the reason why there are two bumps at both sides of the curve. Moreover, the energy will lose when passing through the material, making the curve asymmetrical, the most direct phenomenon of which is that the peak is split, especially the left secondary peak is higher than the right one. Once we take

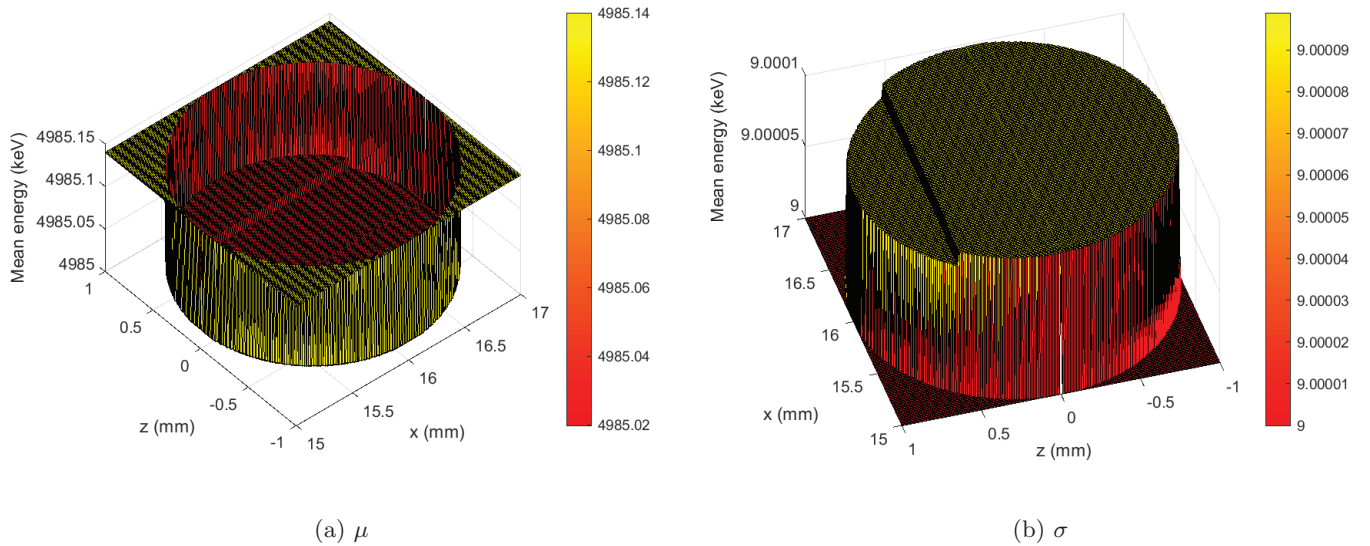


Figure 4: Energy distribution in a particular plane of the beam when passing through the gas target. We approximate it as a Gaussian distribution, with the parameters represented by the two surfaces keep changing.

the detector resolution into account, which is about 15keV the two curves become almost the same, as shown in Fig. 5b.

We consider the detector resolution by replacing every point as a small Gaussian distribution, by which the total calculation counts are redistributed, faring more dispersed than the exact one. Obviously, the fine structure of the recoil counts-energy is covered up due to the relatively low resolution.

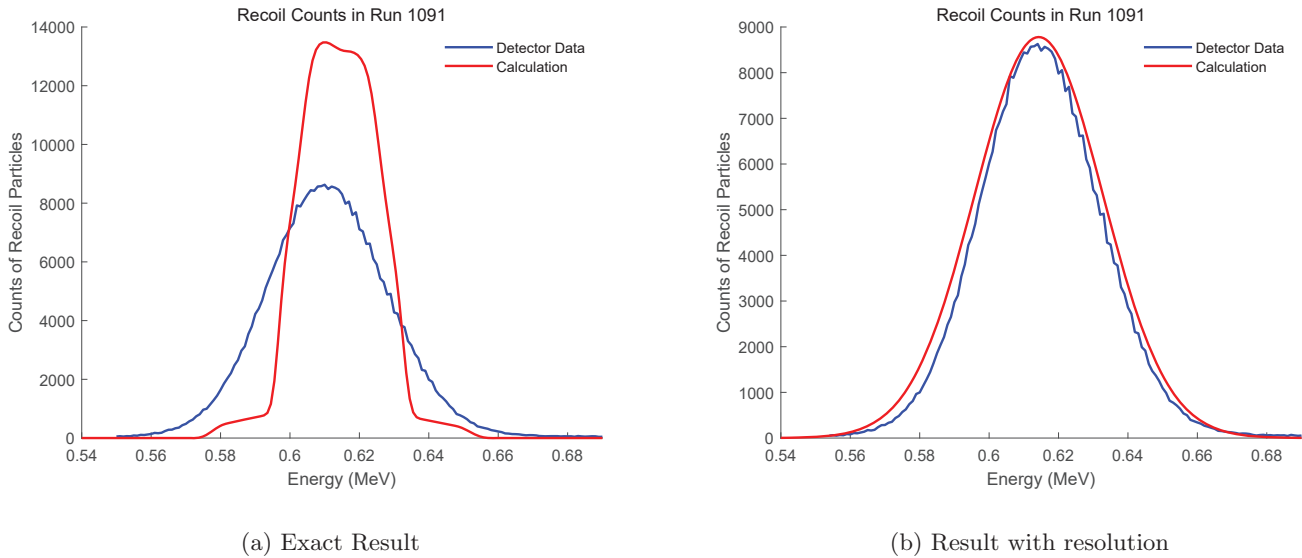


Figure 5: Exact calculation implemented by our algorithm. The red line is the calculation and the blue line is the experimental data in St.George Run 1091. Note that the detector resolution is not high enough so the data looks like a symmetrical curve.

3.2 Deducing the Beam Intensity

As we have mentioned before, the foremost function of our calculation is to deduce the beam intensity from the spectra of scattering energy distribution to offer a precise way to calculate the reaction cross-section. Beam intensity will be easily calculated based on the former discussion. We reverse the way of developing the simulation, reading in the elastic detector spectra and calculate how much beam is hitting the HIPPO. The result is $I = 463.51\text{nA}$, which is very close to the coarse data $I = 500\text{nA}$.

4 Conclusion

We use the FEM to calculate the distance and solid angle of a single element to the detector, using inverse kinematics and Rutherford scattering to derive the cross-section of the recoil. We subsequently consider the Gaussian distribution of the beam, including the energy loss and straggling layer by layer when traveling through the target. Numerical simulation demonstrates that there exist two bumps in the curve and the peak is split into two asymmetrical secondary peaks, but the fine structures are covered up due to the relatively deficient resolution. After considering the effect of the detector resolution, the calculation results agree very well with the data. Therefore, our approach provides an accurate and efficient method to compute the intensity of the incident beam and fine structure of the recoil counts-energy relationship.

5 Acknowledgements

I would like to express my sincere gratitude to my advisor Prof. Manoël Couder, who gave me invaluable guidance on this theoretical project with extraordinary patience, enthusiasm and accurate insights into physics throughout the summer. Besides, professor Couder's optimistic attitude toward research and unremitting encouragements to me give me the strength of persistence, otherwise, I would not know where to work on and which to calculate.

I would also like to sincerely thank graduate student Shane Moylan, Christopher Seymour, Luis Morales, and postdoctoral Alexander Dombos, all of whom listen carefully and give helpful advice in every group meeting. Shane, without whom I would never finish the project so quickly, spent vast time helping me understand the physics background and find issues about the calculation. Luis also gave me numerous ideas to implement, especially the knowledge of the silicon detector. Chris provided information about the detector. Alex gave tremendous help on making concepts clear,

finding critical information, and other necessary aspects. Alex's selfless guidance, encouragement, and patience greatly influenced my attitudes toward physics research. Special thanks to Lori Fuson and Prof. Umesh Garg at the University of Notre Dame for allowing me the opportunity this summer and patient notifications of REU activities.

Finally, I truly appreciate my Alma Mater Xi'an Jiaotong University for selecting me as one of the visiting students, giving the best gift to me in my sophomore summer, and offering tuition and financial support.

References

- [1] M. Couder, G.P.A. Berg, J. Grres, P.J. LeBlanc, L.O. Lamm, E. Stech, M. Wiescher, and J. Hinnefeld. Design of the recoil mass separator st. george. *Nuclear Instruments and Methods in Physics Research Section A: Accelerators, Spectrometers, Detectors and Associated Equipment*, 587(1):35 – 45, 2008.
- [2] Antonios Kontos, Daniel Schrmann, Charles Akers, Manoel Couder, Joachim Grres, Daniel Robertson, Ed Stech, Rashi Talwar, and Michael Wiescher. HIPPO: A supersonic helium jet gas target for nuclear astrophysics. *Nuclear Instruments and Methods in Physics Research Section A: Accelerators, Spectrometers, Detectors and Associated Equipment*, 664(1):272 – 281, 2012.
- [3] Zach Meisel, Ke Shi, Aleksandar Jemcov, and Manoel Couder. Exploratory investigation of the hippo gas-jet target fluid dynamic properties. *Nuclear Instruments and Methods in Physics Research Section A: Accelerators, Spectrometers, Detectors and Associated Equipment*, 828:8 – 14, 2016.
- [4] William R Leo. *Techniques for nuclear and particle physics experiments: a how-to approach*. Springer Science & Business Media, 2012.



Influence of Carbon Abundance on Stellar Photometric Temperature Estimates

Yihao Zhou

2019 NSF/REU Program

Physics Department, University of Notre Dame

Advisor: Prof. Timothy Beers

Abstract

Accurate estimates of effective temperature are of significant importance for the further study of a star. For the carbon enhanced metal-poor stars, the strong absorption lines can severely affect the color, hence affecting the estimated temperature. This work shows the influence of the carbon abundance on the temperature estimates by getting the fitting formula for carbon-rich and carbon-poor stars in SEGUE and comparing their difference. During the fitting process, we use iteration within a uniform sample. The residual of the fitting is given as a test. The effective range of the calibration is also given based on the investigation of the error distribution. It's shown from the results that at different temperature range and for different colors, the degree of influence of carbon abundance is quite different. For cooler stars and for filters at the blue end, the carbon's influence is more pronounced.

1 Introduction

There has been a long history for the human to point the telescope into the deepest part of the sky, trying to find the objects far away from us to get an insight into the origin and evolution of the universe. This is called the traditional cosmology. While in recent decades, the idea of 'near-field cosmology' has been formed and developed. That is, using the stars in our Galaxy, the Milky Way, to study the early universe and the origin of stars and galaxy formation (Freeman and J.Bland-Hawthorn, 2002).

The chemical abundance of a star has been assumed as one of the best proxies for its age. In general, the atmospheric metallicity (usually refers to the elements heavier than lithium) reflects the degree of chemical enrichment of the gas clouds from which the star formed. The underlying assumption is that metal-poor stars are likely to be old (Frebel and Norris, 2015). Over the past few decades, extensive efforts have been

devoted to the search and study the metal-poor stars. Now it's been confirmed that those stars provide means for investigating numerous issues regarding the nature and evolution of the early universe (Beers and N.Christlieb, 2005). For example, the nature of the Big Bang and the first stars, prediction of element production of supernovae, the first mass function (FMF), the nature of the metallicity distribution function (MDF), the astrophysical sites of neutron-capture element production.

One of the most important and interesting results so far is that a large part of the metal-poor stars exhibits overabundance of carbon, i.e. $[C/Fe] > +1$. Beers and N.Christlieb (2005) classified C-rich objects having $[C/Fe] > +1.0$ as Carbon Enhanced Metal-Poor (CEMP) stars. Those metal-poor stars have received extensive study over the past few decades. To learn more about the subclasses and process of CEMP, we refer the readers to Beers and N.Christlieb (2005), Yoon et al. (2016).

The carbon enhancement can be seen clearly from the presence of an abnormally strong CH G-band feature at 4300\AA . Strong absorption lines can severely affect the emergent flux distribution. In many cases, they reduce the flux in some bands and hence change the color. For color consists of two filters, if the carbon abundance influences the two filters at a similar level, the color won't show much difference between CEMP and normal metal-poor stars. While in many cases, the carbon abundance affects some specific filters far more than others, so the colors would increase or decrease to some degree. The effective temperature is usually gotten from the comparison between colors and temperature scales. Hence, the carbon abundance will influence the temperature estimates (Aoki et al., 2002). Getting an accurate temperature is a fundamental demand for further study, so to investigate the difference between the temperature of CEMP and that of normal metal-poor stars is an important task.

This work aims to show such influence and develop an empirical color-temperature calibration. The paper is organized as follows. In Section 2, we show where we get the data and how we perform the data-cleaning. Then we analyze roughly the parameter distribution of the data. In Section 3, we attempt to find the most sensitive color by calculating the variance of color. The process of fitting is provided in Section 4. In Section 5, the difference of carbon-rich and carbon-poor stars are shown and error distribution is also discussed. Then we analyze the influence of carbon for different tem-

perature range and different colors. We finally conclude in Section 6.

2 Dataset

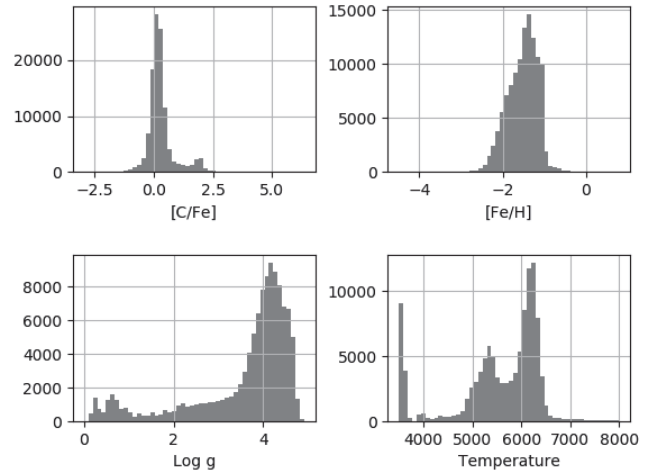


Figure 1: Parameter distribution of the used data

In this work, we use the SEGUE data to build the empirical calibration. There are 300398 records in the SEGUE but there are some abnormal values and missing data which needed removing before the analysis. At first, we pick the ‘star’ from those data for there are some records for galaxy and QSO and then there are 249584 records left. We also remove the stars whose magnitude are missing and whose other parameters, such as [C/Fe] and [Fe/H], are abnormal. (If the SDSS system cannot get that value of the parameter, it will return a special number such as -9999 in some case, which is obviously abnormal.) We also consider uncertainty distribution. Because the estimated temperature and the carbon abundance are of significant importance for the research, we put strict limitations on the effective temperature uncertainty and the [C/Fe]

and $[\text{Fe}/\text{H}]$ (since what we need is absolute carbon abundance instead of the ratio of $[\text{C}/\text{Fe}]$, the value of $[\text{Fe}/\text{H}]$ is also something that needs to be considered). We limit the effective temperature uncertainty within 50K, the $[\text{C}/\text{Fe}]$ uncertainty within 0.2, the $[\text{Fe}/\text{H}]$ uncertainty within 0.1. At last, we have 114379 stars left.

Then we study the distribution of several parameters such as temperature, $[\text{Fe}/\text{H}]$, $[\text{C}/\text{Fe}]$ and $\log g$ in Fig.1. Among them, the distribution of the low-temperature end needs to be paid special attention. There are abnormally too many stars whose temperature around 3500K and there is an unexplained gap at about 3800K. That's because SDSS may put all the stars whose temperature under a special temperature into the 3500K. To exclude those part of stars, we don't study the stars whose temperature under 4000K.

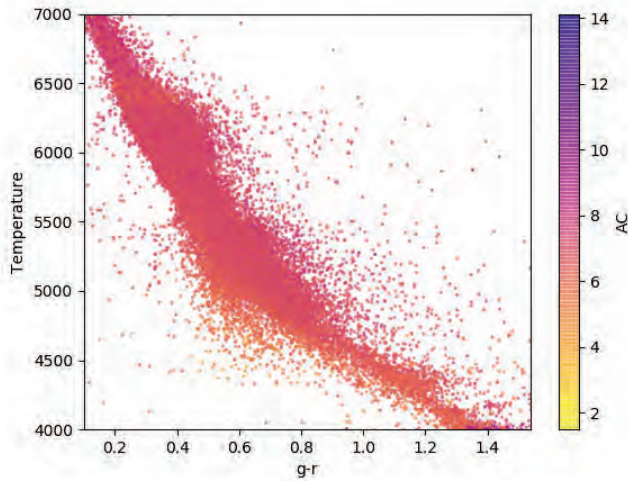


Figure 2: The relation between the temperature and color ($g-r$). The colorbar shows the absolute carbon abundance.

We show the relation between the temperature and color in Fig.2, we use $g-r$ as an example. There are many stars concentrate in the temperature range 312

around 6200K and the data are dispersed to some degree. Those are stars in the main-sequence turnoff. There are many complicated physical and chemical reactions during this process, depending on the mass of the stars, so it's understandable that the dispersion is present.

3 Find the most sensitive color

In the SDSS system, there are five filters ($ugriz$) so we can get 10 color indices from them. To find the most sensitive color to temperature and carbon is an important task because the most sensitive color tends to correspond to the most reliable fit formula.

To find the most sensitive color to temperature, we divide the stars into different temperature bins and each bin is 50K wide. For the stars in each bin, we calculate the average color for them. The variance of these average colors can show the difference between the colors of stars with different temperature, namely, the color's sensitivity of the temperature. And to find the most sensitive color to carbon abundance, we do the same thing for the stars in each carbon abundance bin. We divide the stars according to $[\text{C}/\text{Fe}]$ and each bin is 0.1 (0.7 ~ 2.7).

We list the result in the Table.1. The colors are sorted in descending order. From the result, we can see that for temperature and carbon abundance, the order of colors sorted by the variance are almost the same, $u-z$ is the most sensitive color, followed by $u-r$. And the $r-z$ and $i-z$ are the least sensitive ones, meaning

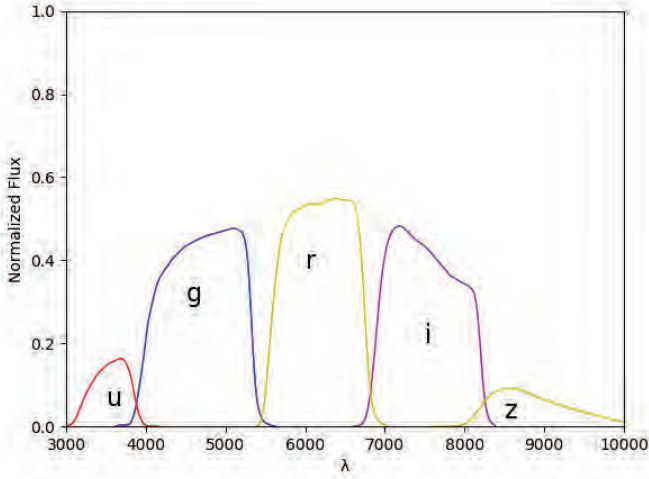


Figure 3: Filter transmissions of the SDSS photometry

that stars with different temperature or carbon abundance don't differ a lot in $r-z$ or $i-z$, but have distinguishing $u-z$ or $u-r$. That's understandable for the filter u and the z are far from each other (which we can see from the Fig.3), so these two filters will cover more information about the spectrum than other colors.

Table 1: Variance of color

Color	Var(T)	Color	Var(C)
$u-z$	1.30	$u-z$	1.04
$u-r$	1.06	$u-r$	0.79
$u-i$	0.74	$u-i$	0.44
$g-i$	0.44	$g-i$	0.40
$g-z$	0.30	$g-z$	0.25
$u-g$	0.26	$u-g$	0.15
$g-r$	0.14	$r-i$	0.14
$r-i$	0.08	$g-r$	0.07
$i-z$	0.03	$i-z$	0.06
$r-z$	0.01	$r-z$	0.02

What has to be mentioned is that the order of colors will change when different ranges are investigated, so the most sensitive color is different for different temperature ranges. We calculate the variance for temper-

ature range of (4000,6000), (6000,8000), in which the order of colors changes a lot. Result are listed in the Table.2.

We can see from these results that for the high temperature end, the color $u-g$, $u-r$, $u-i$, $u-z$ are not so effective compared with their behavior at lower temperature range. Although high temperature stars are not the main target of this study, if we need to calibration them, choose $g-z$ or $g-i$ instead of $u-z$ or $u-i$ might be a good choice. Because of such difference between the behavior of $u-z$, $u-i$, $u-r$ at high and low temperature ends, when we develop the calibration for these colors, we exclude the high temperature end and limit the data below 6000K, otherwise it's challenging to get a good fit.

Table 2: Variance for different temperature range

Color	Var(4000,6000)	Color	Var(6000,8000)
$u-z$	1.11	$g-z$	0.045
$u-i$	0.93	$g-i$	0.032
$u-r$	0.70	$u-z$	0.020
$u-g$	0.30	$g-r$	0.013
$g-z$	0.26	$u-i$	0.011
$g-i$	0.18	$r-z$	0.010
$g-r$	0.09	$u-g$	0.006
$r-z$	0.05	$r-i$	0.004
$r-i$	0.02	$u-r$	0.002
$i-z$	0.01	$i-z$	0.002

4 Fitting Process

What we plan is to get the fit formula relating temperature and color. And then we divide stars data according to the absolute carbon abundance and get the fit formula for each group. By comparing the differ-

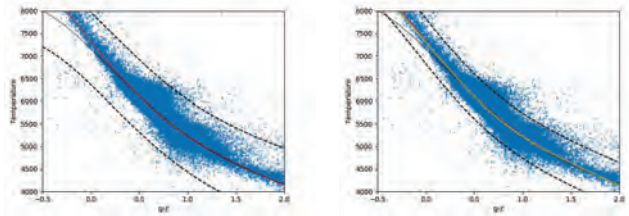
ence of these fit lines, we can have an insight into the influence of the carbon abundance on the photometric temperature estimates. What’s more, these fit formula can also serve as empirical calibration which might be helpful when we try to determine the temperature for a star.

4.1 Problems

There are some problems need to be considered before we start to develop the empirical calibration. First, although we have done data-cleaning, there are still many data left and unavoidably, all these data cannot fit perfectly with a polynomial formula. There are many outliers that must be excluded. How to identify these outliers is an important question. And another problem is that the temperature distribution of these stars is quite uneven. As mentioned above, there are too many stars in the main-sequence turnoff, which locate around 6200K. Considering such a difference in quantity, the data at the end cannot influence the final result as much as the data in the medium temperature range. And in that case, the fit formula cannot work well for the stars at two ends. In the following section, we will show how we addressed these two problems.

4.2 Exclude the Outliers

To exclude the outliers, we iterate the fitting process. We use the color $g-z$ to explain that. At first, we use all the data (after data-cleaning) to get the first fit formula, which is the black solid line in Fig.4(a). Then we select



(a) The first two fit lines and (b) The final fit line and the smaller range.

Figure 4: Iteration of the fitting.

a region, which is the space between the two dashed lines gotten by moving the first fit line. Data outside these two lines are excluded and we only use the data within this range to get another fit line (the red line in Fig.4(a)). We can see that the second line is better than the first line. And then we iterate again but this time we use data with a smaller range to get the third line (yellow line in Fig.4(b)), which is also the final fit result.

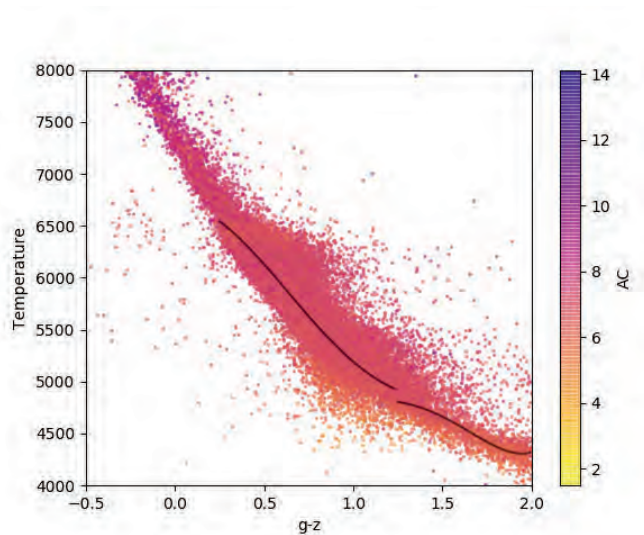


Figure 5: The empirical colour–temperature calibrations of the grouped sample. The colorbar shows the absolute carbon abundance.

4.3 Uneven Distribution

For the second problem, we have two solutions. One is to divide the stars into different groups and fit each group respectively. In this way, those temperature range which has less stars will have a fit line specially for them. We design to divide the stars into three temperature groups: $>6500\text{K}$, $4500\sim 6900$, $4000\sim 4900$. There is overlap between the groups or the stars around boundary cannot fit well. The fit result is shown in Fig.5

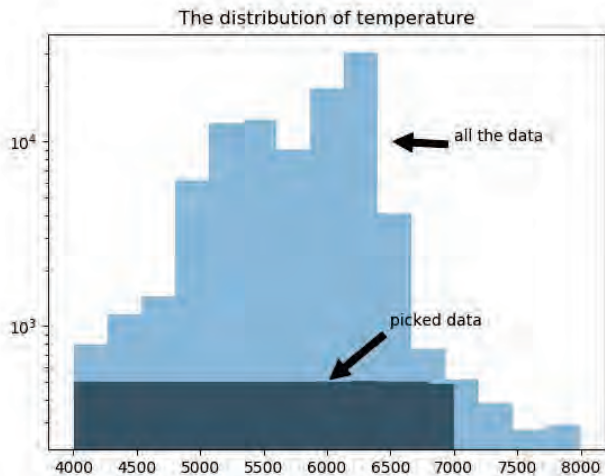


Figure 6: The uniform sample: pick the same number of stars from every temperature bin.

The other way to solve this problem is to make a uniform sample. What we want is to make sure every temperature range will influence the final fit result at a same level, namely, we want the numbers of stars in each group are similar. We divide the stars into different temperature bins and then pick the same number of stars from each bin, which is shown in Fig.6. And in Fig.8, it's can be seen that for every temperature range, the wide of the space which most data concentrate in

is quite similar.

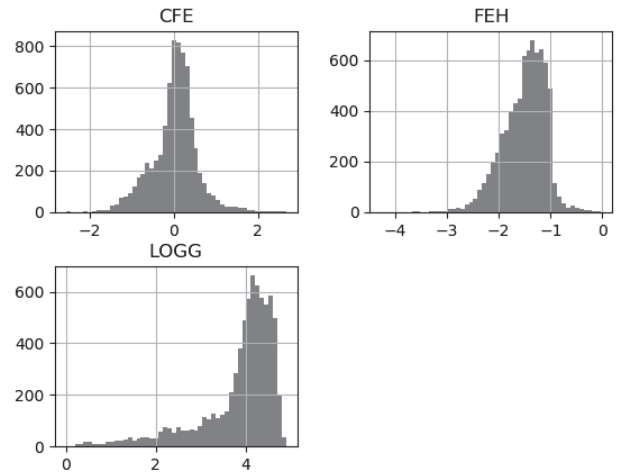


Figure 7: The uniform sample's distribution of parameters

Ideally in this way each group will have exactly the same amount of data. While actually, there is still some difference between the numbers of stars in every group. Some groups have so few stars that it cannot provide enough data as others do, so some samples may be a little less than others but it's not big enough to influence the final results. What's more, for some temperature ranges, the stars are dispersed, such the main-sequence turnoff around 6200K , so many stars in this range will be excluded in the iteration of fitting process. Hence, stars which actually play a role in the fit are still different from one range to another. We show the parameter distribution of the uniform sample in Fig.1. From the comparison of Fig.7 we can say that this uniform sample serve as a good representation of the whole data for its distribution of parameters are quite similar with that of whole sample, except for the temperature of course. The fit result is shown in Fig.8.

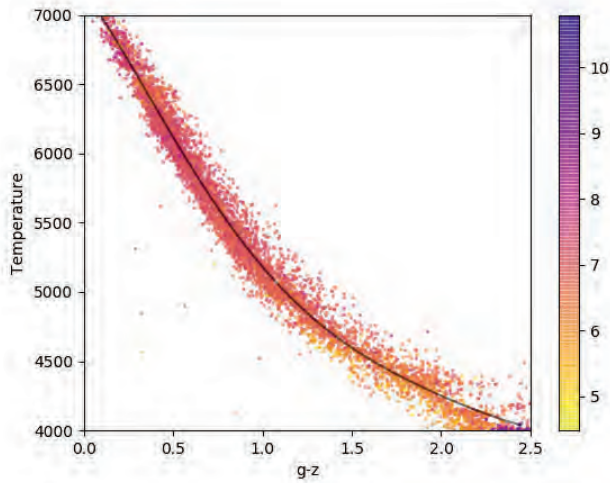


Figure 8: The empirical colour–temperature calibrations of the uniform sample. The colorbar shows the absolute carbon abundance.

We choose to use the uniform sample for the remainder of this work. It would bring some troubles if we use the first solution because we have to decide which group the star is in. It makes no difference if we’re studying the stars with known temperature, but is quite complicated when we try to determine the temperature of a star using this calibration.

5 The influence of carbon abundance

5.1 The calibration

To show the influence of the carbon abundance, we divide the stars according to their absolute carbon abundance and then get fit line for each group. By studying the difference of these fitting lines, we can learn how the carbon abundance influence the estimated temperature. The medium of AC (absolute carbon abundance) of the used data is about 7.1. We divide the star into two groups: AC above 7 and below

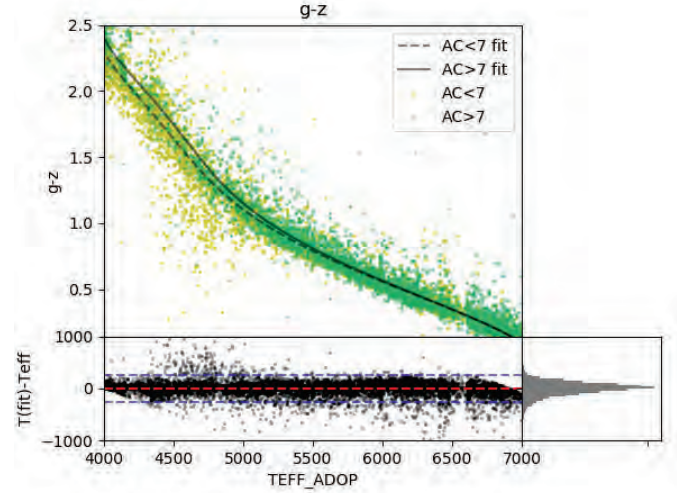


Figure 9: The influence of the carbon abundance on temperature estimates, choosing the color $g-z$ as an example. The lower part is the residual of the fit as a function of temperature. The blue lines are $\pm 250\text{K}$, and the red line is the zero line. The lower left part is the histogram of the error: $T(\text{fit})-T(\text{ADOP})$

7. The result for $g-z$ is shown in the Fig.9

5.2 The influence on different temperature ranges

Regardless of the color, the carbon-rich stars are always hotter than the carbon-poor stars with the same color value. It’s because the carbon absorption line reduce the emergent flux. At high temperature end, the influence of carbon is not so clear. While with temperature decreasing, the difference between two groups shows up. That’s because for hotter stars, the molecular absorption is weak so the color won’t be effected too much.

Table 3: The temperatures below which the difference is larger than 50K

Color	$u-r$	$u-i$	$u-z$	$g-r$
T/K	6000	6000	6000	5935
Color	$g-z$	$g-i$	$r-i$	$r-z$
T/K	5098	5446	4438	4698

Based on the above analysis, we can find the temperature range in which the carbon abundance should take into account. For the influence is bigger for the cooler stars, what we given is a specific temperature below which the carbon needs to be considered. The effect of carbon is quantified by the difference between the fit temperatures of the carbon-rich and carbon-poor stars with the same color value. We set the standard as 50K. The temperatures below which the difference is larger than 50K are list in the Table.3.

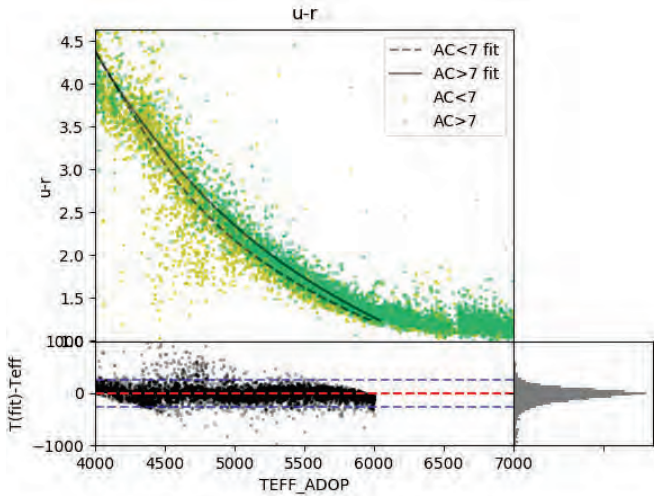


Figure 10: The influence of the carbon abundance for color $u-z$. The influence of carbon is obvious for all the temperature range

5.3 The influence on different colors

The influence of carbon are very obvious for colors includes filter u or g . That is because most carbon absorption lines are located in the blue end of the spectrum and the filter u and g are in this part, as seen in Fig.3. For them, the influence of carbon is obvious for all the temperature range, which is shown in the Fig.10. In Fig.10, the convergence of these two lines

means the fit is not quite accurate for this part, which is confirmed by the residual. We will discuss this inaccuracy in the later part of this work. For the colors not so sensitive, such as those includes filters at the red end, the two fit lines are almost the same, especially for the hot stars.

The data in color $i-z$ are more dispersed than those in other color, so it can be predicted that the fit is not so good for this color and the standard deviation would be quite big, which is also indicated by the Table.4. And the standard deviation is also big for color $r-i$ and $r-z$. Hence, this three colors should avoid being used.

Table 4: The error analysis of the fit

Color	$u-i$	$u-r$	$u-z$	$g-r$	$g-z$
Mean	5.15	5.03	5.00	1.31	-2.80
σ	165	170	163	185	190
Color	$g-i$	$i-z$	$r-i$	$r-z$	
Mean	-0.78	-11.27	-1.10	-7.32	
σ	178	318	236	230	

5.4 The effective range of the calibration

We list the analysis of the fit error in Table.4. We can see from it that the residual average is around zero. The standard deviations are all within 250K except for the $i-z$. It's quite satisfying considering the large amount and the wide dispersion of the used data. The fit result is good for most temperature range, while at two ends, the fitting error diverges from the zero line. To make sure the accuracy of the calibration, we decide to cut the range. And the effective ranges in which the fit is good enough are listed in Table.5. We

determine the effective ranges by limiting the error average and the rate of star whose error is within $\pm 250\text{K}$. For stars with unknown temperature but with available SDSS colors in this range, we can try to determine the temperature according to this calibration.

Table 5: The effective range of the color.

Color	$u-i$	$u-r$	$u-z$
Eff Range	[1.77,4.45]	[1.60,3.85]	[1.90,4.85]
Color	$g-r$	$g-z$	$g-i$
Eff Range	[0.14,1.37]	[0.14,2.22]	[0.14,1.89]
Color	$i-z$	$r-i$	$r-z$
Eff Range	[0.24,0.26]	[0.03,0.56]	[-0.03,0.88]

6 Conclusion

The main goal of this work was to investigate the influence of the carbon abundance on the photometric temperature estimates. We first calculate the variance of the colors of stars in different temperature or carbon bins, showing the sensitivity of color to temperature and carbon. Then we try to develop the calibration. During the fit process, we come across two problems caused by the large number and wide dispersion of the used data. We use iteration to exclude the outliers and make a uniform sample to make sure every temperature range affect the final results at a similar level. We fit the stars whose AC above and below 7 respectively. By analyzing the divergence of the two fit lines, we gain an insight into the influence of carbon abundance. The fit doesn't work well at the two ends of the temperature range, so we cut the range and give the effective range of calibration for each color. For different colors

and temperature ranges, the degree of influence varies a lot. Our analysis for the fit results reveals that for cool stars and for filters at the blue end, the influence is biggest, which is understandable. Ultimately, we hope to significantly improve the calibration of photometric temperature estimates for carbon-enhanced metal-poor stars.

Acknowledgement

I'm grateful to the University of Notre Dame and the REU program for providing me such great experience. Special thanks go to my advisor Prof. Beers, Prof. Placco and Devin Whitten who gave me patient guidance and many valuable suggestions. I feel really lucky to work with these helpful people.

References

- Wako Aoki, John E. Norris, Sean Gyan, and et al. *Astro.J.*, 567:1166–1182, 2002.
- TC Beers and N. Christlieb. *Annu. Rev. Astron. Astrophys.*, 43:531–580, 2005.
- Anna Frebel and John E. Norris. *Annu. Astron. Astrophys.*, 53, 2015.
- K. Freeman and J. Bland-Hawthorn. *Annu. Rev. Astron. and Astrophysics*, 40(1):487–537, 2002.
- Jinmy Yoon, TC. Beers, and Vinicius M. Placco. *Astro.J.*, 833(1), 2016.